

WEIGHTED NETWORKS AND THE TOPOLOGY OF BRAIN NETWORKS

By

LUIS M. COLON-PEREZ

A DISSERTATION PRESENTED TO THE GRADUATE SCHOOL
OF THE UNIVERSITY OF FLORIDA IN PARTIAL FULFILLMENT
OF THE REQUIREMENTS FOR THE DEGREE OF
DOCTOR OF PHILOSOPHY

UNIVERSITY OF FLORIDA

2013

© 2013 Luis M. Colon-Perez

To my wife and family

ACKNOWLEDGMENTS

I would like to thank Prof. Thomas H. Mareci for his support and guidance throughout these past four years. His knowledge, input, and keen attention to detail have been influential factors to my growth as a student and a researcher. I am grateful for Prof. Mareci's guidance in my MRI experiments and the numerous opportunities that presented themselves while working in his lab, such as being able to make research presentations in Canada and Australia. His mentorship has allowed me to grow not only as a researcher, but also as a person. I would like to express my deepest gratitude to Prof. Beverly Brechner. Her eagerness towards the research topic in this dissertation and our insightful discussions were instrumental to my study of graph theory and network theory. Her discussions had a great impact on the development of this work. Last, but not least, I would like to thank Dr. Paul R. Carney, for the discussions, and the research opportunities to work in his laboratory. I recognize that, even though these research endeavors are not part of this dissertation, they did help me grow as a scientist by showing me the broad spectrum of techniques and perspectives that can be used to solve modern problems in the science of the brain.

I feel very fortunate to have been able to work in the Advanced Magnetic Resonance Imaging and Spectroscopy (AMRIS) facility at the McKnight Brain Institute at the University of Florida. The opportunity to work with world-class equipment and staff at AMRIS is something to be really grateful for. I am especially thankful to Kelly Jenkins, Barbara Beck, Dan Plant, and Huadong Zeng for multiple discussions and help with setting experiments and solving hardware problems. Also, my deepest gratitude to my lab mates: Mansi B. Parekh, Garret Astarly, William Triplett, Christine Girard, Aditya Kumar and Guita Banan. I will always remember the fun times in lab and hard work that

we all performed as a team. Also, I would like to show my deepest gratitude to the undergraduates that helped me with the least fun part of this dissertation (node segmentation): Caitlin Spindler, Shelby Goicochea, and Michelle Couret. I appreciate their loyalty to stay with me and I hope you did learn something with me in lab. I would also like to mention other undergraduate students that at some point have helped me with my different investigations: R. Horesh, R. Klassen, E. Carmona and A. Boutzoukas. Lastly, I would like to thank the Physics Department and the professors and staff for all of their help in the past five years. Most importantly, my Physics dissertation committee members: Prof. Mark Meisel, Prof. James Fry and Prof. Neil Sullivan.

Special contributions to this dissertation will be listed in this paragraph. Dr. M. Parekh trained me in the diffusion weighted acquisitions and helped acquire data. Dr. G. Astarly was my MR tutor in lab and helped set up experiments. Mr. Triplett helped me with the coding of the tractography software and made the first version of the software used to perform the tractography work. Dr. E Montie, provided brain rats to study their structural connectivity. Dr. C. Price provided the human data sets presented in this dissertation. Miss S. Goicochea, Miss. C. Spindler and Miss. M. Couret, segmented the rats nodes and assisted in the processing of the data.

I would like to extend a posthumous acknowledgement to my physics high school teacher and mentor Miguel Baez. "Mister Baez" as everyone knew him, passed away in March 2013 and, more than a teacher, he was an inspiration to many of his students, including me. I will always remember the good chats and candid memories of my high school years with him; may he rest in peace.

Finally, I would like to acknowledge the most important people in my life—my family. My wife, Yarelis, who has supported me all these years and stuck with me even with the long distance and sparse opportunities to see each other as often as we wanted to. She was the source of inspiration to continue my studies and finish this PhD. Also, I want thank my parents who raised me to become the person that is completing this PhD work. I would like to thanks Carlos Poventud for being a great college and even greater friend throughout my time in Puerto Rico and after I started my time here in Florida. Their love, guidance, support, and encouragement helped me overcome all adversities in these past years. Last, but not least, I want to thank my sister, Dialitza, for all of her love and support in my life. She was a source of inspiration and encouragement, as she recently graduated with her PhD in the past year, the first in our family.

TABLE OF CONTENTS

	<u>page</u>
ACKNOWLEDGMENTS.....	4
LIST OF TABLES.....	10
LIST OF FIGURES.....	11
LIST OF ABBREVIATIONS.....	14
ABSTRACT.....	16
CHAPTER	
1 INTRODUCTION.....	18
1.1. The Problem.....	19
1.2. Outline.....	20
2 BACKGROUND.....	22
2.1. Diffusion and MRI.....	22
2.1.1. Principles of Diffusion Displacement.....	22
2.1.2. Diffusion Weighted Imaging.....	24
2.2. Networks.....	33
2.2.1. Graph Theory Metrics.....	34
2.2.2. Random Networks.....	38
2.2.3. Small World.....	41
2.2.4. Scale Free.....	42
2.2.5. Brain Networks.....	43
3 GENERAL METHODS.....	54
3.1. MRI Acquisition.....	54
3.1.1. Human Data.....	54
3.1.2. Animal Data.....	55
3.2. Post Processing.....	55
3.3. Tractography.....	56
3.4. Network Calculations.....	57
4 WEIGHTING BRAIN NETWORKS.....	59
4.1. Opening Remarks.....	59
4.2. Methods.....	60
4.2.1. Edge Weight.....	60
4.2.2. Edge Weight Derived from DWI.....	65

4.2.3. Simulations.....	67
4.2.4. Node Segmentation.....	68
4.3. Results.....	70
4.3.1. Simulations.....	71
4.3.2. Cingulum and Corpus Callosum Networks.....	76
4.3.3. Limbic System Network.....	79
4.4. Discussion.....	82
4.5. Concluding Remarks.....	85
5 TOPOLOGY OF WEIGHTED BRAIN NETWORKS.....	96
5.1. Opening Remarks.....	96
5.2. Methods.....	97
5.2.1. Network Construction.....	97
5.2.2. Null Hypothesis Graphs.....	100
5.3. Network Metrics.....	101
5.3.1. Node Connectivity.....	102
5.3.2. Average Weighted Path Length.....	102
5.3.3. Clustering Coefficient.....	104
5.3.4. Small Worldness.....	105
5.4. Results.....	107
5.5. Discussion.....	116
5.6. Concluding Remarks.....	122
6 PATHOLOGICAL NETWORKS.....	141
6.1. Opening Remarks.....	141
6.2. Methods.....	142
6.2.1. Animals Treatment.....	142
6.2.2. Networks.....	142
6.3. Results.....	143
6.4. Discussion.....	148
6.5. Concluding Remarks.....	153
7 FUNCTIONAL NETWORKS.....	163
7.1. Opening Remarks.....	163
7.2. Theory.....	164
7.3. Global Functional and Structural Networks.....	166
7.4. Structural constraints to large DCMs.....	167
8 CONCLUSION AND FUTURE DIRECTIONS.....	170
8.1. Conclusions.....	170
8.2. Future Directions.....	172

APPENDIX

A	OPTOGENETICS AND FMRI	178
B	CONTINUOUS EDGE WEIGHT REPRESENTATION.....	180
C	COMPUTER CODES.....	187
D	AUTHOR'S PUBLICATIONS	190
E	GLOSSARY INDEX	191
	LIST OF REFERENCES	192
	BIOGRAPHICAL SKETCH.....	202

LIST OF TABLES

<u>Table</u>		<u>page</u>
4-1	Edge weight values across the acquired ten data sets of 1 mm ³	95
4-2	Edge weight values across the acquired ten data sets of 8 mm ³	95
5-1	Average node degree values.....	139
5-2	Average node strength values.....	139
5-3	Binary path length and clustering coefficient metrics.....	139
5-4	Weighted path length and clustering coefficient.	139
5-5	Small worldness of weighted and binary networks.	139
5-6	Human brain network nodes.....	140
6-1	Average degree (\hat{k}) values.....	161
6-2	Average node strength (\hat{s}) values.....	161
6-3	Binary network metrics.	161
6-4	Weighted network metrics.	161
6-5	Small worldness	161
6-6	Rat brain network nodes.....	162

LIST OF FIGURES

<u>Figure</u>	<u>page</u>
2-1 Stejskal Tanner diffusion sequence.....	50
2-2 The effect of the b value on the estimation of the diffusion profile.....	50
2-3 The Königsberg map	51
2-4 Types of Graphs.....	51
2-5 The small world phenomenon.....	52
2-6 Scale free distributions in scale.	52
2-7 Brain graph construction.....	53
3-1 Images of data used	58
3-2 Diagram of the tractography process.....	58
4-1 WM fiber connecting two nodes.....	87
4-2 A central node connected to four other nodes.....	87
4-3 A sketch displaying the process used to obtain the set of seed points.....	88
4-4 3D sketch of a system of 2 nodes connected by a fiber	88
4-5 Slant fiber path connecting two nodes at different planes.	89
4-6 Segmentation of a 3-node and 2-edge system.....	89
4-7 Human and rat brain networks.....	90
4-8 System of 2 nodes connected by a fiber at 45 degrees from the pixels.....	91
4-9 Edge weight plots of arc and slants	91
4-10 Edge weight values for a slant in plane of single voxel nodes.....	92
4-11 Coefficient of variation (c_v) plots as a function of σ levels.....	92
4-12 Edge weight plots for the cingulum and corpus callosum tracts	93
4-13 Excised rat brain edge weight values in the TL network.....	93
4-14 Excised rat brain node strength values in the TL network	93

4-15	Excised rat brain surface area values for the TL structures.....	94
4-16	Excised rat brain edge length values in the TL network.	94
5-1	Three-node network connected by two edges.....	124
5-2	Eleven-node weighted network.....	124
5-3	Graph density plot	125
5-4	Node degree measurements	126
5-5	Node degree distribution	127
5-6	Node strength values.....	128
5-7	Node strength distribution.....	129
5-8	Representative binary and weighted adjacency matrices.....	130
5-9	Average binary path length distribution scale	131
5-10	Average weighted path length distribution.....	132
5-11	Binary clustering coefficient distribution.....	133
5-12	Weighted clustering coefficient distribution.....	134
5-13	Weighted clustering coefficient distribution.....	135
5-14	Anatomical location of human nodes.....	136
5-15	Streamlines connecting nodes.....	137
5-16	Differences in binary and weighted matrices.	138
6-1	Degree values, results of rat networks	155
6-2	Degree distribution of rat brain networks	156
6-3	Node strength results of sparse networks.	157
6-4	Clustering coefficients distribution of sparse networks.	158
6-5	Anatomical location of rat nodes.....	159
6-6	Streamlines connecting nodes in the rat brain.....	160
8-1	Resolution effects on town borders in Puerto Rico.....	176

8-2	Validation of streamlines obtained with tractography with histology	177
A-1	Optogenetic stimulation and activation captured with fMRI.	179
B-1	3D fiber sideways.	185
B-2	Sketch of one of the portions that make up the fiber.	185
B-3	Sketch of the piece of the voxel that contributes to the edge.	185
B-4	Sketch of the isolated piece of the voxel contributing to the edge	186

LIST OF ABBREVIATIONS

AD	Average diffusivity
AM	Amygdala
BOLD	Blood oxygenated level dependent
CC	Corpus callosum
DCM	Dynamical Causal Model
DMN	Default mode network
DTI	Diffusion tensor imaging
DWI	Diffusion weighted imaging
EC	Entorhinal cortex
EPI	Echo planar imaging
ER	Erdős and Rényi
FA	Fractional anisotropy
FACT	Fiber assignment by continuous tracking
fMRI	Functional magnetic resonance imaging
FOV	field of view
GM	Gray matter
HARDI	High angular resolution diffusion imaging
HC	Hippocampus
L	Left side
MOW	Mixture of Wisharts
MR	Magnetic resonance
MRI	Magnetic resonance imaging
NMR	Nuclear magnetic resonance
PDF	Probability displacement function

PR	Puerto Rico
PTU	Propylthiouracil
R	Right side
SF	Scale free
SNR	Signal to noise ratio
SW	Small world
TD	Thyroid disruption
TE	Echo time
TH	Thalamus
TL	Temporal lobe
TR	Repetition time
WM	White matter

Abstract of Dissertation Presented to the Graduate School
of the University of Florida in Partial Fulfillment of the
Requirements for the Degree of Doctor of Philosophy

WEIGHTED NETWORKS AND THE TOPOLOGY OF BRAIN NETWORKS

By

Luis M. Colon-Perez

August 2013

Chair: Thomas H. Mareci, Ph.D.
Major: Physics

The brain is a network characterized by high clustering and short distances between nodes. The topological framework used to quantify these properties assumes that connections are equivalent and that networks are sparse, which is not an accurate assumption for the brain. Consequently, there is a need to generate metrics that resemble the physical substrate of brain networks, which would lead to properly weighted networks. This dissertation describes a novel edge-weight, which is a dimensionless, scale-invariant measure of node-to-node strength connectivity in brain networks derived from magnetic resonance imaging (MRI). Edge-weight simulations were performed on multiple fiber structures, displaying higher accuracy with high seed points per voxel and when random errors were kept below a standard deviation of less than 0.03. This implies that high seed density and signal to noise ratio is required to employ the edge-weight.

The framework used to estimate the topological features of networks is generalized to study weighted brain networks. The framework allows the study of topological properties in dense weighted networks, which otherwise would not be

possible. Human and rat diffusion weighted images (DWI) were acquired in a 3T and 17.6T magnet respectively. The DWI data was used to construct the brain networks and the generalized framework was able to demonstrate the small world property in situations where the binary framework failed. In dense binary networks (when the number of edges is 50% or more than all possible node-pairs combinations), the brain displayed organization similar to a random network while dense weighted networks displayed increased clustering suggesting a small world organization. This suggests a new way of looking at structural brain networks derived from MRI as a dense mesh of weighted connections, arranged in an efficient and robust manner.

Finally as a perturbation model, thyroid disrupted rat brain networks were analyzed and revealed that the brain exhibits small world properties even after perturbations. This implies that the network is organized to preserve effective global communication and specialized processes. The weighted networks and framework presented in this dissertation provides a more realistic model to describe brain networks and eliminates the sparseness requirement to determine network organization.

CHAPTER 1 INTRODUCTION

Although the brain's ability to wonder and inquire has permitted us to understand many aspects about our bodies, the environment, and the universe, much is left to understand about the brain itself. The brain is the substrate where all knowledge originates. Neuroscience has guided most of our understanding of the brain; however, physics can finally provide its own contribution with the development of novel techniques and modeling to further comprehend the complexity of our brains.

The idea of looking at the structure of complex systems as a network became a useful tool as the limitations of working with isolated components of the system became understood (i.e. reductionism is not enough) (Barabási, 2011; Glickstein, 2006). The study of networks has yielded a wealth of knowledge regarding the topological organization of large-scale systems (Craddock et al., 2013). The topological traits of real complex networks have been widely studied by mostly assuming binary interactions between the components of the network. However, the representation of these systems as either connected or not connected (i.e. simple graphs) is not sufficient. The binarization of interactions yields a topological framework that allows us to study complex networks and estimate the organizational features of real world networks. However, the framework itself is not flawless; it comes with ambiguities in the definition of connections and assumes that networks are sparse.

The connections in the binary framework, by definition, are present or absent, assuming all connections as equivalent in their strength. This binary framework has been used because it was the natural progression of the field and simplification of network interactions as equivalent provided helpful information regarding the structure

of real systems. However, it is unrealistic to assume equivalency in the connection strength between components of most real systems. Also, the sparseness condition is associated with the fact that the strongest connections are most confidently measured. Devising methods to quantify the strength of a connection requires a system-by-system analysis. Once acceptable measurements become available, network properties can be estimated from more complicated graphs (i.e. weighted, multigraphs).

1.1. The Problem

While representing real world systems as networks, one must consider the heterogeneity of connections in the real world. This is a useful and necessary concept to represent the real system as a network. The structure of real networks should not be assumed to have equivalent connections, nor should these connections be considered sparse. Therefore, it is essential to develop novel methods that can define edges with their associated strength within the network (i.e. weighting the network). Also, to characterize the real structure of networks, the binary framework must be generalized to account for the new degree of freedom that is associated with the heterogeneity of edges in the weighted network.

The ability to quantify the brain's complex structure permits us to infer the basic principles of brain organization and formation. The structural organization of networks can be studied at different levels or scales, which are representative of the interaction between components. The brain has three levels: microscale, mesoscale and macroscale (explained in Chapter 2). To discover universal principles of network organization, an adequate framework must be created to study networks at all levels. Many networks, although different in nature, share basic principles; therefore, being

able to understand how networks form and how they are structured for a given system might provide the necessary insight to understand all networks. A proper framework might elucidate new principles of the real structure of networks that would not have been possible with a binary approach.

Generalized frameworks permit the estimation of structural organization allowing researchers to gain insight into the features of real world networks from models that closely resemble the real substrate. Such an approach would take us a step closer to accurately describing the brain as a complex network, without losing the important information obtained from binary approaches, and providing new information to understand the brain's structural organization in greater detail. Also, the generalization of the framework would be a necessary advancement to deal with networks in a more realistic manner, as long as an appropriate characterization of the physical strength of connectivity is accomplished.

1.2. Outline

In this dissertation, developments made in complex network analysis are presented. In Chapter 2, the background of diffusion is reviewed and briefly discussed as it relates to the different structures of the brain. Also, a brief discussion on graph theory developments is revisited. This is followed in Chapter 3, with an introduction of the MR methods used in Chapters 4 through 6. In Chapter 4 a new definition of an edge weight, based on a previous edge weight by Hagmann et. al. (Hagmann et al., 2008), derived from DWI and tractography is presented. Chapter 5 introduces a generalized framework to analyze weighted networks, which is a new approach to estimate topological characteristics in weighted networks. The combination of Chapters 4 and 5

present a novel method to weigh brain networks derived from MRI and tractography in relation to the physical substrate. In Chapter 6, effects of network perturbations are addressed in brain networks that give rise to structural reorganizations. The perturbations are due to white matter loss resulting from thyroid hormone disruption in rat brains. In Chapter 7 a roadmap to merge structural networks with functional models is shown. Finally, Chapter 8 summarizes the findings and gives an overview of the current state of the field and possible future directions.

CHAPTER 2 BACKGROUND

2.1. Diffusion and MRI

Diffusion is the tendency of particles to move at random via collisions within a medium. It gives us the ability to understand the properties of materials and study environmental structures (e.g. porous media). Currently, the study of diffusion allows scientists to better understand the brain's vasculature (Assaf et al., 2008), compositional changes in the presence of disease (Jellison et al., 2004), and overall structural organization (Hagmann et al., 2007; Iturria-Medina et al., 2007). The random motion of water molecules helps describe tissue boundaries and arrangement, which ultimately allow the estimation of the complex structure and network of the brain (Assaf and Basser, 2005; Basser et al., 1994; Conturo et al., 1999; Ozarslan et al., 2006).

2.1.1. Principles of Diffusion Displacement

Diffusion allows particle mixing without bulk motion (Crank, 1980), a process commonly related to mass transport. Employing Fick's laws of diffusion, this process can be expressed mathematically, in an isotropic medium, where the media structure permits substances to have the same diffusive properties at any location (Phillips et al., 2008). Fick's first law of diffusion relates diffusive flux to a gradient in concentration as

$$J = -D \cdot \nabla C. \quad (2-1)$$

In Equation 2-1, J represents the particle flux, C is the particle concentration, and D is the diffusion coefficient. The diffusion coefficient is a property of the medium, depending on the particles undergoing diffusion and the environmental structures. Fick's first law

describes the flux, J , in a system with an inhomogeneous spatial concentration of at least two substances. The direction of the flux will be opposite to the gradient of the concentration (i.e., particles in the area of higher concentration will migrate to areas of less concentration) until equilibrium is reached and a homogenous distribution is obtained. Fick's second law of diffusion (Equation 2-2) is obtained by employing two conditions: (i) the conservation of particles and (ii) continuity such that the change in concentration over time is due to particle flux in the system as

$$\frac{\partial C}{\partial t} = \nabla(D \cdot \nabla C). \quad (2-2)$$

At this point, from Equation 2-2, it appears that once a gradient of concentration vanishes, the flux will vanish as well and diffusion would stop. However, the particle's random motion, driven by thermal energy, continues even at equilibrium. Since diffusion is constrained by the structural geometry of the environment, diffusion with nuclear magnetic resonance (NMR) provides a unique foundation to obtain information about the internal structure of a system. Therefore the diffusional properties of water molecules can be exploited in the study of brain structure using magnetic resonance imaging. In 1827, Robert Brown, a Scottish botanist, observed pollen grains and inorganic particles moving when suspended in water (Brown, 1828). Although in the system there is no net flux or gradient of concentration, Brown observed molecules moving. He called these active molecules organic and inorganic bodies. In 1905, Albert Einstein, examining the existence of atoms, showed that particles of microscopic size would move when suspended in water (Einstein, 1905). Einstein's work proved that Brown's active molecules were the manifestation of molecule collisions (driven by the thermal energy) with the liquid molecules in the system. Einstein's 1905 publication on

the studies of small particles in liquid would consolidate Brown’s observations with the predictions obtained by molecular kinetic theory of heat. Einstein goes on to state that “bodies of microscopically-visible size suspended in a liquid will perform movements of such magnitude that they can easily be observed in a microscope, on account of the molecular motions of heat”. Then he states that the molecular motions he discussed could be identical to Brownian motion, and over time this statement has been accepted as the reason for the observed motion of Brown’s particles. Also Einstein’s description of the diffusion of small spheres in suspension led to Equation 2-2 hence unifying the Fickian and Brownian descriptions of particle diffusion. These diffusion descriptions helped characterize diffusion behavior in NMR experiments (Carr and Purcell, 1954; Torrey, 1953) as will be shown in the next section. This ultimately led to diffusion weighted MRI (DWI).

2.1.2. Diffusion Weighted Imaging

In 1956, H. Torrey modified the phenomenological NMR’s Bloch equations (Equation 2-3 and known as the Bloch-Torrey equation) to explain the change in magnetization due to the thermal motion of water molecules (Torrey, 1956). The modification consists of the addition of a diffusion term analogous to the right hand side of Equation 2-2. In Equation 2-2 diffusion is due to changes in concentration while in Equation 2-3 it is due to the transfer of magnetization by diffusion.

$$\frac{d\vec{M}}{dt} = \gamma \vec{M} \times \vec{B} + \frac{1}{T_1} (\vec{M} - \vec{M}_z) - \frac{1}{T_2} (\vec{M}_y + \vec{M}_x) + \vec{\nabla}^T \cdot \vec{D} \cdot \vec{\nabla} M \quad (2-3)$$

where, M stands for the magnetization of water molecules in an applied magnetic field, γ

represents the gyromagnetic ratio of the particles, B is the applied magnetic field, T_1 longitudinal relaxation time, T_2 is the transverse relaxation time and D is the diffusion coefficient. The first term on the right contains the effects of the magnetic field on the total magnetization, M ; this causes the precession of spins around the main magnetic field B . The spins will precess at a frequency characteristic of its nucleus leading to the rate of precession known as the Larmor frequency (ω , Equation 2-4) (Haacke et al., 1999). The Larmor frequency is determined by

$$\omega = \gamma B \quad (2-4)$$

is the angular velocity of particles rotating in a magnetic field. The Bloch-Torrey equation represents the macroscopic change in time of the magnetization in a system where the particles that make up the macroscopic magnetization also undergo diffusion. The second term is the yields the time dependence of the longitudinal magnetization (around main magnetic field) as it returns to equilibrium and the third term yield the time dependence of the transverse magnetization. From now on relaxation effects are disregarded, since the experiments in this dissertation will consist of attenuation measurements that estimate an effective scalar diffusion coefficient that is averaged over the echo time. Later it will be shown that this measurement is only due to diffusion contributions and independent of relaxation times.

In 1965, Stejskal and Tanner developed modern diffusion MRI measurements (Stejskal and Tanner, 1965), to capture the diffusion effect in NMR by applying short duration gradient pulses, as Figure 2-1 shows. In a spin echo experiment, as the one shown in Figure 2-1, the time to repeat the entire encoding scheme (time between 90° pulses) is known as TR and the time between the 90° pulse and the time it takes to

obtain a signal is TE. The Stejskal and Tanner method precisely defines the time period in which the gradients are applied, and the time between gradients, so that diffusion can be quantified. The first diffusion pulse gradient produces a phase shift that depends on the position of each particle along the direction of the pulse gradient. In the absence of diffusion, the second gradient would undo the phase shift due to the first gradient and the loss of coherence would be negligible. However, as particles diffuse, the refocusing of the second pulse becomes incomplete and causes an attenuation or signal loss. With this method, the first pulse applies a spatially dependent phase change, such that when the second pulse is applied, it forms a net phase change in the form of

$$\varphi_2 - \varphi_1 = -q(x_2 - x_1) \quad (2-5)$$

where $q = \gamma\delta g$, δ is the diffusion pulse length, g is the gradient strength, and x_1 and x_2 are the particles' positions at the time of the first and second pulse, respectively (Bernstein et al., 2004). In the Stejskal and Tanner approach the application of the pulses are made "short" enough so that molecular displacements are negligible small during δ compared to the diffusion time, Δ (i.e. $\delta \ll \Delta$). The signal, which is given by the magnetic moments of all spins, is attenuated due to the incoherence in the orientations of the individual magnetic moments due to their thermal motion. This leads to a phase change because of the change in their positions. Solving Equation 2-3 assuming $T_1 \sim \infty$ and a spin echo sequence as shown in Figure 2-1, yields Equation 2-6, which shows the signal obtained during a spin echo DWI experiment.

$$S(q) = S_0 e^{-D \left[(\gamma\delta g)^2 \left(\Delta - \frac{\delta}{3} \right) \right]} e^{-TE/T_2} \quad (2-6)$$

where S_0 is the rate without diffusion weighting. Given the time scales (long TR's and

long TE's) in diffusion weighted experiments, the contrast will come predominantly from T2 and diffusion.

Diffusion experiments seek to study the effect of the gradient pulses on the echo amplitude. Hence, the diffusion signal is more conveniently written by the echo signal, $E(q)$ (Equation 2-7). The echo signal is a quantity obtained by taking the ratio of the attenuated signal and the signal without any diffusion weighting, $E(q) = S(q) / S_0$. Therefore, the attenuation (Equation 2-7) is due to only diffusion effects and removes relaxation effects by dividing by S_0 . Equation 2-7 employs a normalized spin density such that when no diffusion weighting is applied $E(q) = 1$.

$$E(q) = \int \rho(x_1) \int P(x_1, x_2, \Delta) \cdot e^{-iq(\bar{x}_2 - \bar{x}_1)} dx_2 dx_1 \quad (2-7)$$

where $\rho(x_1)$ is the normalized spin density at the time of the first pulse and $P(x_1, x_2, \Delta)$ is the diffusion propagator (Green's function) (Callaghan, 1991). The propagator is a function that represents the likelihood that a particle initially at position x_1 ends up in position x_2 after a time Δ , which is the time between gradients. The rate of signal loss, or attenuation, for a given gradient strength is greatest when the gradients are applied along a direction of small or no obstruction, and it is least for a gradient perpendicular to a barrier or a restriction. In the Stejskal & Tanner approach, the solution to Equation 2-7 can be written as (Basser, 2002)

$$E(q) = e^{-bD} \quad (2-8)$$

where

$$b = (\gamma \delta g)^2 \left(\Delta - \frac{\delta}{3} \right) \quad (2-9)$$

In Equation 2-6, the term in brackets will be referred throughout this text as the b value

(Equation 2-9), which is a quantity of the influence of the gradients in the diffusion-weighted image. Important to note is the fact that the diffusion coefficient in Equation 2-8 is written in terms of a scalar apparent diffusion coefficient. This means that the measured $E(q)$ will be dependent on the applied direction of the diffusion gradient or b value direction. The bD term in the echo signal is the inner product of those quantities. Therefore, every measurement along a different diffusion gradient direction will yield a different diffusion coefficient which describes the influence of the diffusion gradient direction in relation with the microstructure orientation within the voxel. For example the echo signal will be minimal (attenuation will be maximal) when the gradient is parallel to a WM fiber and maximal (attenuation will be minimal) when WM structures are perpendicular to the gradient direction.

In practice, during the pulse gradient sequence, the molecules displace in the order of 100 Å to 100 μm over time scales of a few milliseconds to a few seconds (Callaghan, 1991). The dimensional scale of the pulse gradient scheme corresponds to an organizational domain that includes features of macromolecular solutions, porous solids, and biological tissue. The orientation dependence of the measured diffusion coefficient will enable the modeling of the microstructure in a more complex manner. Therefore, using pulse gradient NMR, one can probe the internal structure of the brain. With the obtained MR signal, multiple models of diffusion can characterize the properties of diffusion within the tissue: diffusion tensor, a distribution of second rank tensors, and a model of constricted and hindered diffusion (Assaf and Basser, 2005; Basser et al., 1994; Jian et al., 2007b).

The first model of diffusion to be introduced was the diffusion tensor (\hat{D}) or, diffusion tensor imaging (DTI) which corresponds to a second order tensor that estimates the average diffusion coefficient in a voxel¹ of the MR image (Basser et al., 1994).

$$\hat{D} = \begin{pmatrix} d_{x,x} & d_{x,y} & d_{x,z} \\ d_{y,x} & d_{y,y} & d_{y,z} \\ d_{z,x} & d_{z,y} & d_{z,z} \end{pmatrix} \quad (2-10)$$

where d_{ij} corresponds to the components of the diffusion tensor. In order to estimate the diffusion tensor, a minimum of seven measurements are needed: a low or no diffusion weighting and six diffusion weighted images. The six images includes: three along the orthogonal directions (e.g. {x,y,z}) and three for crossed terms (e.g. {xy, xz, yz}) in Equation 2-10. The tensor has antipodal symmetry, (i.e., it will always be symmetric) and therefore only needs six component measurements, instead of all nine. This model assumes Gaussian diffusion profiles in each voxel to estimate the diffusion tensor. This has been a very successful model in obtaining diffusional properties of regions with strong and coherent WM structures like the spinal cord, corpus callosum and cingulum; however, it fails in regions where multiple fiber orientations appear. The Gaussian diffusion condition limits the model to regions of single fiber orientation or free diffusive water (e.g. cerebral spinal fluid). Diagonalization of the diffusion tensor as

$$\hat{D} \cdot u = \lambda \cdot u, \quad (2-11)$$

allows for the estimation of the average diffusivity ($AD=\langle D \rangle$),

¹ Voxel is the 3D analog to a pixel

$$\langle D \rangle = \frac{\sum_{i=1}^3 \lambda_i}{3}, \quad (2-12)$$

which is a measure of the self-translating diffusion within each voxel. Finally the fractional anisotropy (FA, Equation 2-13) (Basser and Jones, 2002) can also be obtained by

$$FA = \sqrt{\frac{3}{2}} \sqrt{\frac{(\lambda_1 - \langle D \rangle)^2 + (\lambda_2 - \langle D \rangle)^2 + (\lambda_3 - \langle D \rangle)^2}{\lambda_1^2 + \lambda_2^2 + \lambda_3^2}} \quad (2-13)$$

which is a measure of the deviation from isotropic diffusion in each voxel. These measures allow the discrimination of GM regions (high AD and low FA) from WM (high FA and low AD). The recognition of anatomical structures is limited by the ability to find contrast between tissue types, hence FA and AD greatly aids in tissue contrast hence improving the ability to segment brain regions. In Equations 2-11 to 2-13, u represents the eigenvectors or the principal diffusion directions and the λ 's are the eigenvalues.

In the brain, water molecules are present in the intra and extra axonal compartments, which lead to restricted and hindered diffusion, respectively. The intra axonal or restricted diffusion is observed over length scales of less than 2 μm . Technological advantages of stronger magnetic fields allow the probing of the diffusion within this compartment by applying stronger diffusion weightings. This prompted the development of a new methods with improved acquisition techniques to model diffusion like Diffusion Spectrum Imaging (DSI) (Wedeen et al., 2005), High Angular Resolution Diffusion Imaging (HARDI) (Tuch et al., 1999) and the Composite Hindered and Restricted Model of Diffusion (CHARMED) (Assaf and Basser, 2005; Assaf et al., 2004). The DSI model uses the diffusion propagator of Equation 2-7 and samples diffusion on

a Cartesian space (i.e. q space, Equation 2-5). Employing the propagator's Fourier relation between the obtain signal and the mean particle displacement DSI is able to characterize diffusion. HARDI, on the other hand, measures apparent diffusion coefficient along many directions. From HARDI acquisitions more sophisticated models of diffusion can be applied to represent diffusion profiles on each voxel. A method is called the Method of Wisharts (MOW), Equation 2-14 (Jian et al., 2007a; Jian et al., 2007b) to avoid DTI's uncertainty in regions with multiple fibers a method. MOW is based on HARDI acquisitions and was consists of fitting a distribution of tensors on each voxel given by

$$E(q) = \frac{1}{n} \sum_{i=1}^n e^{(-b\hat{g}^T D_i \hat{g})} . \quad (2-14)$$

This model assumes that a mixture of diffusion tensors can characterize the diffusion in each MR voxel. In this model, multiple tensors in the MOW distribution will yield the fiber orientation. This allows resolving the regions of multiple directions within a voxel. In this model, increased noise levels makes it more challenging to estimate the fiber orientation when there are more than three fiber orientations. In this model, there is no distinction between the different compartmental contributions to the signal attenuation from the different biological compartments. The last model to be described here, CHARMED, assumes two water compartments (one hindered and another restricted) on each voxel where the diffusion attenuation arises. DSI and CHARMED requires the acquisition of multiple shells of diffusion weightings where each additional shell is the amplification or increase of the diffusion weighting, b value, and the number of gradient directions. Although this model is the most physically feasible, it requires a

high number of diffusion weightings, thus making the acquisition protocol highly time consuming. Since MOW is able to reconstruct multiple fiber orientations in each voxel and is more applicable in many practical situations (i.e. clinical) will be employed in this investigation.

To apply any of these methods, optimized acquisition protocols are needed to better estimate diffusion profiles to reduce noise and angular uncertainty. The optimization of b values (Equation 2-9) will better estimate the diffusion properties in different regions of the brain. Since white matter fiber tracts, which are bundles of neuronal axons, hinder diffusion of water molecules in neural tissue, the measured DWI will depend on the structures and their orientation along the gradient directions. It has been shown that at low b values the angular dependence of the signal in a plane containing 2 distinct fiber directions is small, and diffusion direction estimation is very noise sensitive, as seen in Figure 2-2 (Tournier et al., 2004). Contrastingly, high b values enhance angular dependence; however the signal attenuation can get large enough so the noise begins to dominate. Therefore, intermediate b values provide better results because strong angular dependence is introduced without attenuating the signal to noise level. A good compromise between b value and signal to noise ratio (SNR) is needed to achieve high angular acquisition to accurately estimate diffusion and obtain reliable fiber tracking. High angular resolution will aid in regions where fibrous tracts cross (i.e., fibers travel one on top of another in a MR voxel, or kiss, i.e. the fibers get close but do not cross). As the b value is optimized, the gradient direction scheme can also be adjusted.

Performing additional measurements along a high number of gradient directions, reduces bias introduced by measuring signal attenuation along a limited number directions and diffusion estimation profile is improved in highly anisotropic areas (Jones et al., 1999). Gradient schemes can also be optimized to improve the acquisition scheme by increasing the number of diffusion directions. This work will employ an optimized scheme of gradient directions described by Jones et al (Jones and Leemans, 2011). To optimize the diffusion directions of the gradient vectors, Jones applies the criterion that these directions should be uniformly distributed in 3D space, analogous to electrostatic repulsion that uniformly distributes charged particles onto a sphere. Jones' model considers a line parallel to each gradient vector that passes through the center of a sphere and a unit electrical charge is placed at both points where the line intersects the sphere. A total of 64 charges (this number can be varied as desired) are allowed to move, according to Coulomb's repulsion law, until the sum of the electrical repulsion of all charges is minimized. Thus, 64 direction gradient vectors are obtained to distribute the diffusion weightings for imaging. These two approaches, b value and gradient direction schemes, will be employed to improve the angular quality of the diffusion weighted images.

2.2. Networks

Graph theory is the framework for the mathematical treatment of networks. A network refers to a real system that is represented by a mathematical graph. The origin of graph theory is attributed to Leonhard Euler and his study of the Königsberg riddle. The city of Königsberg, presently called Kaliningrad in Russia, was separated by the Pregel River and contained two islands, as shown in Figure 2-3, which were connected

by a set of seven bridges. In 1736, Euler solved the path riddle of the bridges (Newman, 2010), which inquired about the possibility of finding a path through the city crossing each of the bridges only once. The residents of Königsberg tried without success to find such path. In order to solve the riddle, Euler abstracted the city as a set of nodes (the land masses) and edges (bridges), which became the Königsberg graph, Fig 2-4b. Euler noticed that if a walker were to traverse only once through the bridges, they would have to enter and leave each node an even number of times except at the beginning and the end of the path (i.e., first and last nodes). All nodes in Figure 2-4b have an odd number of connections. Euler's abstraction of the network as a graph, proved the impossibility of finding the riddle's path. This proof was the first work using graphs to represent a real network (Albert and Barabási, 2002) and provides the basis for dealing with real systems as connected units forming a network.

2.2.1. Graph Theory Metrics

Graph theory represents a network as a graph, $G = [N, E]$, where N is the set of n nodes and E is the set of m edges in the network (Rosen, 2003). The basic components of a graph are the nodes (e.g., people, web sites, or specific parts of the brain) and the edges (i.e., the connections or interactions between different nodes) (Butts, 2009). Mathematically, there are two basic descriptions that can be used to represent a graph: the incidence matrix, M , and the adjacency matrix, A . The incidence matrix, $M = [m_{ij}]$, for a simple and undirected graph (described in the next paragraph) is a rectangular $n \times m$ matrix for a set of nodes, $N = \{n_1, n_2, n_3, \dots, n_n\}$ and edges, $E = \{e_1, e_2, e_3, \dots, e_m\}$ with a specified ordering of the nodes and edges. The element of the incidence matrix m_{ij} is non-zero when e_j is incident on n_i and zero otherwise. The adjacency matrix is a square,

symmetric matrix, $n \times n$, for simple and undirected graphs, where n is the number of nodes in the network, and A is written as

$$A = \begin{pmatrix} a_{11} & \cdots & a_{1n} \\ \vdots & \ddots & \vdots \\ a_{n1} & \cdots & a_{nn} \end{pmatrix} \quad (2-15)$$

where

$$a_{ij} = \begin{cases} \text{non zero,} & \text{if there is an edge connecting } n_i \text{ to } n_j \\ 0, & \text{otherwise.} \end{cases} \quad (2-16)$$

The adjacency matrix represents specific connections between nodes, where the a_{ij} element of this matrix is non-zero if the node n_i is connected to n_j by an edge, and zero otherwise. The non-zero elements of A will be determined depending on the type of graph being employed to describe the network. There are four main types of networks described by graph theory: simple, multigraph, directed, and weighted. The nature of the connections in the network will determine the type of graph to be employed.

The most basic type is the simple graph. In this graph, the edges are directionless (i.e., an edge from n_i to n_j is equivalent to the edge from n_j to n_i as shown in Fig 2-4a). The elements of the matrix are one when an edge connects the nodes and zero otherwise. In addition, self-connections or multiple edges connecting the same two nodes are not allowed. Therefore, adjacency matrices of simple graphs are always symmetric and their trace is 0. Simple graphs will be referred through this text as binary, since the connectivity is characterized by the presence or absence of edges.

A second type of network is the multigraph, which allows the presence of self-connections or loops, also multiple edges connecting the same two nodes (e.g., the Königsberg riddle of Figure 2-3 and 2-4b). However, similar to simple graphs, the edges of multigraphs are directionless. The adjacency matrices of multigraphs are always symmetric and their trace is not necessarily zero. The element a_{ij} of multigraphs will reflect the number of edges connecting n_i to n_j and the trace of A will be twice the number of loops in the graph. By definition, a loop connecting n_i to itself is assigned the number two. In simple graphs, an edge connecting node n_i to node n_j provides two elements of the adjacency matrix; $a_{ij} = 1$ and $a_{ji} = 1$. Therefore, each end of every edge contributes twice to the adjacency matrix. Similarly, by definition a loop is counted twice. A loop will have two ends connecting to the same node yielding a value of two for a_{ii} . Another type of graph is a directed graph. In these graphs, as the name suggests, edges describe a direction of flow. In simple and multigraphs, information can flow in either direction along the edges. In directed graphs, the adjacency matrix is defined as follows: $a_{ij} = 1$ if the edge is directed from i to j , while $a_{ij} = 0$ otherwise.

Up to this point, all the discussed networks (simple, multigraph, and directed) are described mathematically by integers (i.e., the number of edges connecting any two nodes). However, for the last network type, weighted networks do not need integers describing the connectivity. In these networks, the elements of A reflect strength of connectivity between any connected pair of nodes in a graph. For the sake of simplicity in this introductory chapter the network metrics described will be for simple graphs (i.e. binary networks).

The adjacency matrix allows the determination of network parameters such as: 1) the node degree, which is the number of edges that connect to a specific node; 2) the path length, shortest path along the edges of the network to connect n_i to n_j ; and 3) the clustering coefficient, which measures the tendency of nodes to cluster. The simplest measure that describes a network is the degree, k , (Equation 2-17) of each node. It is calculated as

$$k(n_i) = \sum_{j=1}^N a_{ij} \quad (2-17)$$

where a_{ij} is the ij^{th} element of the adjacency matrix. The degree distribution provides a simple topological representation of the number of links that any given node holds and provides insights on the connectivity arrangement in the network.

Another commonly used metric is average path length, which measures the average number of steps that connects any node to all others. Average path length relates how efficiently information is transferred globally within the network. The path length is calculated as given by

$$l(n_i) = \frac{\sum_{j=1}^N s_{ij}}{N-1} \quad (2-18)$$

where s_{ij} represents the minimal number of steps it takes to travel along the edges of the graph from node i to node j , and N is the number of nodes in the network. In the brain, the path length is associated with the efficiency of the overall structure of the network (Bullmore and Sporns, 2009). Ideally, if only a few steps are needed to travel from any node to any other node, information will most likely be transferred very efficiently within the network.

The clustering coefficient, c_i , measures the level of connectivity of the neighbors of node n_i or local connectivity around the neighborhood of n_i . It measures the ratio of the overall number of triangles that any node forms with its neighbors to the total number of possible connections. The clustering coefficient of node n_i considers the neighbors n_j and n_k . If n_j and n_k are connected, then they form a triangle centered around n_i which contributes to the clustering coefficient value of node n_i . The normalization $[k_i(k_i-1)/2]$ in the clustering coefficient is the total number of pair connections among the neighbors if node i . The binary form of c_i is specified by

$$c_{i,B} = \frac{2E_{jk}}{k_i(k_i - 1)} = \frac{1}{k_i(k_i - 1)} \sum_{j,k=1}^N a_{ij} a_{jk} a_{ki} \quad (2-19)$$

where $E_{i,k}$ is the number of edges connecting the neighbors of node i . In the brain, the clustering coefficient has been associated with specialized processing (e.g. sensory input analysis, like visual, auditory, and so forth) (Bullmore and Sporns, 2009). Nearby nodes work together to achieve complex tasks; therefore, high node clustering of the neighbor nodes allows the efficient communication and ultimately complex task processing.

2.2.2. Random Networks

In 1959, Paul Erdős and Alfred Rényi introduced the first model to generate random graphs (also known as ER graphs)(Erdős and Rényi, 1959) This model was the first one used to address questions relevant to network analysis using probabilistic methods as the number of edges is increased. As an example, the ER model described the probability of obtaining a giant component in a graph (a giant component is a

maximal set of nodes that are connected by a finite number of steps). Essentially this is the point at which the graph starts to appear connected and the isolated nodes or clusters of nodes are greatly reduced.

The construction of a random graph, $G(n,p)$, starts with n nodes, and all edges have equal probability p of connecting any pair of nodes, independently of the others (Boccaletti et al., 2006). This is the first model using graphs to study the properties of large-scale networks. The properties of these graphs are usually studied as an ensemble of random graphs constructed with a specified number of nodes, and a probability, p , that any pair of nodes is connected. In this model, the probability to find any graph, G , is given by

$$P(G) = p^m (1-p)^{\binom{n}{2}-m} . \quad (2-20)$$

where m is the number of edges in the graph. Equation 2-20 leads to the probability of having a graph with m edges from the ensemble of the form of Equation 2-21 (i.e. a standard binomial distribution) (Newman, 2010), given by

$$P(m) = \binom{\binom{n}{2}}{m} P(G) = \binom{\binom{n}{2}}{m} p^m (1-p)^{\binom{n}{2}-m} . \quad (2-21)$$

From Equation 2-21, and some simple arithmetic the mean number of edges can be found as

$$\langle m \rangle = \sum_{m=0}^{\binom{n}{2}} m P(m) = \binom{n}{2} p , \quad (2-22)$$

which is the total possible number of node-pairs times the probability, p , that they are connected (Equation 2-22) (Newman, 2010). Since the edges are randomly distributed

throughout the entire graph, the mean degree can be estimated using Equation 2-22, which leads to a mean degree of $2m/n$ for the entire graph. In this case, most of the nodes in the graph will have an average degree

$$\langle k \rangle = \sum_{m=0}^{\binom{n}{2}} kP(m) = \sum_{m=0}^{\binom{n}{2}} \frac{2m}{n} P(m) = \frac{2}{n} \binom{n}{2} p = (n-1)p, \quad (2-23)$$

which is equal to the total number of nodes in the network minus one (itself, since it is a simple graph) times the probability, p , that any pair of nodes are connected.

These mathematical descriptions of networks do not satisfy the observed organizational and communication properties of real networks (Barabási and Albert, 1999; Milgram, 1967). This is not a surprise since it is not realistic to assume that all connections are equivalent and equally probable. Erdős and Rényi recognized the failure of their hypothesis in their work, “On the evolution of random graphs” (Erdős and Rényi, 1960) where they refer to the evolution of certain communication networks, like electric network systems;

“If one aims at describing such real situation, one should replace the hypothesis of equiprobability of all connections by some more realistic hypothesis”

Erdős and Rényi were more concerned with the mathematical treatment of networks rather than fully understanding the intricacies and details of real network formation. However, their work served as the mathematical basis of network studies until new mathematical models of networks were introduced almost 40 years later.

2.2.3. Small World

At some point in our lives, we all have said “what a small world!” whenever we find out that the person we have just met is a family member of our best friend, that a co-worker we have worked with for some time is actually best friends with our cousin, and many more familiar situations that we can all relate to. This phenomenon is actually referred to in science by the same expression—the “small world” phenomenon (Watts, 2003). Stanley Milgram first introduced this phenomenon to science in 1967 with his letters on the mail experiment (Milgram, 1967). Milgram asked a group of individuals to send a letter from Kansas to Massachusetts, with the restriction that each sender had to send it to an acquaintance who was most likely to know the final recipient. At the time, the only network model was the random model introduced by Erdos and Renyi, which led to the expectation that letters would travel at random through the 200 million inhabitants of the United States until it would reach the final recipient. However, to Milgram’s surprise, the letters that reached the final recipient arrived with an average number of five intermediaries. This result contradicted common knowledge at the time about network organization. It would take another 30 years to find a suitable mathematical network model to describe this phenomenon.

In 1998, Watts and Strogatz introduced the small world model to explain observations of the properties of real networks (Watts and Strogatz, 1998). The model attempted to replicate the observed organizational feature of high clustering, which is associated to the structure of regular graphs, and also short path lengths, associated with random graphs. Studies of real-world networks (e.g., the world wide web (www)) repeatedly revealed a mixture of properties from random and regular graphs. The small world model displayed the observed property that some real-world networks are neither

regular (i.e. all nodes have same degree) nor random. Figure 2-5 illustrates these differences. Regular networks emphasize lattice-like arrangement of the nodes, as in the atoms of a lattice from solid-state physics, where the connections between components of the lattice are well known and ordered. Regular graphs exhibit the properties of high clustering coefficients and long path lengths, while random graphs do not emphasize any arrangement among nodes. Random graphs, in contrast to regular graphs, exhibit low clustering coefficients and small path lengths. The small world networks display some arrangement, yielding a high clustering coefficient as seen in regular graphs. Additionally, it establishes some arbitrary connections that allow the network to display small path lengths as seen in random graphs.

2.2.4. Scale Free

In 1999, studies of large-scale networks, such as the www, revealed another feature that the previous two models had failed to show. Barabási found a long tail in the degree distribution of real networks, such that a small, but significant, number of nodes contained a very high number of connections, referred to as hubs. He coined the term “scale free” (Barabási, 2009) to name these networks, due to the inability to obtain a meaningful mean degree from these networks. In Figure 2-6, a power law is shown, a long tail can be seen, where the black line represents an exponential decay associated with small world networks. The exponential decay description shows that the graph is unlikely to have degrees much different from the mean. However, the power law that characterizes scale free networks implies that degrees much different from the average are still likely to occur. In Figure 2-6 the probability of having nodes with degree 10

increases by 10 and 100 times for power laws with λ equal to three and two, respectively.

A fundamental difference between the scale free model and both the ER and small world models is the fact that the scale free model relies on growth and preferential attachment (Barabási, 2003). The fact that the number of www websites or nodes is dynamic allows one to think in a growth situation with a “first come, first serve” assignment of the connections within the web. Originally, the graph is very small and, as time progresses; one might think that the older nodes might lead to a hub-like status over time. However, growth alone is insufficient to account for the extremely large hubs in the www and other real world networks. Preferential attachment is introduced to bias newcomers in the network to preferentially attach to high degree nodes. These two conditions of preferential attachment and growth were sufficient to replicate the degree distributions observed in the www and many other systems.

2.2.5. Brain Networks

Similar to the dispute on the nature of light, where Huygens argued for a wave description of light while Newton claimed that particles were the basic nature of light, neuroscience had a controversy regarding the nature of the basic organization in the brain. Ramon y Cajal argued for a neuron doctrine while Golgi argued for a reticulum or a network description (Glickstein, 2006). Ramon y Cajal’s interpretations and simplicity of experiments led to the widespread consensus regarding the neuron being the basic component of the brain. However, after a century of many advances, science has come to the conclusion that to fully understand the brain, the neuron is insufficient (Sotelo, 2011). The interactions of neurons within brain regions are key to understand our

cognition and complex functioning. A rebirth of the network notion as a basic structure to describe the brain appeared to provide a new way to further understand the intricacies of brain structure and function. Although the neuron has been commonly accepted as the basic component of brain structure, a network description would not defy this consensus because the basic object of study in the brain network would be the neuron and its interactions among other neurons (Sporns, 2011).

A growing interest to provide new ways to study the brain (Crick and Jones, 1993) has constantly been producing novel methods to determine brain structure *in vivo* (Bassett and Bullmore, 2006; Bullmore and Sporns, 2009; Guye et al., 2010; Hagmann et al., 2010a; Honey et al., 2010; Lo et al., 2011; Rubinov and Sporns, 2010; Sporns et al., 2005; van den Heuvel and Sporns, 2011). High angular resolution diffusion imaging, HARDI, (Tuch et al., 2002) and graph theory provide an ideal foundation to study the brain structure non-invasively. The contrast due to local tissue structure (i.e. gray matter (GM) and white matter (WM)) is greatly enhanced in HARDI measurements (Basser and Jones, 2002). HARDI, along with advanced models that quantify diffusion parameters (Jian et al., 2007b; Ozarslan et al., 2006; Tuch, 2004), allow the reconstruction of WM fibers using tractography, even in complex tissue regions where fibers kiss or cross. Using tractography techniques and graph theory, brain networks can be recreated by representing anatomical regions as nodes, and the WM fibers connecting these nodes as edges.

The characterization of brain graph topology can be made by estimating node degree, path length, and clustering coefficient and determining connectivity patterns in the brain (i.e. verifying which areas of the brain are connected). Network models can be

used not only to advance the knowledge regarding our brains, but also to provide information about the formation and organizational features of networks in general. The brain is a complicated network composed of billions of neurons connected by axons and dendrites. In the last two decades, developments in the treatment of real systems has led to complex networks science (Newman, 2010). Although complex networks may be very different in their microscopic details, most share a similar macroscopic organization (Barabási, 2009). Brain structural systems have features of complex networks, such as small path length and high clustering, at the cellular level, as well as in the level of anatomical regions. Therefore, complex network analysis provides an ideal framework to study the brain structure.

To understand brain structure, the brain needs to be examined at three size scales: microstructure, mesostructure and macrostructure (Sporns et al., 2005). The microstructure deals with single neurons and synapses. The mesostructure refers to anatomical cells grouping and their projections. Finally, the macrostructure deals with brain regions and their connecting pathways. At the current technological state of MRI and tractography, only the macroscopic structure is a reasonable starting point for the study brain networks. Neuron size can vary in diameter from 4 to 100 μm , but most often varies from 10 to 25 μm . Assuming a standard MRI voxel size of of 1 mm^3 and a neuron radius of 20 μm , a single voxel might contain 70,000 to 80,000 neurons. Common DWI image resolution is 8 mm^3 ; so in this case each voxel contains close to 600,000 to 650,000 neurons. For these reasons the discussion will be limited to the macrostructure of the brain.

Within the macroscale, there are two possible networks to study: local and global. Local networks refer to anatomical structures connected to form a network with only a few nodes that are closely related to specialized functions (Catani and Ffytche, 2005; Colon-Perez et al., 2012). Global networks will be associated with the study of cortical structures or large-scale structures of the brain. Given the resolution and lack of neuronal specificity of MRI, the nodes will be related to known macroscopic anatomical regions. This allows us to assume that functional regions will be constrained within anatomical regions. Several reports segregate random nodes in the cortex; however, this assumes a functional homogeneity within the cortex that is not realistic (Bassett et al., 2011b; Cammoun et al., 2011; Hagmann et al., 2007). Functional regions might overlap with random node placement and connections might be confounded with a lack of care for the integrity of functional domains in the node definition. A way to possibly overcome the ambiguity of defining nodes might be through the use of functional MRI (fMRI).

In 1990, Ogawa et. al. described changes in MR signal due to changes in blood oxygenation levels (Ogawa et al., 1990). This blood oxygenated level dependent (BOLD) signal is the basis of fMRI. The BOLD signal results from increased blood flow, blood volume, and oxygen consumption. These hemodynamic changes (or BOLD signal) are preceded by neuronal activation. As neurons activate, they consume oxygen, energy, glucose, glutamate and lactate (Magistretti and Pellerin, 1999; Magistretti et al., 1999). Glutamate has been shown to be necessary to explain the link between oxygen and energy consumption with neural activity (Magistretti et al., 1999). However, oxygen is the main contributor to the BOLD signal so neuronal consumption

of glutamate, glucose and lactate will not be addressed for this discussion, since these do not affect significantly the measured response in the brain using fMRI. Neuronal activation is associated with increases in the blood flow and blood volume locally in the active region. The blood flow increases the amount of deoxygenated blood (which is a paramagnetic molecule) inducing a field change which leads to a local reduction of the field homogeneity (due to the susceptibility difference between deoxygenated blood and the surrounding tissue). The susceptibility difference creates a frequency shift ($\Delta\omega = \gamma\Delta B$) hence reducing the T_2^* locally ($1/T_2^* = 1/T_2 + \gamma\Delta B$). This reduction in T_2^* is measured with MRI as a decrease in the signal strength in the location of active neurons. Usually neuronal activation is made possible by some sort of stimulation or function (e.g. hand movements, visual stimulation and so on). Hence, using fMRI one can deduce which regions are associated with the particular function used in the experiment. Up to this point it has been discussed that functional and structural brain networks can be further understood by the use of MRI, specifically fMRI and DWI respectively.

Functional analysis of brain networks can be made with optogenetics which allows one to deliberately select specific regions (instead of stimulating by function, which yields a response in the entire brain) to determine the functional connectivity from the targeted region with the rest of the brain. Optogenetics is a method that allows one to study the functional connectivity of the brain in such a way that neurons are made sensitive to light via viral transduction of a light sensitive ion channel (channel rhodopsin or ChR2) from algae (Lee et al., 2010). In optogenetics the CamKII promoter is used to specifically target excitatory neurons. As light is shined onto the transduced neurons, the ion channel opens up causing the neuron to become activated. This method allows

the activation of specific regions in the brain that can be used to study their functional connectivity (Appendix A for details of preliminary work).

With graph theory, the brain can be described as a network. Current network-based studies focus on determining the topological traits of the brain. Brain networks are currently studied *in vivo* with magnetic resonance imaging (MRI) to create structural connectivity maps via diffusional properties of tissue and tractography. Graph theory provides the most commonly employed framework to study connectivity in the brain. Evidence of scale free and small world organization has been found in the brain with the use of functional MRI (fMRI) (Eguiluz et al., 2005; Tomasi and Volkow, 2011; van den Heuvel et al., 2008). On the contrary, the use of diffusion MRI, tractography, and structural studies suggests only a small world organization for brain networks (Bassett et al., 2011b; Hagmann et al., 2007; He et al., 2009). A four part process is used to develop such a model, as shown in Figure 2-7; (i) define networks nodes, (ii) define network edges, (iii) estimate a connectivity matrix and (iv) calculate network parameters (Bullmore and Sporns, 2009).

Brain network analysis will benefit by devising methods to obtain global network characteristics in more realistic models. Weighted networks aids in the development of this endeavor since weights in the graph can be associated with the physical substrate of the edge. The main network metrics used to calculate networks properties are: 1) degree, 2) path length, and 3) clustering coefficients. In this dissertation an edge weight is presented to quantify the structural connectivity between any two nodes in the brain. Then a generalization of network metrics is used to measure network properties in weighted brain networks derived from tractography. Finally an assessment of the

weighted framework is made by comparing thyroid disrupted rat brains with normal brains. The discussion in this dissertation from this point on will be limited to simple graphs and the networks they represent (as a way to compare with more traditional results obtained in literature) and weighted graphs and the networks they represent. Directed graphs will not be considered since brain networks obtained from MRI do not reflect any directionality in the connectivity pattern of the edges.

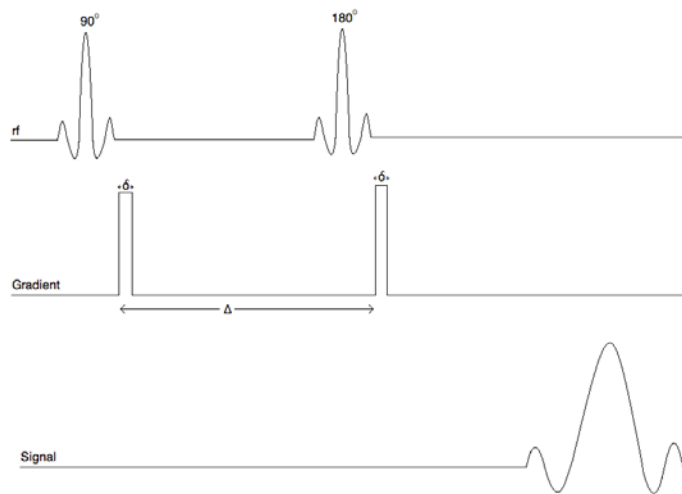


Figure 2-1. Stejskal Tanner diffusion sequence: Shown is a spin echo sequence with two short duration diffusion gradients applied after each radio frequency pulse. The radio frequency pulses will give rise to the measured magnetization. The time δ , is the duration of the diffusion gradient, and time Δ is the time between gradients. The diffusion gradient duration is set to be “short” so that the diffusion undergone by the spins in δ is negligible compared to Δ .

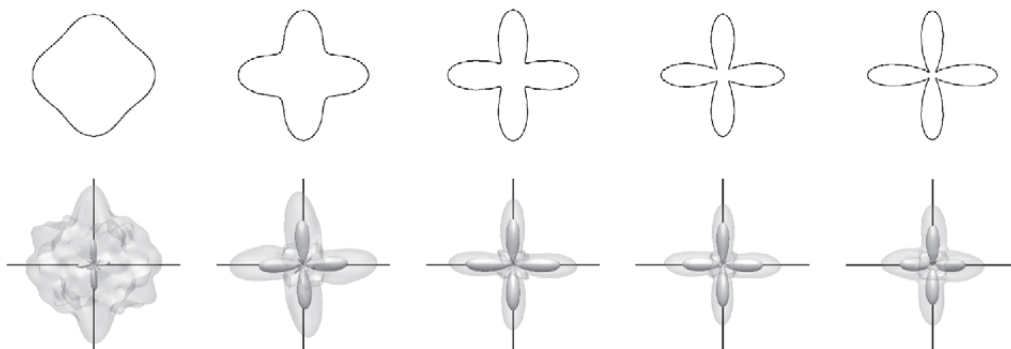


Figure 2-2. The effect of the b value on the estimation of the diffusion profile: Top: the noiseless signal attenuation profile in the plane of the fibers for a system consisting of two fiber populations crossing at 90° . Bottom: the corresponding fiber orientation distribution function for $\text{SNR} = 30$. The mean fiber ODF is depicted by the opaque surface, and the mean fiber standard deviation by the transparent surface. Left to right: b value increasing from 1000 to 5000 s/mm^2 in increments of 1000 s/mm^2 . Image from Tournier, et. Al. (Tournier et al., 2004). Reproduced with approval from Elsevier.

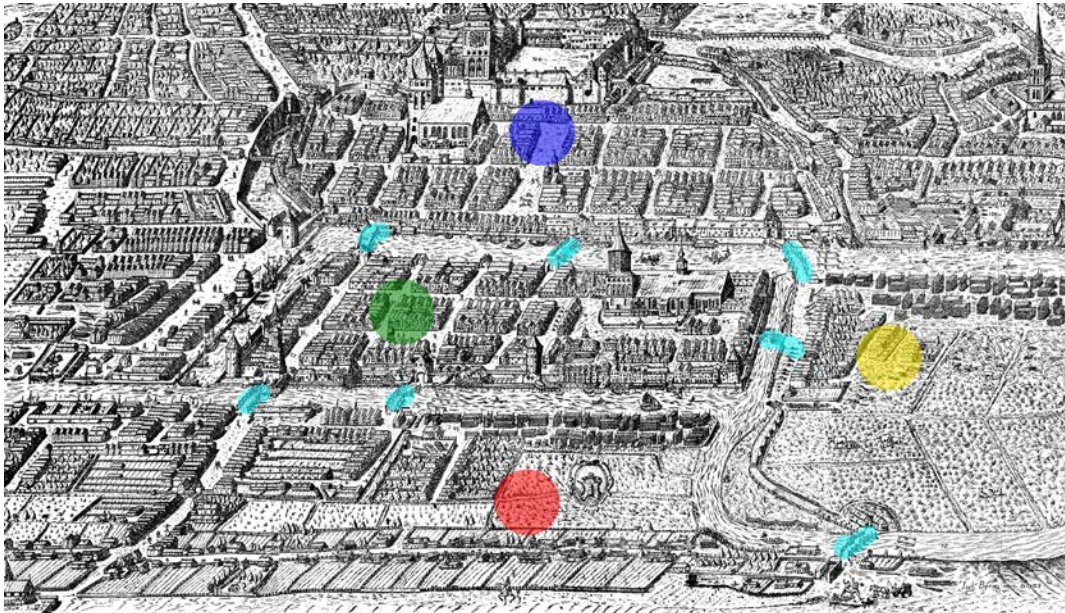


Figure 2-3. The Königsberg map: The islands are represented by the green and yellow dots and the large land masses are represented by the blue and red dots. Bridges are shown in turquoise. (Picture modified from engraving by Joachim Bering (Public domain, 1613))

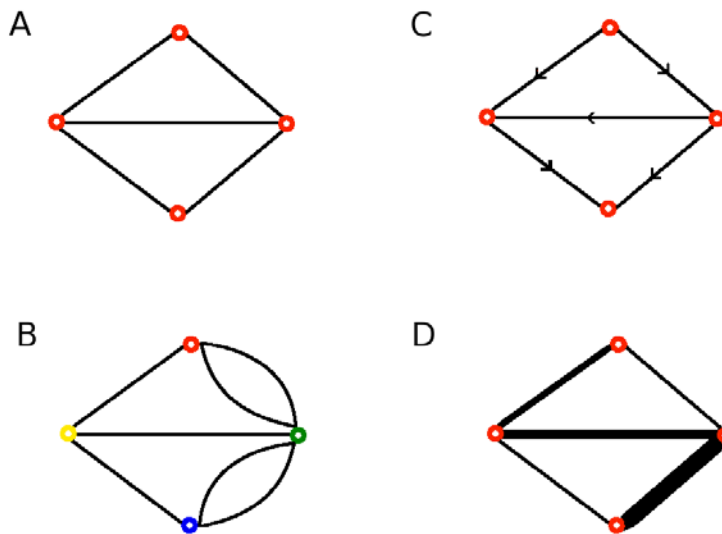


Figure 2-4. Types of Graphs: A) Displays a simple graph. B) Multigraph representing the city of Königsberg (Nodes' color corresponds to the nodes in Figure 2-3). C) Sketch of a directed graph, top node is a source and bottom node is a sink. D) Weighted graph, thicker edge represents largest edge weight value.

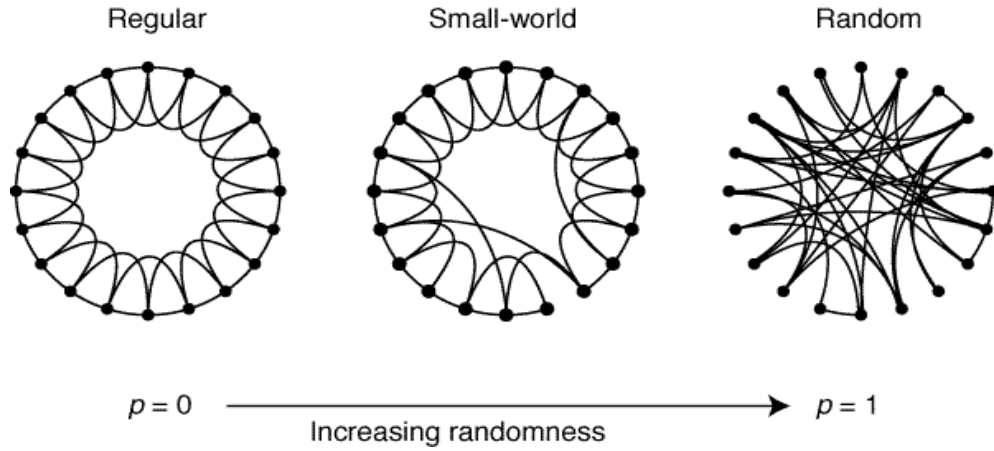


Figure 2-5. The small world phenomenon: Graphs arranged; regular, small world and random graphs. (Figure from Watts et al. (Watts and Strogatz, 1998)). Reproduced with approval from Nature Publishing Group.

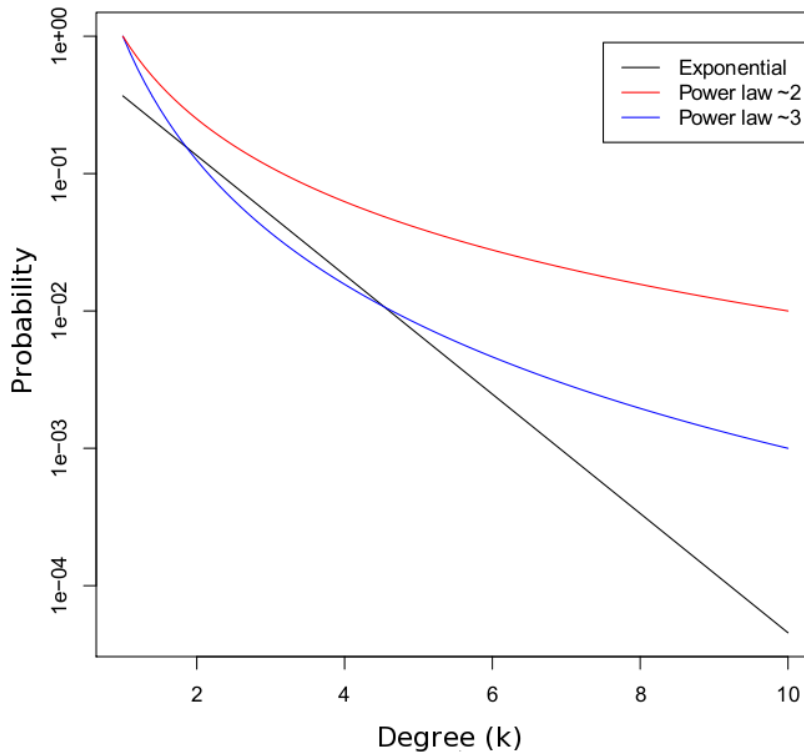


Figure 2-6. Scale free distributions in log-linear scale: Plot of the power law behavior in observed degree distributions from scale free networks. The exponential decay is associated with real, small world networks.

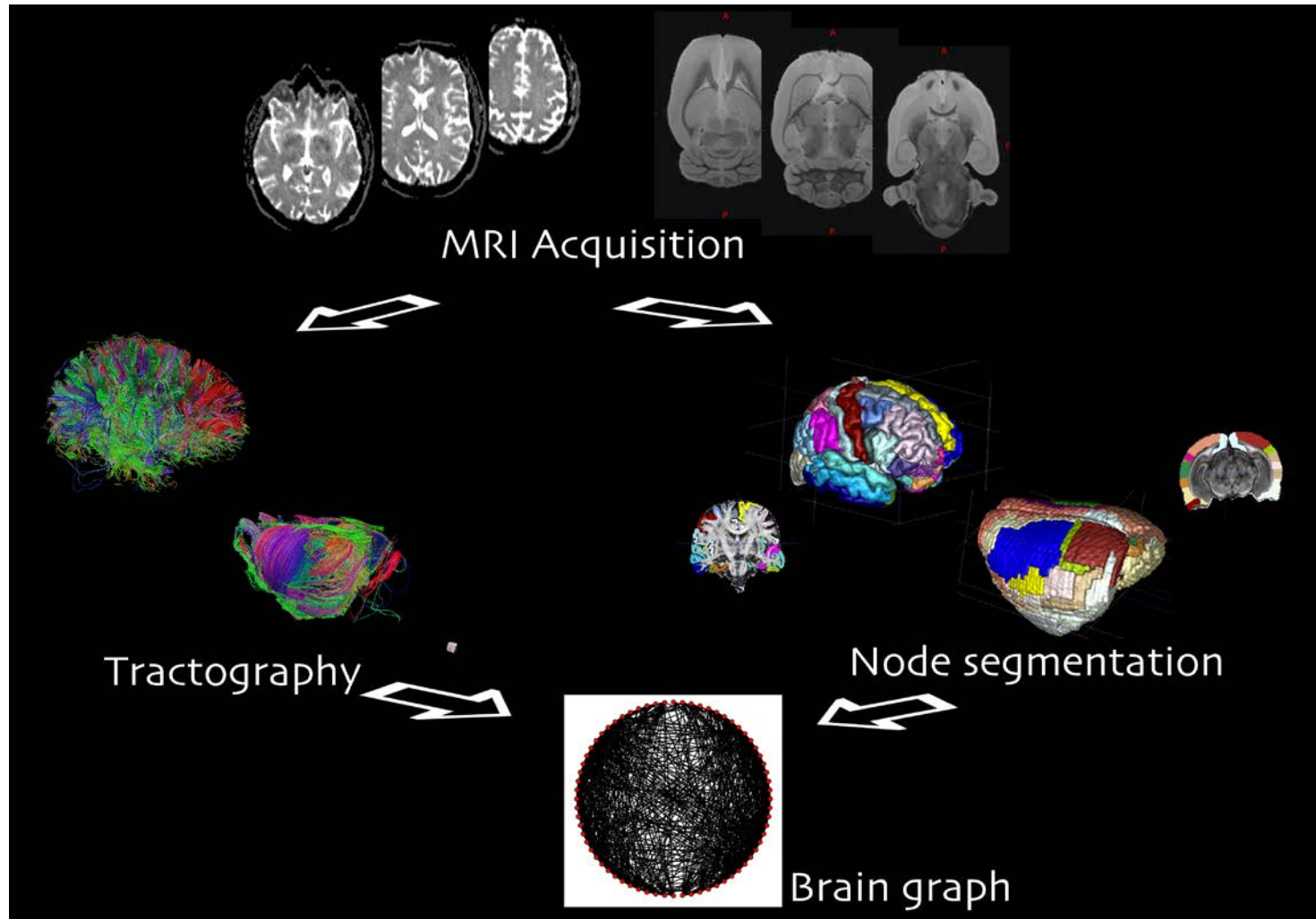


Figure 2-7. Brain graph construction. First a diffusion-weighted (DW) image is acquired. DW image allows the segmentation of the brain image into a set of nodes. In a separate step the DW image allows one to create a fiber map (fiber tracking explained in methods) to estimate the connections of the brain. Finally with the constructed network path length, clustering coefficient and parameters can be calculated.

CHAPTER 3 GENERAL METHODS

This chapter reviews the common techniques employed in the next three chapters of this dissertation. Firstly, the human and rat acquisition schemes are explained. Then the software and post processing techniques are reviewed. Lastly the tractography is reviewed and the software for the network calculation is presented.

3.1. MRI Acquisition

3.1.1. Human Data

The University of Florida Institutional Review Board approved all human studies. One healthy subject was scanned ten times throughout the course of one month, which provided a controlled set of ten brain networks to determine the network properties across different MR acquisitions. The subject was scanned in a 3T Siemens Verio system in the Shands Hospital of the University of Florida. HARDI data was obtained with a spin echo preparation and an EPI (Poustchi-Amin et al., 2001) readout and the following set of parameters: TR/TE = 17300/81 ms, 2 scans without diffusion weighting, 6 diffusion weightings with b-values (Equation 2-9) of 100 s/mm² and 64 diffusion weightings with b-values of 1000 s/mm² (Figure 3-1). The diffusion gradients were distributed following a scheme of electrostatic repulsion (Jones et al., 1999). The diffusion-weighted images covered the entire brain with an isotropic resolution of 2.0 mm, field of view (FOV) of 256 mm x 256 mm and 73 slices, which interpolated to 1.0 mm isotropic with tri-cubic interpolation. In addition, a high-resolution T1 structural scan of the entire brain was acquired with TR/TE = 2500/3.77 ms, resolution 1mm isotropic, FOV of 256 mm x 256 mm and 176 slices.

3.1.2. Animal Data

Four excised 90-day-old normal rat brains were scanned at the Advanced Magnetic Resonance Imaging and Spectroscopy (AMRIS) facility of the McKnight Brain Institute at the University of Florida with repeats of two brains for a total of six data sets. HARDI data was obtained using a 17.6 T Bruker Avance system (Bruker Corp, Billerica, MA) with the following set of parameters: 7 diffusion weightings with b values of 100 s/mm² and 64 diffusion weightings with b values of 2225 s/mm². The diffusion gradients were distributed following the scheme of electrostatic repulsion. An image resolution of 190 x 190 x 190 μm³ was acquired; therefore this data set will be referred to throughout this text as the 190 μm data set. Two new data sets were created for each of the six data sets by interpolating the original image to 95 x 95 x 95 μm³, referred to as the 95 μm data set, and degrading it to 380 x 380 x 380 μm³, referred to as the 380 μm data set, by using only half of the original k-space (Fourier transform of the MR image) information to reconstruct the image. Representative images of these data sets are shown in Figure 3-1.

3.2. Post Processing

The diffusion weighted scans were corrected for motion distortion using FSL's *eddy_correct* algorithm (Jenkinson et al., 2012). With the motion corrected data, FA and AD maps were created using in-house software using the Interactive Data Language (IDL; Exelis Visual Information Systems, Boulder, CO). The probability displacement function (PDF) was calculated on each voxel using a mixture of Wishart (MOW) distribution of positive definite matrices (Jian et al., 2007b) implemented with an in-house C based software. Using the root mean displacement in three dimension

($\chi^2 = 6Dt$, where $t = \Delta - \delta/3$), the PDF was estimated in each voxel for an average water displacement of 13 μm (human data) and 6 μm (rat data), then the maximum displacement probability within tissue in each voxel is identified and associated as the local fiber orientation. The nodes were created by visual inspection using ITKSNAP (Yushkevich et al., 2006) to delineate the desired structures on the FA and AD maps. For human data, the node segmentation was performed on a single data set (the first one acquired) at the 1 mm x 1 mm x 1 mm resolution data set, then registered to the other nine data sets using FSL's FLIRT and ApplyXFM (Jenkinson et al., 2012). Then these nodes were then registered onto the 2 mm x 2 mm x 2 mm data set from its correspondent 1 mm x 1 mm x 1 mm data set by applying an identity transformation using ApplyXFM. The node segmentation for the rat data was performed using the 95 μm resolution FA map. These nodes were then registered onto the 190 and 380 μm data sets by applying an identity transformation using ApplyXFM. Details of node placement will be addressed in each subsequent section.

3.3. Tractography

The fibrous structures of the brain are estimated from diffusion-weighted data by creating fiber maps using tractography. These are calculated by deterministic streamline tractography in the whole brain employing the MOW-derived fiber orientations.

Tractography was performed following a modified version of the fiber assignment by continuous tracking (FACT) algorithm (Mori et al., 1999), in which the direction with the least angular deviation along the incoming fiber path was selected to be continued at each iteration of the tractography process. In many brain regions WM fibers cross or kiss, so DTI cannot model the diffusional characteristics in these regions by just a single

Gaussian diffusion tensor per MR voxel, as explained in Chapter 2. Therefore MOW is used to estimate the multiple fiber orientations in each MR voxel, yielding a more accurate description of fiber directions. Fiber maps were calculated using an in-house C based software. To avoid the ambiguity of random placement of seed points, these were placed uniformly throughout the MR voxels making up the brain. Tractography is performed by seeding each MR voxel in the brain with any number P of evenly-spaced seed points. From each seed point, one streamline is launched bi-directionally for each estimated displacement probability maximum contained in that voxel with the modified FACT algorithm. Each streamline front is propagated by stepping half of the MR voxel width in the direction that is most in line with the streamline's present direction of travel (i.e. tractography generated smooth and no sharp turns) as shown in Figure 3-2.

Tractography parameters were: 125 seeds per voxel, a fiber step size of 0.5 of the voxel size, and no step-to-step track deviations greater than 50° and stopping criteria for voxels with low anisotropy values ($FA < 0.05$). If the estimated track exceeds this threshold, the streamline is stopped.

3.4. Network Calculations

All network metrics were calculated in R (<http://cran.us.r-project.org/>), with the aid of the network package (<http://cran.r-project.org/web/packages/network/index.html>).

The network package is a set of tools to create and modify network and relational data within the R interface. All the networks metrics described in Section 2 were calculated with in-house written software. All network metrics were calculated with the equations presented in this manuscript (Chapter 2 for binary metrics and Chapter 5 for weighted metrics). A copy of the most complicated of the codes can be found in Appendix C.

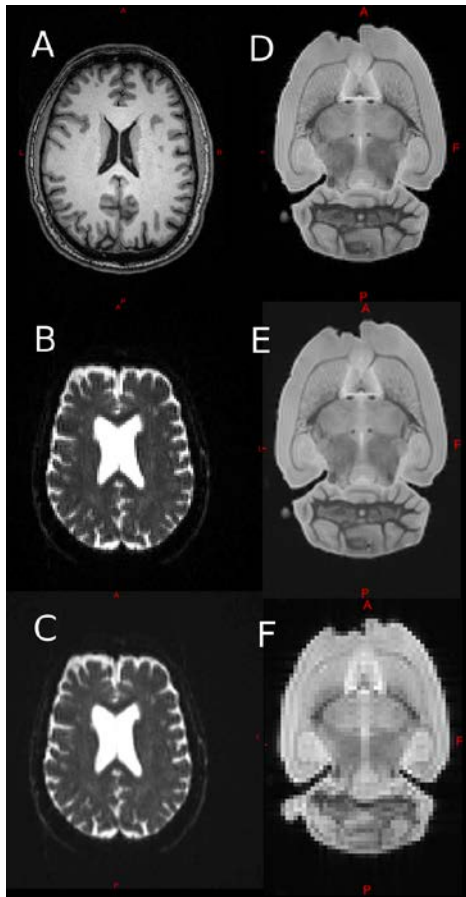


Figure 3-1. Images of data used. Human data shown in left column and rat data to the right. A) T1 weighted image at 1mm isotropic resolution. B) DW image at the acquired resolution of 2mm isotropic. C) Interpolated DW to 1 mm isotropic resolution. D) Acquired DWI at 190µm isotropic resolution. E) Interpolated DWI to 95µm isotropic resolution. F) Degraded DWI to 380µm isotropic resolution

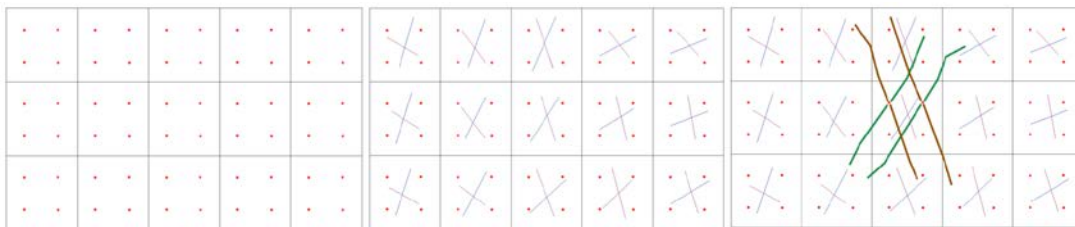


Figure 3-2. Diagram of the tractography process. The first image on the left shows the seed points that starts each fiber. Each point is evenly spaced in the entire brain. The middle figure displays the calculated fiber orientations. This image shows 2 fiber orientations in each voxel. The image in the right shows the fiber propagation across the entire image. Each seed point contributes with two fibers because there are two fiber orientations in each voxel, but once a streamline is started it will follow the direction most in line with its path.

CHAPTER 4 WEIGHTING BRAIN NETWORKS

4.1. Opening Remarks

Graph theory studies applied to brain networks have gathered a great deal of interest in large part due to the desire to analyze the large-scale cortical structure of the brain (Bassett et al., 2011a; Cheng et al., 2012a; Costa Lda et al., 2007; Gong et al., 2009; Hagmann et al., 2008; Hagmann et al., 2007; Romero-Garcia et al., 2012; Sporns et al., 2007). In addition to cortical analysis, graph theory has been applied to understand the relation between brain network structure and brain development (Hagmann et al., 2010b) or pathological states like: epilepsy (Ponten et al., 2009), schizophrenia (van den Heuvel et al., 2010), Alzheimer's (Lo et al., 2010), and multiple sclerosis (He et al., 2009). On the other hand, little attention has been devoted to studying subcortical networks (Colon-Perez et al., 2012), e.g. the limbic system in which abnormal connectivity is thought to be related to epilepsy (Bertram, 2009). Changes in the connectivity between structures of the limbic system, which includes the hippocampus (HC), amygdala (AM), thalamus (TH) and entorhinal cortex (EC) is theorized to be the source of the emergence of epilepsy (Nadler, 2003). In other words, epileptic networks may have a different connectivity structure when compared to normal networks. Studying the connectivity of limbic structures using graph theory, instead of cortical analysis, would aid in understanding epileptogenesis and possibly, when employing the appropriate anatomical regions, other types of pathologies.

To quantify brain connectivity, an edge weight is proposed that is an extension of a previously defined edge weight (Hagmann et al., 2008). This new edge weight will provide a measure independent of network scales, spatial resolution, and tractography

parameters, as long as sufficient and reliable diffusion information is acquired during the magnetic resonance experiment. What constitutes “sufficient” resolution is an open question in tractography; however, for the purposes of this work if the fiber size is in order of the MR voxel size, then this would represent a minimum condition for sufficient information from the MR (under the condition that sufficient SNR and an adequate DWI experiment is obtained). If the fiber is much smaller than the MR voxel resolution, then this does not constitute sufficient MR resolution. Important to note is the brain is a very complicated system and all anatomical fibers are not well known; hence, in this work by the feasibility of streamlines obtained from tractography is related to the expected fiber pathways that usually form in the brain. The edge weight metric can be used to analyze WM connectivity between GM structures. As is common in all imaging techniques, the limitations to the application of the edge weight arise from spatial resolution to estimate fiber pathways. With DWI, the metric is also limited by the angular resolution of the diffusion measurement. When tracts are too small compared to the spatial resolution, volume averaging starts to dominate. Also, if the angular resolution of the diffusion measurement is not sufficient to characterize the diffusion profiles, the tracts obtained from tractography might not represent the WM structure of the brain. Therefore, noise and resolution (spatial and angular) limitations will play a more important role, as the fiber tracts get smaller.

4.2. Methods

4.2.1. Edge Weight

Using graph theory and tractography, WM fibers connecting anatomical GM brain structures can be represented as edges connecting nodes. The connections derived

from tractography are estimated by calculating streamline-fibers which are an estimation of the actual WM fibers in the brain. To distinguish real from calculated fibers in this dissertation, fibers created from tractography from now on will be referred to as streamlines and the actual WM fibers in the brain will be referred to as fibers. The path of fibers is estimated with tractography as streamlines which are started from seeds that represent the spatial location used to initiate the streamline calculation. The total number of streamlines originates from two sources: the number of seeds per voxel and the number of voxels that make up the streamline. To determine the strength of an edge, a modification of a previously defined edge weight (Hagmann et al., 2007) was made to create a dimensionless, scale invariant measure of connectivity. The modification consists of removing dependencies on fiber scale and tractography seeding schemes (these points will be reviewed shortly) via normalization of the edge weight by the ratio of the MR voxel volume and the number of seeds per voxel, as shown in Equation 4-1.

$$w(e_{ij}) = \left(\frac{V_{voxel}}{P_{voxel}} \right) \left(\frac{2}{A_i + A_j} \right) \sum_{p=1}^P \sum_{m=1}^M \frac{1}{l(f_{p,m})} \quad (4-1)$$

where V_{voxel} is the MR voxel volume, P_{voxel} is the number of seed points per voxel, A is the surface area of each node, M is the number of voxels making up the edge, and $l(f_{p,m})$ is the length of the streamline originating from seed point p on voxel m . The edge weight (Equation 4-1) presents a tight relationship between V_{voxel} and the total number of streamlines (obtained from tractography). For a system with a fixed surface area and fiber length, when V_{voxel} is reduced by some factor then the summation over M increases by the same factor, leaving the edge weight unchanged in spite of changes in

spatial resolution. For example, a fiber characterized by a single voxel, as the spatial resolution is increased by a factor of 2 on each dimension then V_{voxel} will be reduced by 2^3 and the summation over M will now have eight voxels characterizing the fiber. In other words, the reduction by eight in the V_{voxel} is made up with an increase by eight of the total number of streamlines. This relationship between V_{voxel} and M allows the edge weight to be a measure of connectivity strength not dependent on resolution (as long as sufficient information is obtained to characterize the fiber). It will be shown shortly that inadequate spatial resolution is a problem to estimate the small fibrous structure. For the interested reader an analytical description of the edge weight is presented in Appendix B. The current discussion, using the numerical calculation described here, will be more suited to the connectivity measured with tractography.

A 2D example on how to calculate the edge weight is described to show the edge weight's independence of fiber scale and tractography seeding schemes. This shift to a 2D case will be made for simplicity of this introductory description. The edge weight (Equation 4-1) has to be modified for this 2D example; therefore, V_{voxel} becomes a pixel area, A_{pixel} , and A becomes a node perimeter. A depiction of a two-dimensional edge weight is illustrated in Figure 4-1, where each node represents a single pixel. The resolution of the pixels in Figure 4-1 is d , the area of each pixel is d^2 and the perimeter of each node (gray boxes) is $4d$. Figure 4-1a shows an example where the seeds per pixel is one, $P_{\text{pixel}} = 1$, producing only one streamline connecting the nodes with a fiber length of d , resulting in an edge weight value of $1/4$. In Figure 4-1b, the seeds per pixel value is changed to four, resulting in four streamlines; however, the edge weight normalization factor ($Area_{\text{pixel}} / P_{\text{pixel}}$) will account for this difference, yielding an edge

weight value of 1/4. This result is consistent for any number of seeds per pixel for the edge of Figures 4-1a and 4-1b. In Figure 4-1c, the streamlines connecting two nodes do not lie within a single pixel, but within two pixels and with one seed per pixel, $P_{pixel} = 1$. In this case, the streamline length would be $2d$ but, since all the pixels in the streamline path are seeded, a total of two streamlines would connect the nodes. Therefore, the result of Equation 4-1 is still 1/4. For straight 2D streamlines directly connected between identical nodes through a face (as in Figure 4-1), the edge weight value is 1/4. This result is independent of the number of pixels that make up the streamline and the number of seeds per pixel.

The connectivity strength (Barrat et al., 2004) of any node in a weighted graph can be defined by

$$s(n_i) = \sum_{i \neq j} w(e_{ij}). \quad (4-2)$$

In this equation, $w(e_{ij})$ is the edge weight (Equation 4-1) connecting node i to another node, j . A node that is fully connected with straight streamlines (Figure 4-2) shows a dark, central node connected to four other nodes, where each streamline is a replica of the example shown in Figure 4-1a. The central node has a connectivity strength value of 1, which represents a fully connected node, since there are 4 edges, each with an edge weight of 1/4.

The same straight 2D fiber, as the one just described, will now be considered in 3D space. The surface area of the connected nodes will now become, $A=6d^2$. Identical single voxel nodes separated by one voxel, leaves one voxel to characterize the fiber connecting them. Similarly as the 2D discussion, for any number P of seed points, the number of streamlines will be determined by P since only one voxel will contribute to the

fiber estimation. Finally the 3D fiber will have an edge weight value $1/6$ since the obtained number of streamlines will be normalized by the number of seed points in Equation 4-1. If the separation of the nodes is increased and the fiber is contained within M voxels, the number of streamlines will now be $M*P$ and the fiber length will turn out to be $l=M*d$. In this case the edge weight value will still be $1/6$ for any number of seed points and any fiber length as long as the nodes are identical. Lastly, if the nodes are not single voxels as discussed so far, the surface area of the nodes will be related to number of voxels in each spatial dimension. Nodes of rectangular shape with “u” number of voxels in one dimension, “v” in another, and “w” in the remaining dimension will now be considered. The surface area of these nodes becomes the sum of the number of voxels in each of its six rectangular faces (from now on the “uv” face refers to the region of the node with surface area uvd^2 and so on for the other dimensions). The average surface area of these nodes is, $A=2uvd^2+2uwd^2+2vwd^2$. For any number of voxels separating the connected nodes and any number of seed points the number of streamlines in the face with cross section “uv” becomes $u*v*M*P$ and the length will be, $l=M*d$. The edge weight is then given by

$$\begin{aligned}
 w(e_{uv}) &= \frac{d^3}{P} \frac{1}{(2uv + 2vw + 2uw)d^2} \sum_{p=1}^P \sum_{m=1}^{uvM} \frac{1}{l} \\
 &= \frac{d^3}{P} \frac{1}{(2uv + 2vw + 2uw)d^2} \frac{uvMP}{Md} = \frac{uv}{2(uv + vw + uw)}.
 \end{aligned} \tag{4-3}$$

The numerator in Equation 4-3 is modified conditional to the face where the fiber is connecting the nodes. For example, if the fiber connects through the “vw” face the numerator gets modified to vw and so on. The result of Equation 4-3 can be used to estimate the node strength of a rectangular node connected to identical nodes. If the

node is connected to 6 fibers through each one of its faces (i.e. through “uv”, “vw”, and “uw”) the resulting node strength turns out to be

$$s(n) = 2w(e_{uv}) + 2w(e_{vw}) + 2w(e_{uw}) = 2(uv + vw + uw) \left(\frac{1}{2(uv + vw + uw)} \right) = 1. \quad (4-4)$$

The node strength again is one for a fully connected node by a single edge through each of its six faces. In this case the fibers can have different sizes and changing the number of seed points per voxel, and length of fiber will not affect this result. As a special case of rectangular nodes, let's consider disks (i.e. $w = 1$). The surface area of disks become, $A=2uvd^2+2ud^2+2vd^2$. The fiber length will again be of arbitrary length, $l=M*d$. The edge weight is given by

$$w(e) = \frac{uv}{2(uv + v + u)} = \frac{1}{2 \left(1 + \frac{1}{u} + \frac{1}{v} \right)}. \quad (4-5)$$

As u and v become large then $w(e)$ tends to $1/2$ and as $u=v=1$, then w tends to $1/6$ as shown before. In summary, the edge weight is a measure of the strength of connectivity between two nodes in a network. It is defined as being inversely proportional to the surface area of the connected nodes, providing a measure of the overall connectivity between two nodes relative to the surface area available to create connections.

Therefore, node surface area and streamline coherence are the main sources of variation in the measured edge weight.

4.2.2. Edge Weight Derived from DWI

The proposed edge weight in the previous section is defined by calculating streamlines only from “WM voxels” (i.e., streamlines that do not originate from nodes or

outside the streamline path). This assumption relies on an appropriate WM and GM differentiation in order to only seed voxels representative of WM tracts or “WM voxels”. Selecting WM voxels would introduce *a priori* selection that determines the boundaries of WM and GM. Preferably no *a priori* assumptions should be made in the seeding scheme; hence, the tractography is performed on each voxel with homogenous and evenly spaced seed points within the entire brain. This tractography procedure will yield a large number of streamlines from multiple tissue sources: the WM track, the anatomical nodes and external track regions. This seeding scheme requires a method to retain only streamlines originating from the desired WM tract.

Streamline filtering is performed to remove streamlines that originate from the nodes and external voxels that do not constitute the WM path connecting the nodes. Only streamlines originating in the WM regions (light gray in Figure 4-3a) and connecting the nodes (dark gray in Figure 4-3a) are used in the calculation of the edge weight and all other streamlines are discarded. Connected nodes will yield a set of M voxels (light gray in Figure 4-3b) that define the edge (dark gray in Figure 4-3b). In the set of all streamlines within the set of M voxels, only the streamlines that meet the following criteria are retained:

1. Directly connect the nodes (i.e. no additional nodes are found in the streamline path)
2. Originate from seed points in the set of M voxels.

These criteria define a subset of seed points, R , within the set of all seed points, $M*P$, located at positions x_R, y_R, z_R (Figure 4-3b) in the M voxels used to calculate edge weight.

To fit the criteria mentioned above, the edge weight defined in Equation 4-1 is modified as,

$$w(e_{ij}) = \left(\frac{V_{\text{voxel}}}{P_{\text{voxel}}} \right) \left(\frac{2}{A_i + A_j} \right) \sum_{p=1}^P \sum_{m=1}^M \frac{\chi_R(f_{p,m})}{l(f_{p,m})}. \quad (4-6)$$

where

$$\chi_R(f_{p,m}) = \begin{cases} 1, & f_{p,m} \in R \\ 0, & f_{p,m} \notin R \end{cases} \quad (4-7)$$

Equation 4-6 introduces $\chi_R(f_{p,m})$, which is the characteristic function for the set R of streamlines connecting nodes n_i and n_j . The characteristic function (Equation 4-7) ensures that the streamlines connecting any two nodes are sampling the spatial location of the fiber and eliminate spurious streamlines that do not meet the criteria described in this section.

4.2.3. Simulations

A simulation was executed on IDL (Exelisvis, Boulder, CO) to determine the effect of increasing seeds per voxels in more complicated pathways than the fiber pathway previously described in Sections 4.2.2 and 4.2.1. The simulation was performed using single voxels as nodes that connect through an arched fiber (Figure 4-4a), a slanted fiber at 45° within the plane (Figure 4-4b), and a slanted fiber at polar angles of $\theta=45^\circ$ and $\varphi=54.1^\circ$ (Figure 4-5). The space between the nodes' closest points was varied from 1 (Figures 4-4a to 4-4b and 4-5), 2 and 3 voxels, and the seeds per voxels were varied in linear increments of 1^3 to 100^3 seeds per voxel. The seeds were placed uniformly in each voxel and the distance from the seed point to each node

was calculated. If the seed point was a member of subset R , it was used to measure the edge weight; otherwise, it was discarded.

To estimate the impact of random errors (like the influence of noise on calculated diffusion directions, improper diffusion gradients sampling and anisotropic voxels) on the edge weight, a simulation was performed of the slanted fiber at 45° within the plane (Figure 4-4b). The fiber will have vector components, $v = [0.707, 0.707, 0.0]$, in an $\{x, y, z\}$ coordinate system. An image containing v in each voxel was defined *a priori* and used for tractography. The image containing v was modified to obtain five images at different noise levels by adding a standard deviation (σ) to each voxel. The added random errors (Gaussian distributed, which resembles the effect of noise on calculated diffusion directions) were: 0 (no error), 0.03, 0.07, 0.1 and 0.2. The tractography was performed 105 times with varied random errors restrained to the standard deviations previously described, 125 seeds per voxel and a 0.5 step of the voxel size. The separation of nodes through the nodes' closest points was varied from 1, 2, 3, 5 and 10 voxels.

4.2.4. Node Segmentation

The edge weight calculation depends on reliable node segmentation, since the surface area estimation is used in Equation 4-3; hence, accurate node delineation is crucial to reliably estimate node connectivity. Careful and consistent segmentation reduces the underestimation of the WM tracts (Figure 4-6b) and the incorrect assignment of WM tracts (Figure 4-6c). Although the edge weight presented here is independent of fiber scale and seeding scheme, the segmentation of the nodes is a crucial part to define the connectivity in the brain. The nodes are segmented by defining

voxels, which meet the criteria of spatial location and contrast (will be described in each chapter as necessary) of the desired anatomical regions. The spatial resolution (i.e. voxel size) affects the edge weight measure as a result of volume averaging and ambiguity in the selection of the node boundaries. The next two paragraphs will describe the criteria used to segment the nodes which are used to define the human and rat brain networks used in this chapter.

A simple network in the human brain of two nodes was first used to check the edge weight variation across different acquisitions. The nodes were placed at the edges of the cingulum and corpus callosum (CC), which are large and coherent WM paths. Using an FA map, disk nodes were placed within the cingulum to create the two-node network, as shown in Figure 4-7a and 4-7c. To define the cingulum edge, disk nodes were separated by roughly 49 mm to create the long edge of the cingulum, as shown in Figure 4-7c. Placing a third node in the middle of the cingulum tract created a three-node network, resulting in two edges of roughly 24 mm of length each (i.e., cingulum short edges). The radii of all the cingulum node disks were about 7 mm. To study the edge weight values of the CC, disk nodes were also placed laterally at each side of the body of the CC at the point where it starts to branch outward into the cortex (roughly 22 mm apart) as shown in Figure 4-7b and 4-7d. This edge will be referred to as the long edge of the CC as shown in Figure 4-7d. A second three-node network is made by placing a third node at the midline of the body of the CC, creating two edges of about 10-11 mm each (i.e., CC short edges). The radii of the corpus callosum node disks were each about 6 mm.

The rat brain networks were segmented by visual inspection from the defined structures in the Paxinos and Watson Rat Brain Atlas (Paxinos and Watson, 1998). The rat brain networks consisted of the limbic system (LS) structures of four excised rat brains. A coronal view of the structures is shown in Figure 4-7i, where the thalamus (TH) is the blue node, amygdala (AM) is green, entorhinal cortex (EC) is yellow and hippocampus (HC) is red; the color scheme is maintained in Figures 4-7e to 4-7i. To obtain a first estimation of the boundaries of the rat brains' LS nodes, the four nodes were segmented using FA maps in ITKSNAP from coronal slices following Paxinos guidelines. Further refinement was performed in the sagittal and transverse slices to achieve a 3D representation of the nodes without sharp peaks or hollow spots. In segmenting the TH, the acoustic radiation, the fasciculus retroflexus, and the medial lemniscus were used as boundary markers. The HC included the CA1, CA2, CA3 and dentate gyrus. The alveus of the HC, the fimbria of the HC and the laterodorsal thalamic nucleus were not included. The AM structure did not include the optic tract and kept a clear boundary between the amygdala and the piriform cortex. The EC was defined without including the dorsal endopiriform nucleus and the piriform cortex below the structure (in reference to the coronal slice). A space above the EC (~ 2 or 3 voxels) was left to separate it from the perirhinal cortex (in reference to the coronal slice). The entorhinal cortex becomes larger as it goes from anterior to posterior in the coronal slices. The subiculum was not included to physically maintain a separation between the EC and HC.

4.3. Results

Brain fibers do not necessarily traverse a straight path perpendicular to the surfaces of the nodes, like the example of Figure 4-1; therefore, additional analysis was

performed to address the edge weight expectation on more complicated pathways similar to those in Figures 4-4 and 4-5. Seed density effects (i.e., seed point locations) in complicated pathways strongly influence the selection of the streamlines that are used for the edge weight calculation. An example of voxel edge effects is shown in Figure 4-8, where not all seed points from the set of M pixels contribute to the edge weight. Figure 4-8a shows 5 voxels, for a total of 20 possible seed points, contributing to the edge weight. Out of the 20 possible seed points, only 8 will eventually contribute to the edge weight, as shown in Figure 4-8b. Consequently, the discrete square geometry of voxels in MR images will affect the outcome of the calculated edge weight as a result of seed point placement. This chapter discusses the application and results of the edge weight to human and rat brain networks. With the human data the edge weight is calculated for large and coherent WM tracts in repeated MR acquisitions of the same subject. With the rat data an assessment of the changes of resolution and interpolation are addressed.

4.3.1. Simulations

Initially, simulations were performed to study the seed density effects on calculated edge weights in ideal situations without noise contributions to the estimated primary diffusion direction. This resulted in no deviations in the fiber path as the length increases. Seed density effects are minimized as the seeds per voxel are increased, as Figure 4-9 shows. Increasing the seed points per voxel essentially samples region R (Figure 4-3c) homogeneously, allowing the edge weight to reach a horizontal asymptote for large numbers of seeds per voxel. Simulations for the arched fiber (Figure 4-4a) show the asymptotic behavior of the edge weight as seed points are increased, as

shown Figure 4-9a. The plot in Figure 4-9a reaches a plateau at high number of seed points per voxel reaching asymptotic values of 0.167, 0.166, and 0.165 when the separation between nodes is 1, 2, and 3 voxels, respectively. As the fiber length increases (larger node separations) the edge weight displayed larger differences from plateau values at small number of seed points. Differences from the plateau edge weight were found to be less than 1.01 % for 1 voxel of separation with at least 64 seeds per voxel, 2.48% for 2 voxels of separation with at least 125 seeds per voxel, and 9.57% for 3 voxels of separation with at least 125 seeds per voxel (Figure 4-9a). These results suggest that longer fibers require a larger number of seed points to achieve stable edge weight results.

Edge weight results for the slanted fiber (Figure 4-4b) are shown in Figure 4-9b. The plot of Figure 4-9b reaches a plateau with values of 0.234, 0.233, and 0.233 when the nodes' separation through the nodes' closest points contains one voxel, two voxels and three voxels, respectively. Differences from the plateau edge weight were found to be less than 6.49% for one voxel separation when the seed points were at least 216, less than 7.89% for two voxels of separation when the seed points were at least 216, and less than 6.40% for three voxels of separation when the seed points were at least 216. A 10% difference from the plateau value was reached at 125 seeds per voxel (Figure 4-9b). Similarly as the arched fiber, these results suggest that larger number of seed points is required to achieve stable measures of connectivity. In this slanted simulation the fiber connects the nodes though two faces of the nodes hence the edge is covering a larger surface area of the nodes. Appendix B shows an analytical calculation of this fiber edge weight, which agrees with the obtained results of ~ 0.234 .

Edge weight results for the three-dimensional slanted fiber (Figure 4-5) are shown on Figure 4-9c. The plot of Figure 4-9c reaches plateau values of 0.284, 0.282, and 0.281 when the separation of the nodes, through the nodes' closest points, contains one voxel, two voxels and three voxels, respectively (Refer to Appendix B for an analytical solution of this fiber's edge weight). Differences from the plateau edge weight were found to be less than 8.50% for one voxel separation when there were 729 or more seed points, less than 9.52% for two voxels of separation when the seed points were 729 or more, and less than 8.37 % for three voxels of separation when the seed points were 729 or more. A 20% difference from the plateau value was reached at 125 seeds per voxel (Figure 4-9c). As the first two simulations imply, a larger number of seed points yields a stable measure. As the geometry of the fiber path becomes more complex the number of seed points has to increase to accurately measure the edge weight on complex pathways.

In all simulated fibers, a large number of seeds per voxel ($P > 8000$) resulted in a less than 3% difference between the plateau values for each case. In these cases, placing 125 seed points per voxel yielded a 20% difference or less from the plateau. Consequently, the analysis was limited to $P = 125$, because increasing the number of seeds per voxel dramatically increases computation time and storage capacity. An entire brain tractography file with $P = 125$ yielded a file size for human data of ~ 250 GB and rat data ~ 500 GB. The larger file size of the tractography in the rat data is due to the high spatial resolution obtained in these data sets. The results suggest that $P = 125$ is a reasonable compromise between storage capacity and high seed densities. Cheng et al. suggest that high seed densities reduce variation in calculated brain network

parameters, similar to the results presented here. However, the highest seed density employed in their work was $P = 40$ (Cheng et al., 2012b). The discussed results suggest that for the edge weight (Equation 4-3) 40 seed points is not enough. Obtaining track files with more than 40 seed points becomes very time consuming and requires a large data storage capacity. Their limit of 40 seed points is justifiable to avoid large data files associated with larger number of seed points and shorter waiting time periods to finish the tractography.

The edge weight was calculated for single nodes connected by slanted fibers with increasing σ to simulate the effects of errors obtained in the estimated diffusion directions due to noise and having a finite number of gradient directions in the DWI measurement. The edge weight value with no error ($\sigma = 0$) was around 0.16 and 0.17 for all three separations, as shown in Figure 4-10. The coefficient of variation ($c_v = \text{standard deviation} / \text{mean}$) was 0.33%, to 0.4% at all separations. As the error is increased ($\sigma \leq 0.07$), the coefficient of variation increased (Figure 4-11), but remained less than 23% for all separations. As the σ reached 0.2, the c_v was 42.9% at 1 voxel of separation up to 162.9% for 10 voxels. Since the edge weight obtained from the simulation without noise is 0.17, an edge weight comparison can be made calculating the percentage difference between results with and without noise. The percentage difference for $\sigma \leq 0.03$ was never more than 11.9%, but as the σ reached 0.2 the percentage difference was 48.1% for 1 voxel of separation up to 95.9% for 10 voxels of separation. Since the edge weight is derived from tractography which in turn is derived from DWI measurements, appropriate levels of SNR are needed to estimate connectivity. In a separate work, Bastin et. al. showed that the SNR needed to obtain

stable tensor measures from DWI is 20 or more (Bastin et al., 1998). The results obtained from $\sigma=0.2$ would correspond to an SNR of 5, which is lower than the acceptable levels, hence it produces the large variations in the edge weight measures. The SNR of $\sigma=0.03$ would correspond to a value of ~ 33 which surpasses the minimum optimal SNR level to obtain stable measures from DWI. The results presented in this Section suggest that levels below $\sigma = 0.03$ levels yield differences of the edge weight values less than 7.5% from the plateau. In other words, high SNR measurements are needed to obtain stable diffusion measures which in turn lead to stable edge weights.

At this point, an emphasis is made that $P_{\text{voxel}} = 125$ will be maintained at all spatial resolutions for the human and rat data, which is suggested to be a reasonable compromise between file size and reduced variation of edge weight values. The edge weight presented here is normalized to remove any dependence on fiber scale and seeds per voxel; therefore, changes in seed density per unit volume should not significantly affect the edge weight results. A high spatial resolution implies higher definition of the WM fibers; hence, small pathways become more visible, which requires high seed densities to reliably represent these using tractography. At low spatial resolution, the small pathways will not be resolved with tractography even at extremely high seed densities due to volume averaging with larger pathways and other tissue architecture. Tractography in low spatial resolution data yields fewer streamlines per unit volume at constant P_{voxel} . The simulations described in this chapter suggest that performing tractography with a large number of seeds per voxel reduces the variation of edge weight measures of the fiber within the voxel. Increasing P_{voxel} at low spatial resolutions (compared to a high resolution data set), to maintain a constant seeds per

unit volume will only result in replicating the streamlines that are estimated at $P_{voxel} = 125$. Increasing the number of seeds ($P_{voxel} > 125$) will improve the results presented here; however, it creates extremely large tractography files and long waiting periods. Ultimately, the ability to reliably resolve small fibers will be dictated by the spatial resolution and keeping a high number of seed points in a voxel.

4.3.2. Cingulum and Corpus Callosum Networks

The edge weight connectivity of ten data sets from a single human subject was analyzed with disk nodes placed on the cingulum and CC tracts. These tracts were chosen because they are large, coherent, and fairly homogenous WM structures. The multi-scan single subject acquisition provides a good standard to assess the edge weight variation across image acquisitions of large tracks.

The CC edge weight results across all ten data sets at 1 mm isotropic resolution and seed density of 125 seeds per voxel are shown in Figure 4-12a. Average edge weight values are shown in Table 4-1 and Table 4-2 at 1 mm and 2 mm isotropic resolution, respectively. A consideration to have in this section is that the change in resolution is due to interpolation and not different acquisitions. Increased spatial resolution acquisition would yield lower SNR's which in turn affect the estimated diffusion parameters. In the current study SNR was constant, so the results to be discussed are due to interpolation and not to changes in SNR or acquisition parameters. Even though interpolation does not provide any additional information it will be shown that it does improve the fiber tracking calculation and the edge weight results. From now on it should be clear to the reader that for the human data the change in resolution is due to interpolation. Table 4-1 shows the long CC edge for the 1mm resolution data with

an average edge weight of 0.133 with c_v of 7.57% while the two shorter edges show an average edge weight of 0.156 and 0.179 with a c_v of 9.29% and 8.54%, respectively. The same analysis on the data set with an isotropic resolution of 2 mm (i.e., lower resolution) yielded an average edge weight of 0.096 with a c_v of 11.1%, and the two shorter edges yielded an average edge weight of 0.116 and 0.133 with a c_v of 9.55% and 9.88%, respectively. A comparison was made between the restrictive filtering of streamlines that originated from voxels outside of region R and the common procedure where no restriction is placed upon the streamlines that contribute to edge weights (i.e., allowing streamlines that connect the nodes to contribute to the edge weight independently of their spatial origin). The average CC edge weights results are shown in Tables 4-1 and 4-2. The 1 mm isotropic data results were: 0.94 for the long edge with a c_v of 10.4%, and 2.26 and 2.77 for the shorter edges with a c_v of 13.1% and 9.05%, respectively. The 2 mm data yielded average edge weights of 0.606 for the long edge with a c_v of 15.2%, and 1.62 and 1.95 for the shorter edges with a c_v of 15.0% and 13.3%, respectively.

The percentage difference between edge weights of longer edges compared to those of shorter edges was calculated to observe discrepancies in the edge weight as a result of node placement. The edge weight is a measure of connectivity strength; therefore, the average edge weight of the longer and shorter edges should only contain variation due to the seed point effects, as long as the streamline is completely contained within the nodes. The proposed method showed a difference from long to short CC edges in the 1 mm data of 16.1% and 30.0%, and the 2 mm data showed 18.7% and 32.2% difference. After allowing all streamlines to be used to calculate the edge weight,

the percentage difference in edge weight of the long to short edges was found to be 82.2% and 98.7% for the 1 mm data sets and 91.4% and 105.1% for the for the 2 mm data sets.

The same analysis was performed on the cingulum tract with the 1 mm data. It was found that the long edge weight average was 0.0612 with a c_v of 9.52%, and the two shorter edges showed an average edge weight of 0.0887 and 0.0766 with a c_v of 7.80% and 7.74%, respectively. In the 2 mm data sets, it was found that the long edge average edge weight was 0.0431 with a c_v of 12.5%, and the two shorter edges showed an average edge weight of 0.0575 and 0.0626 with a c_v of 10.7% and 8.15%, respectively. The percentage difference in edge weight from the longer and shorter edges was found to be 22.3% and 36.7% in the 1 mm data, and 28.7% and 37.0% in the 2 mm data. Without restriction to calculate the edge weight, the percentage difference in edge weight of the longer edge to the shorter ones was found the be 75.2% and 93.2% for the 1 mm data and 81.4% and 92.0% for the 2 mm data.

These results suggest that for large and coherent WM tracks the restrictive method used in this dissertation to define the streamlines that make up the edge reduces variation encountered due to volume averaging. Also interpolation helps reduce the effects of volume averaging seen in the reduction of the edge weights variations. The filtering of streamlines described in Section 4.2.2 ensures that only streamlines originating from the pathway are used in the connectivity estimation. The filtering eliminates the possibility of having streamlines that originate from extraneous regions contributing to the edge weight calculation. Also, as long as the path is contained within the voxels used to measure the connectivity, the restrictive method yields a more stable

measure than allowing all streamlines connecting the nodes to contribute to the edge weight.

4.3.3. Limbic System Network

The rat LS network at different spatial resolutions is shown in Figures 4-7e to 4-7g. It is evident from a visual inspection of the streamlines that the spatial resolution will affect network measures as a result of volume averaging effects. In this case the changes in resolution are due to interpolation (similar to human data) but also due to the process described Chapter 3, where only half of the k-space is used to reconstruct the image which would equate to a low resolution acquisition. The acquired data (190 μm) set took 20 hours to acquire and the acquisition parameters were agreed upon as a compromise between acquisition time and optimization of the DWI parameters. In this dissertation interpolation is used as a means to obtain “higher” spatial resolution data without undergoing multiple days of acquisition of a 95 μm spatial resolution data set. It should be clear now that changes in spatial resolution in the rat data are obtained by interpolation and k-space restriction in the reconstruction of the data (Chapter 3).

The LS network displays a set of long streamlines wrapping around the HC (red node) in the higher spatial resolution data set as shown in Figure 4-7e, while the lower spatial resolution data set shows less streamlines connecting to the surface area of the HC (Figure 4-7g). The edge weight values for five of the six edges in the left and right side LS network at 95, 190 and 380 μm isotropic resolution are shown in Figure 4-13. The TH-EC edge is not shown due to its low value (10^2 to 10^3 times smaller than the TH-AM edge) which is the smallest value shown in Figure 4-13. The edge weight variations (error bars) were similar at all analyzed resolutions and all nodes; in some

cases, they decreased with higher resolution, e.g. TH-HC. The HC edge weights consistently decreased with increased resolution in the left and right side networks, whereas the EC-AM increased with increased resolution. The TH-EC displayed a low value edge weight, on the order of 10^{-6} , throughout the left and right sides at 95, 190 and 380 μm resolutions. Also, in three of the six rat brains, at the lower resolution of 380 μm , no calculated streamlines met the criteria discussed in the edge weight section; therefore, no streamlines connecting those nodes contributed to the edge weight in half of the networks. The TH-EC edge is a small and long pathway compared to the other edges in the LS network. Lower spatial resolution obscures the ability to observe this pathway due to volume averaging effects. Longer streamlines, as was shown in the simulation results, increasingly become harder to accurately estimate due to error propagation in the tractography process. Hence higher resolution than 380 μm is needed to estimate the connectivity of small pathways like the HC-EC.

Node strength results are shown in Figure 4-14 and display similar results for left and right LS networks. The standard deviation suggests robustness across changing spatial resolution (i.e., it did not appear to be affected by voxel size). The HC and TH node strengths increased with decreasing resolution, while the AM increased with increasing resolution. The EC did not show resolution dependence on the measured node strength. The HC and TH are nodes are central nodes with reasonably large WM tracks connecting to them. As the spatial resolution is decreased, the appearance of larger and stronger WM tracks dominate the diffusion characteristics in the voxels that represents them yielding larger edge weights. Hence at low spatial resolution it creates coherent WM tracks and reduces the proper characterization of smaller pathways. The

AM node is located in an inferior part of the brain (Figure 4-7) and only small pathways connect to it. Lower spatial resolution minimizes the voxels that contribute to its edge weight and since it only receives inputs from fibers inferior to the node (Figure 4-7) the estimation of these streamlines becomes increasingly difficult when inadequate spatial resolution is obtained. Finally the EC has the particular situation where at low spatial resolution the coherent pathways connecting to the HC get enhanced. Meanwhile, at high spatial resolution the small pathways connecting to the TH and AM become more visible, hence making this edge weight consistent across changes in spatial resolution.

Nodes' surface area and edge length measurements are shown in Figures 4-15 and 4-16. The HC was the largest and most consistently defined node with variations of less than 3%. The variation in the surface area of nodes affects the edge weight measurement (Equation 4-3), since the surface area is used as part of the edge weight measurement. The AM, EC and TH are in close spatial proximity to many other anatomical structures with similar contrast which made the segmentation of these nodes significantly more difficult than the HC. Ample care was taken by the rater (person defining the nodes) to consistently define the LS nodes, which resulted in the small variation in the surface areas observed in Figure 4-15. The spatial resolution affects the edges (Figure 4-7e to 4-7g) through volume average effects causing the measured length of all the edges to decrease with decreased resolution. The ability to resolve all the fibers that make connections is limited by the spatial resolution of the images. At lower spatial resolutions most of the available surface area of the nodes is left without streamlines. Lower resolution (Figure 4-7g) has more area of the node exposed than the higher resolution network (Figure 4-7e), where almost the entire surface of the node

is covered by streamlines. The measured length of all edges is decreased with decreased spatial resolution. The length variation of the edges is not affected with changing spatial resolution (Figure 4-16), which supports the notion that spatial resolution is a limiting factor to resolve small tracts that traverse paths close to the nodes.

4.4. Discussion

Streamline maps inferred from HARDI using tractography allows the study of the large-scale fibrous structure of the brain *in-vivo* (Bassett et al., 2011a; Cheng et al., 2012a; Costa Lda et al., 2007; Gong et al., 2009; Hagmann et al., 2008; Hagmann et al., 2007; Romero-Garcia et al., 2012; Sporns et al., 2007). The use of HARDI data to create binary networks is useful, but weighted networks are better suited to obtain a better understanding of the connectivity strength between nodes of smaller local networks, such as the LS. With binary networks the connectivity between nodes is characterized by the presence or absence of edges. So the connectivity of the LS network described in this chapter would correspond to a completely connected network, hence no new information is obtained since these nodes are expected to be connected. On the other hand, weighted networks add another degree of freedom in the characterization of complex networks and create a more realistic representation of the brain network.

The simulations show that a large number of seeds per voxel are required to reduce the variation of connectivity measures between structures, which is consistent with literature (Cheng et al., 2012b); however, a compromise has to be made between computing storage capacity and seed density to reliably map connectivity between

nodes. Simulations determined that a seed density of several thousand might be the best way to reduce seed density effects to less than 1%. The seed density of 125 is used for the tractography analysis as a compromise to minimize seed density effects to roughly 20% of the plateau value, and to avoid large tractography files. Percentage differences in edge weight from the plateau value did not show variations greater than 20% if the seed density was 125. Nevertheless, the percentage differences of edge weight were never greater than 10% for the same seed density, despite changing the number of voxels separating the nodes.

Simulations showed an increased uncertainty in the edge weight value as random errors in the estimated diffusion direction increased, and the node separation is increased, which agrees with literature results of streamline uncertainty derived from tractography (Miles and Laidlaw, 2012). The percentage difference of less than 11.9% for σ levels of less than 0.03 suggests that high accuracy is required from the diffusion direction profile estimation to calculate the edge weight connectivity. The edge weight's c_v of 7.5 for $\sigma= 0.03$ confirmed low standard deviation requirement (which in turn relates to high SNR) to reduce variations in the edge weight calculation. As the noise is increased, the uncertainty in the estimated diffusion direction is increased (Bastin et al., 1998). Therefore, high SNR in the HARDI acquisitions is needed to maintain accurate fiber estimation (Alexander et al., 2001), and to allow the calculation of a reproducible edge weight measure.

Corpus callosum and cingulum edge weights showed a reduction in the variability of edge weights obtained from a single subject 10 times by using the streamline selection criteria (Section 4.2.2). Edge weight values showed an inter-scan variability

range from 0.5 % to 3.8% in the 1 mm data and 1.1% to 5.5% in the 2 mm data. The difference between the long and short edges is greatly reduced using the criteria presented in *Edge Weight Derived from DWI* (Section 4.2.2). The node placement successfully measured the connectivity of the cingulum and CC disk nodes placed at different locations on the tract path. The percentage difference of the edge weights measured with the proposed restrictive method displayed a smaller change, with nodes measuring the connectivity of CC and cingulum placed at different places along the tract, compared to the more common method of using all streamlines independently of their origin. The nodes were defined to ensure that the full fiber tract was captured in its entirety.

The edge weight is a measure of node connectivity and does not solely depend on the cross sectional area of the tracts. The cross sectional areas of the cingulum and CC tracts were 7.3 and 7.9 mm respectively, which corresponds to a 5.6% decrease in the cross sectional area of the cingulum tract related to that of the CC tract. The cingulum edge weight showed a 53.8% decrease compared to the CC edge weight and there is roughly a 60% decrease in the surface areas. Therefore, the edge weight reflects a measure of connectivity that depends on the surface area (size of the nodes) of the nodes as well on the connectivity strength of the fibers.

The edge weight was used in the rat LS network to quantify the connectivity between anatomical structures. This approach creates a complete network (i.e., every node connected to every other) with the idea that the use of weighted networks can aid in differentiation of node relevance (larger node strengths $s(n)$) within local networks.

The implementation of the edge weight proposed allows for the in-depth study of smaller local networks, as well as larger cortical networks.

The higher spatial resolution of the rat data allowed an improvement in the ability of the rater to differentiate between the node boundaries (Figure 4-7i). The low variation of surface area estimates in the lower resolution data sets is due to the ability to segment in a high-resolution data set and then register these nodes to the lower resolution data sets. A first attempt to segment at the low-resolution data proved to be too difficult due to the lack of clear node boundaries. The HC displayed higher edge weight values with decreased resolution; this can be attributed to its central spatial location within the LS network. The fibers in the LS network mostly travel near the surface of the HC node. Lower resolution averages the majority of the WM structure with the boundaries of the nodes, resulting in a few voxels yielding coherent pathways to and from the TH, AM and EC structures. The EC-TH edge proved to be difficult to capture given its small size and long length. The variance of streamlines from tractography have been proven to increase with increasing arc length from the seed point (Miles and Laidlaw, 2012). Streamline length results (Figure 4-14) show that the EC-TH edge is the longest thus should display the highest variation, which is consistent with Miles et al. findings (Miles and Laidlaw, 2012). Consequently, the spatially close EC-AM nodes display the shortest length but the highest edge weight; thus, Figure 4-7e to 4-7g displays a coherent fiber structure connecting the EC and AM nodes.

4.5. Concluding Remarks

The dimensionless and free of scale network metric described in this chapter improves on currently used edge weights (for tractography) in the literature since it

removes the majority of the acquisition and post-processing parameters that influence the network metrics. Previously studies were mostly devoted to cortical binary graph descriptions, and weighted networks increasingly have gathered attention to describe the connectivity of brain networks. Weighted networks depict brain connectivity in a more realistic manner, because the brain is a complex network with heterogeneous connections (i.e., edges). Appropriate SNR levels are essential to acquire optimal data to estimate the fiber paths connecting anatomical structures (Bastin et al., 1998; Miles and Laidlaw, 2012). Errors associated with low SNR affects the estimated diffusion profiles leading to a propagation of errors in the obtained streamlines from tractography, hence reducing the confidence that the obtained streamlines represent actual brain fibers. Seed density and volume averaging effects gained more influence as resolution was decreased; suggesting high seed density and higher resolution reduces the variability on weighted network metrics. The selection of a high seed density has to be a compromise between computing times and file size. The ability to reliably quantify small tracts stems from appropriate spatial and angular resolution (refers to number of gradient directions used to measure the DWI's), which will ultimately allow the tractography estimation of these pathways. To achieve the highest resolution, acquisition must be a compromise between time and SNR. Additionally, optimized diffusion protocols improve the ability to estimate the diffusion characteristics used for tractography. In the next chapter, the edge weight is used to generalize the framework to study the organizational principles of networks.

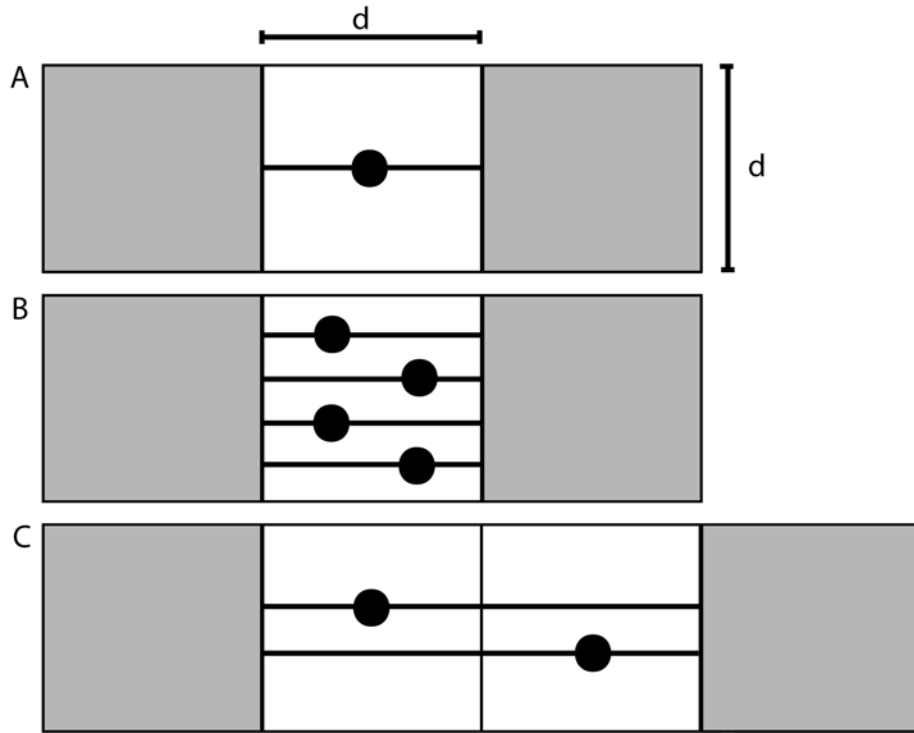


Figure 4-1. WM fiber, contained within the white pixels, connecting two nodes, gray pixels. The fiber lies within a single voxel; the tractography is performed with A) one seed per voxel and B) four seed points per voxel. C) The fiber lies within two voxels; the tractography is performed with one seed per voxel.

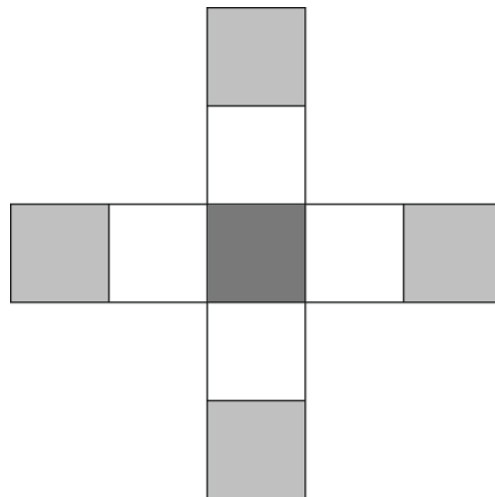


Figure 4-2. A central node (dark gray) connected to four other nodes (light gray), each through a single fiber (white) similar to those shown in Figure 4-1a and 4-1b.

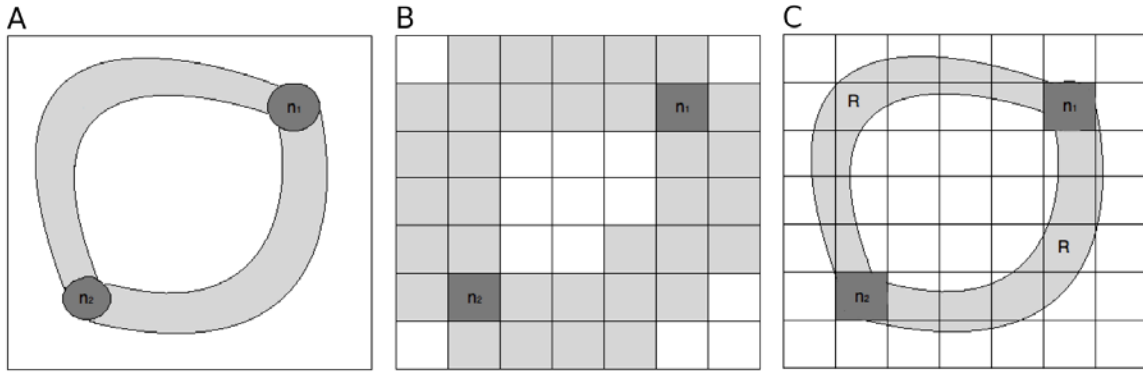


Figure 4-3. A sketch displaying the process used to obtain the set of seed points, M , connecting two nodes, n_1 and n_2 . A) "Real" 2-node system used to quantify the edge weight of the fiber connecting them. B) Labeling MR pixels as nodes (dark gray) and fiber voxels (light gray). C) Region R contains the seed points that contribute to the edge weight.

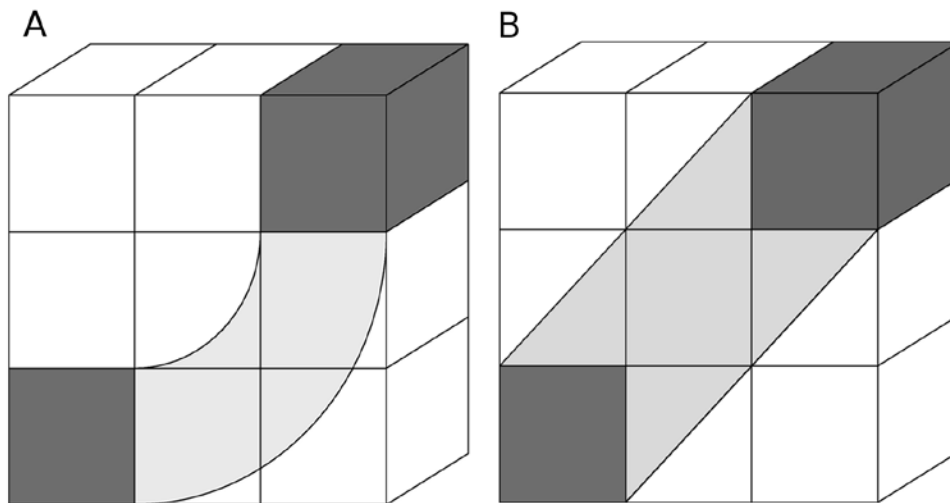


Figure 4-4. 3D sketch of a system of 2 nodes connected by a fiber. A) Arched fiber joining the two nodes exactly at one face of each of the dark gray cubes. B) Slant fiber connecting the two dark gray nodes at two of the six faces of each node. Both fibers A and B travel parallel to the plane shown.

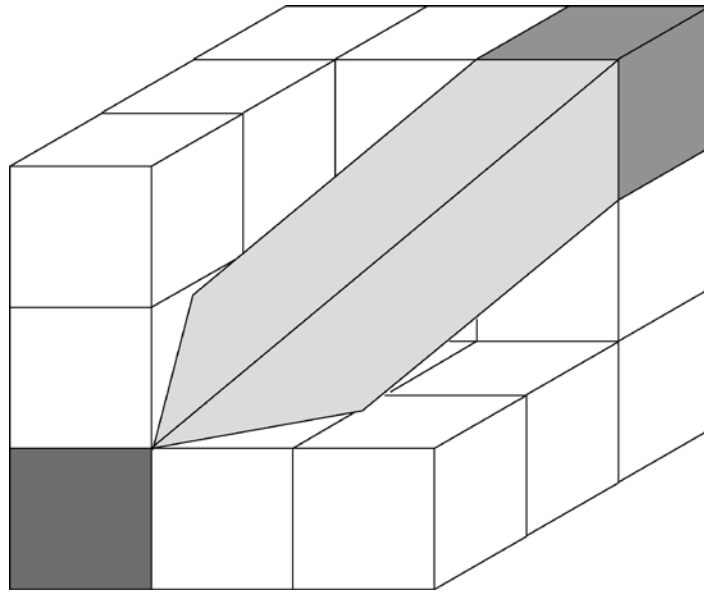


Figure 4-5. Slant fiber path connecting two nodes at different planes. Sketch corresponds to fiber of length equal to $\sqrt{3}$ by the closest two points on each node with angles of $\theta=45^\circ$ and $\phi=54.1^\circ$.

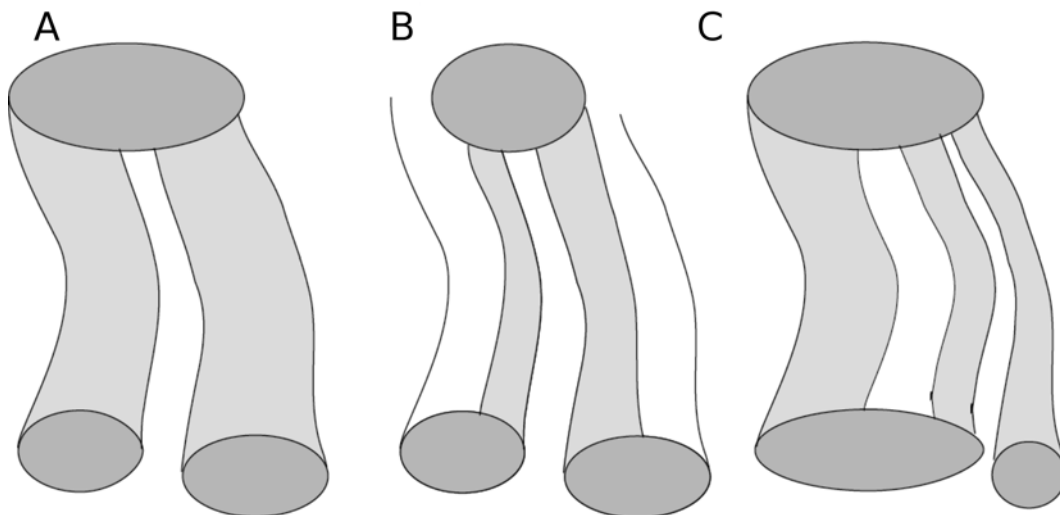


Figure 4-6. Segmentation of a 3-node and 2-edge system. A) The intended three nodes (dark gray) to measure the WM connectivity (light gray). B) Underestimation of the upper node yielding a smaller calculated track connection to the bottom nodes. C) Overestimation of the bottom left node and underestimation of the bottom right node, this yields part of the bottom right node to be assigned as connections to the bottom left node, and a portion of the right tract to be neglected.

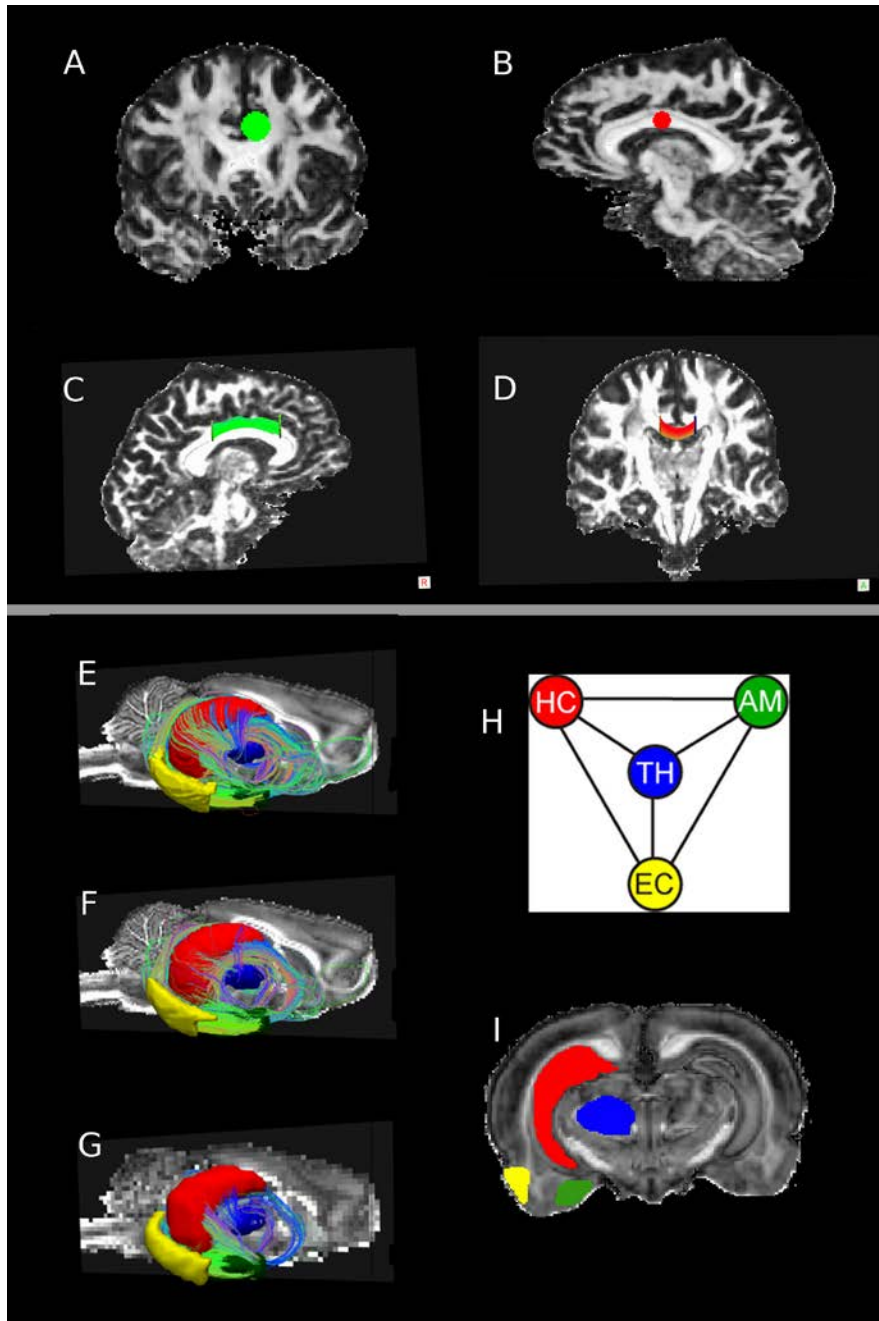


Figure 4-7. Human and rat brain networks. A) Coronal view of the cingulum node. B) Saggital view of the corpus callosum nodes. C) Saggital view of the cingulum network shows the disk nodes and the fiber connecting them. D) Coronal view of the CC network shows the disk nodes and the fiber connecting them. E) TL network at the interpolated resolution of 95 μm . F) TL network with tracks connecting nodes at acquisition resolution of 190 μm . G) TL network at the degraded resolution of 380 μm . H) Sketch of the TL simple graph; hippocampus, HC, thalamus, TH, amygdala, AM, and entorhinal cortex, EC (Color scheme is maintained in all figures). I) Coronal slice displaying the nodes.

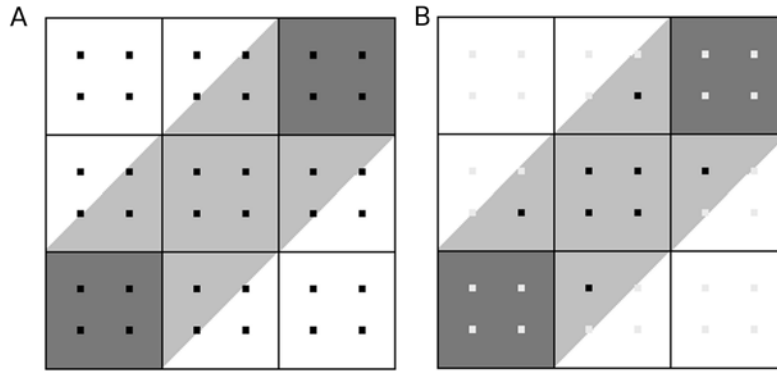


Figure 4-8. System of 2 nodes connected by a fiber at 45 degrees from the pixels.
 A) Color meanings; ROIs to be connected in dark gray, tract to be quantified in light gray and tiny dark squares are the seeds points. B) After keeping the seedpoints that lie within the region R , out of 36 original seed points, only 8 contribute to the edge weight.

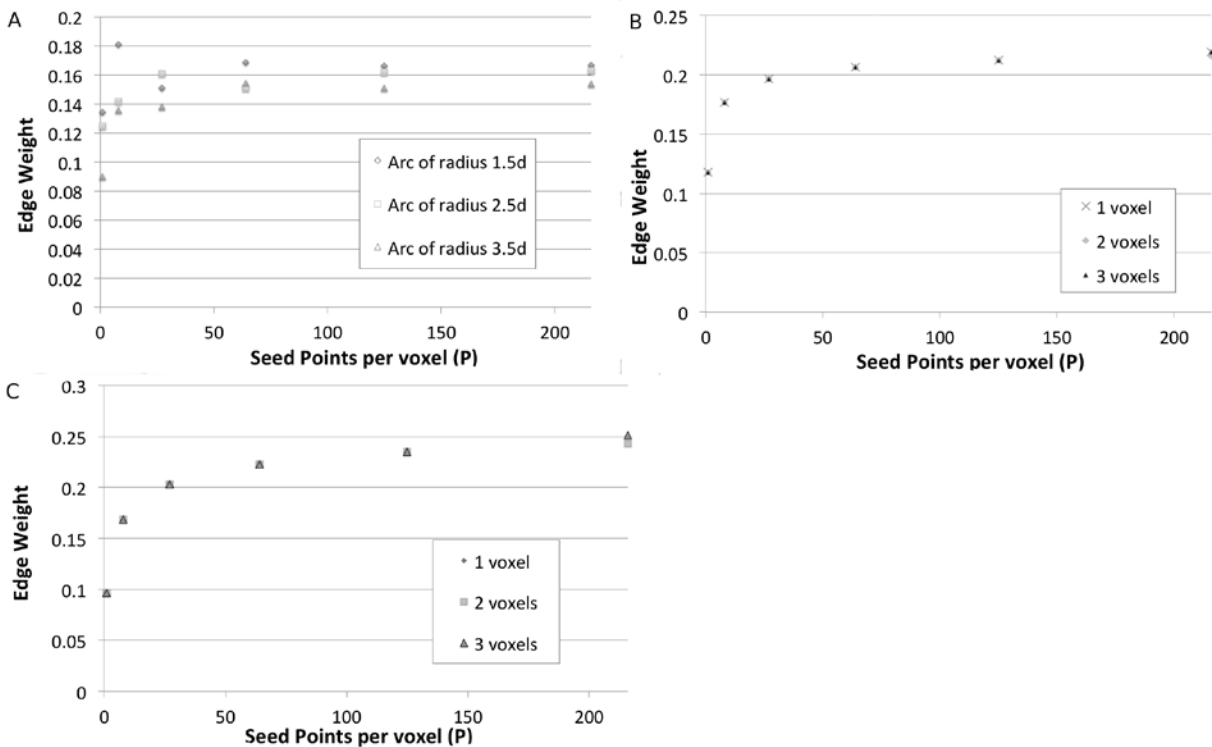


Figure 4-9. Edge weight (Equation 4-6) plots of arc and slants of Figures 4-4 and 4-5.
 A) Arc edge weight plateaus to: 0.167 for radius, r , of 1.5, 0.166 for $r=2.5$ and 0.165 for $r=3.5$. B) Slant in plane edge weight plateaus to: 0.234 for a separation of one voxel through its closest point, 0.233 for a separation of two voxels, and 0.233 for a separation of three voxels. C) 3D slant plateaus to: 0.284 for a separation of one voxel to its closest points, 0.282 for a separation of 2 voxels and 0.281 for a separation of 3 voxels.

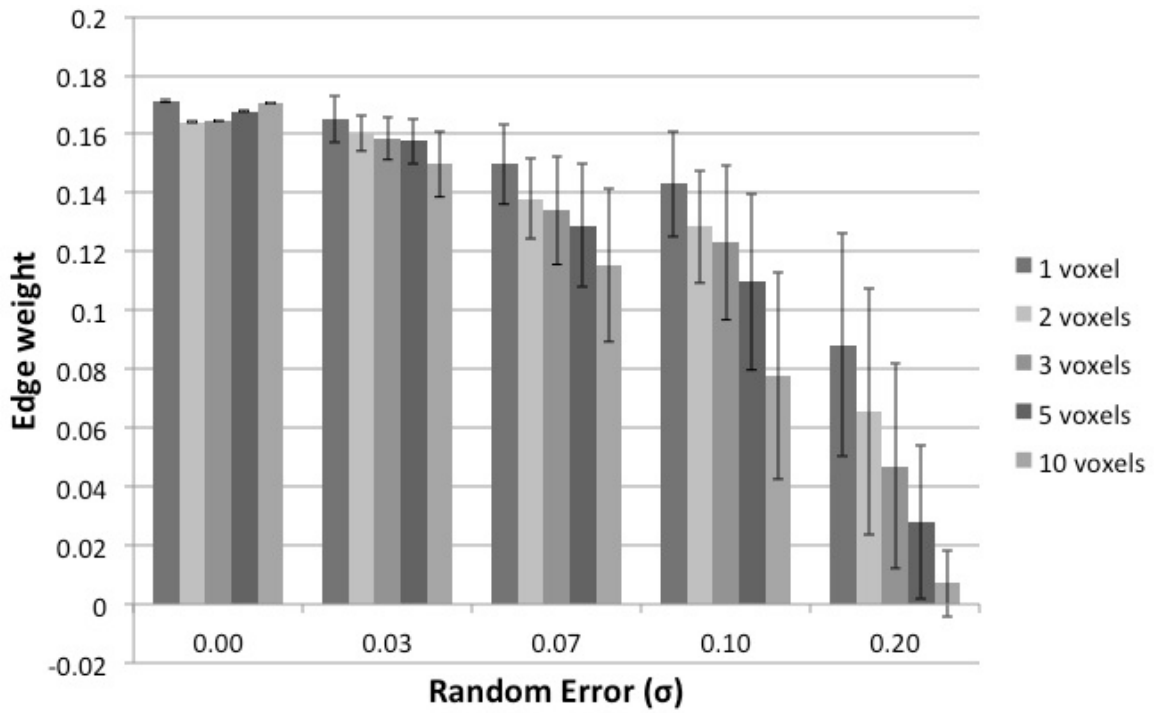


Figure 4-10. Edge weight values for a slant in plane of single voxel nodes. The nodes closest points were separated by; 1, 2, 3, 5, and 10 voxels.

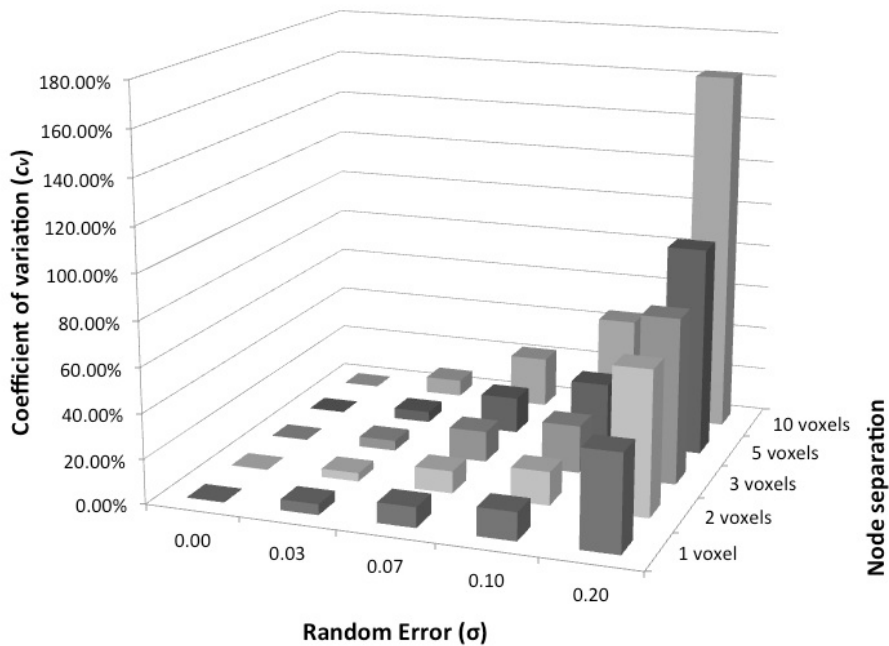


Figure 4-11. Coefficient of variation (c_v) plots as a function of σ levels and node separation. The nodes closest points were separated by; 1, 2, 3, 5 and 10 voxels.

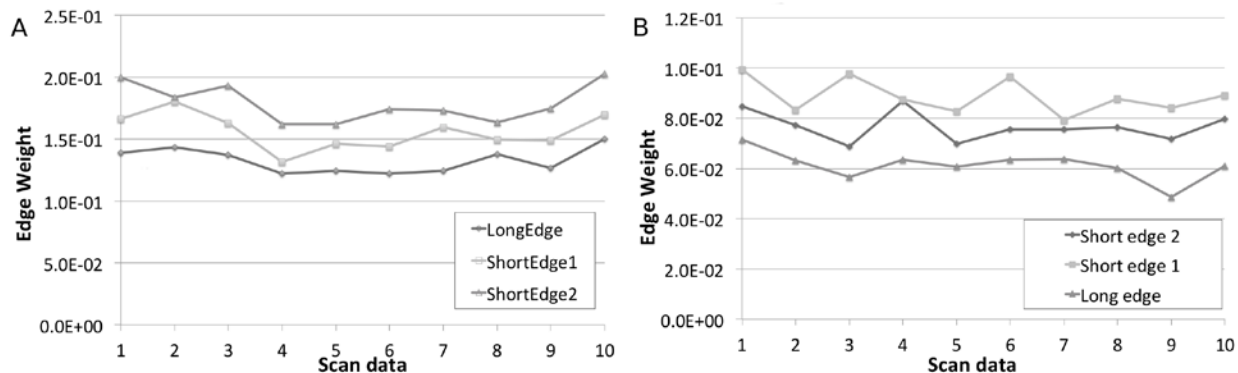


Figure 4-12. Edge weight plots for disk nodes in the cingulum and corpus callosum tracts. A) Corpus Callosum disk nodes edge weights, B) cingulum disk nodes edge weights.

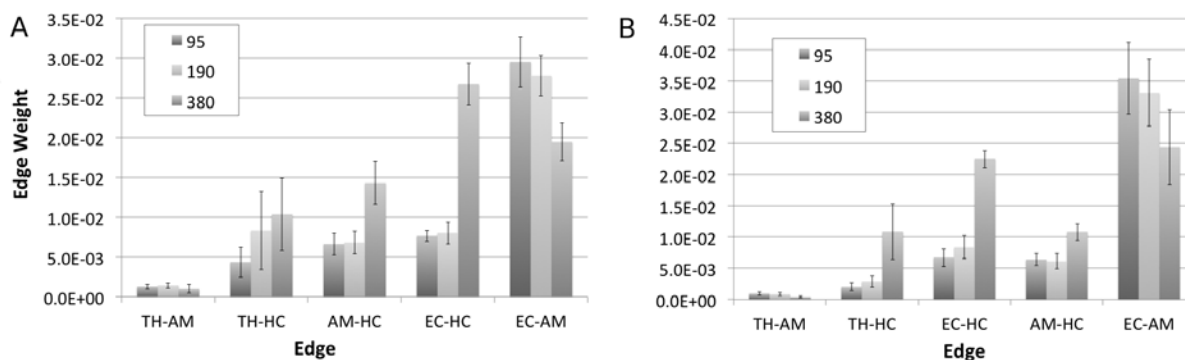


Figure 4-13. Excised rat brain edge weight values in the TL network. A) Left and, B) right side TL edge weights. Values shown are across different resolutions of 95, 190 and 380 μ m. TH-EC not displayed due to its small value.

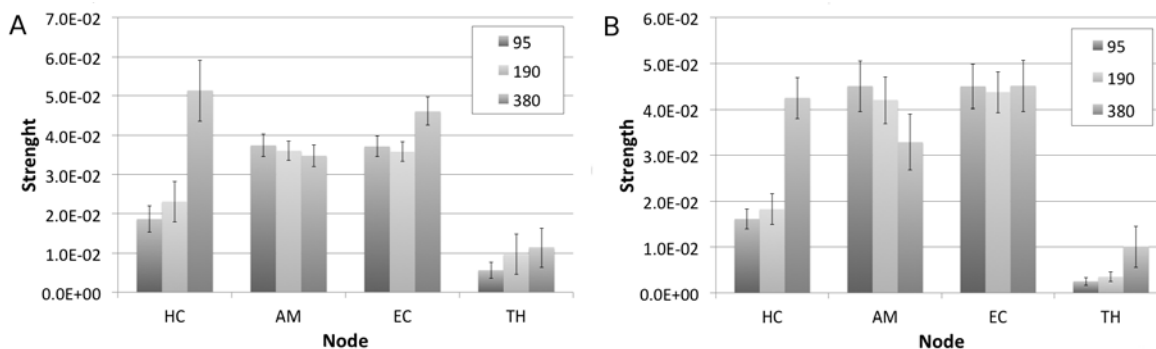


Figure 4-14. Excised rat brain node strength values in the TL network. A) Left and B) right side TL node strength values. Values shown are across different resolutions of 95, 190 and 380 μ m.

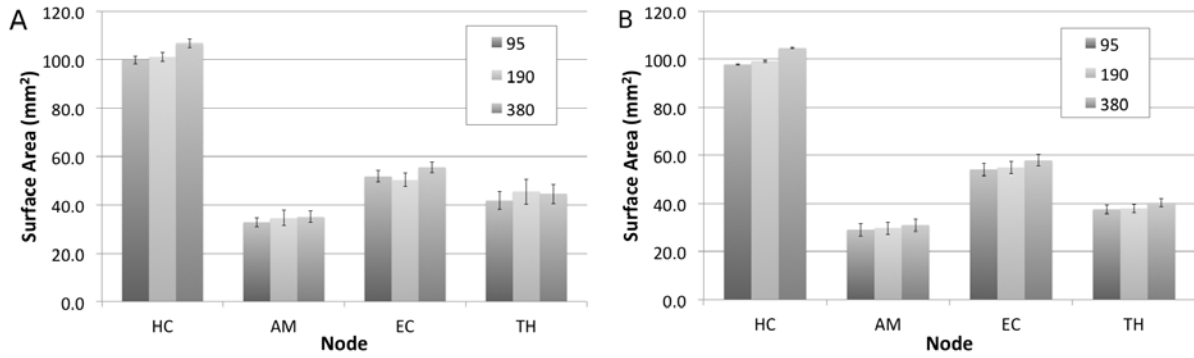


Figure 4-15. Excised rat brain surface area values for the TL structures. A) Left and B) right side TL node surface area measurement. Values shown are across different resolutions of 95, 190 and 380 μm . Segmentation was performed in the 95 μm data set and registered onto the 190 and 380 μm sets using FSL's FLIRT and ApplyXFM.

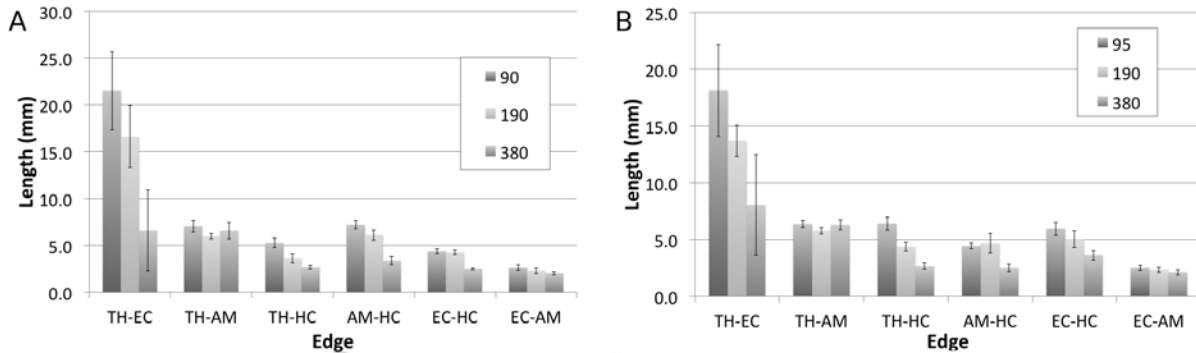


Figure 4-16. Excised rat brain edge length values in the TL network. A) Left and, B) right side TL edge lengths. Values shown are across different resolutions of 95, 190 and 380 μm . Observed fiber length differences in Fig. 7 are more pronounced on the TH-EC edge.

Table 4-1. Edge weight values across the acquired ten data sets of 1 mm³. The proposed restriction, i.e. criteria 1 and 2, to obtain the fiber connecting fibers reduces the variation across different scans.

Edge (e)	Proposed restrictive method		Common approach, no restriction	
	w(e)	c _v	w(e)	c _v
CC (long)	1.33E-01	7.57%	9.42E-01	10.44%
CC (short 1)	1.56E-01	9.29%	2.26E+00	13.09%
CC (short 2)	1.79E-01	8.54%	2.77E+00	9.05%
Cingulum (long)	6.12E-02	9.52%	2.56E-01	12.36%
Cingulum (short 1)	7.66E-02	7.74%	5.64E-01	9.76%
Cingulum (short 2)	8.87E-02	7.80%	7.02E-01	9.80%

Table 4-2. Edge weight values across the acquired ten data sets of 8 mm³. The proposed restriction, i.e. criteria 1 and 2, to obtain the fiber connecting fibers reduces the variation across different scans.

Edge (e)	Proposed restrictive method		Common approach, no restriction	
	w(e)	c _v	w(e)	c _v
CC (long)	9.62E-02	11.13%	6.06E-01	15.24%
CC (short 1)	1.16E-01	9.55%	1.62E+00	15.01%
CC (short 2)	1.33E-01	9.88%	1.95E+00	13.29%
Cingulum (long)	4.31E-02	12.49%	1.50E-01	15.12%
Cingulum (short 1)	5.75E-02	10.73%	3.57E-01	11.86%
Cingulum (short 2)	6.26E-02	8.15%	4.06E-01	13.57%

CHAPTER 5 TOPOLOGY OF WEIGHTED BRAIN NETWORKS

5.1. Opening Remarks

Structural network studies generally use binary connectivity representations, in which every connection between nodes is equivalent (Hagmann et al., 2007; Iturria-Medina et al., 2007). Consequently in binary representations, the connection either exists or does not exist. In reality, the brain is a heterogeneous system comprised of a range of WM connection strengths (Catani et al., 2002; Concha et al., 2005). Also, computational models of neural networks were proven to display enhanced synchronizability using weighted networks (Chavez et al., 2005). Therefore, to account for the enhanced behavior obtained from simulations of weighted computational models, the analysis of network structures necessarily has to include a weighted connection between nodes to describe brain networks. Because the relative “strength” of white matter tracts in the brain varies, weighting the network is necessary to differentiate between the network connections of various strengths (Butts, 2009). Additionally weighting the edges of the network adds an extra degree of freedom to calculated network parameters. Various weighted network parameters have been proposed in literature, but a comprehensive weighted connectivity framework has not been proposed that allows the estimation of topological traits of networks, such as those of a small world (Watts and Strogatz, 1998) or a scale free (Barabási and Albert, 1999) network.

In this chapter, a generalization of the framework used to study brain network organization is introduced then applied to determine the advantages that weighted edges have on the calculated measures of network connectivity. The usual framework used to estimate the topology of brain networks includes the calculation of the degree

distribution, path length and clustering coefficients (Watts and Strogatz, 1998). In separate works, all of these calculations have been generalized to weighted networks. With these generalized network measures the topological features (small world or scale free organization) of brain networks are estimated using a weighted network. This approach leads to a more realistic model of the brain network, which leads to a more robust characterization of the network topology.

5.2. Methods

The procedures used to construct the human cortical networks are described in this section. First the procedure to obtain the nodes is described and then the edge assignment and weighting is reexamined from Chapter 4.

5.2.1. Network Construction

In brain networks created from tractography, thresholds are usually employed to reduce the number of artifactual streamlines and the effects of volume averaging of the voxels in network measures. In binary networks thresholding introduces two problems into the networks calculations. The first is the arbitrary selection of the threshold and the second issue that arises is that networks with different thresholds are not independent samples (Langer et al., 2013). First, the arbitrariness of chosen thresholds does not ensure that real edges are not eliminated or that artifactual edges are eliminated, since there is not a clear criterion to achieve the elimination of artifactual streamlines. Also, the statistical results obtained for all networks will depend on the selected thresholds. Secondly, networks created at different thresholds are pseudo replicas of group level networks (Langer et al., 2013). This means that the results obtained from the same data

expressed as a sparse network is also contained in a dense network, but not vice-versa. This indicates that there is direct dependence of the calculated network properties on the applied threshold, which leads to different results at different thresholds. In this chapter, binary and weighted metrics are calculated for networks created at different thresholds to determine whether weighting the network's edges allows better estimation of an appropriate threshold or if it is possible to eliminate it from the analysis.

Low edge weight values are commonly used as thresholds to eliminate what could be considered artifactual edges connecting any two nodes. In binary networks, sparse networks (i.e. the number of edges is much less than 30% of the total number of possible edges) allow better estimation of the topological properties of networks, because the nodes of dense networks become highly connected, almost leading to a complete graph (every node connected to all others in the graph). Hence thresholds also aid in the characterization of the topological properties of binary networks. In this work, a high seed density ($P_{\text{voxel}} = 125$) is used to maximize the accuracy of the calculated edge weights, and the edge weight itself is calculated to reduce the effect of artifacts (Section 4.3.1) (Colon-Perez et al., 2012). In this chapter, thresholds will be set low enough so that “weak” edges are not removed just to create sparse networks. To determine an appropriate threshold level, suppose that a characteristic “small” edge in the brain network has a length of 3 mm and the streamline fibers are entirely contained within three voxels. Using Equation 4-3, a total of 375 streamlines ($M \times P = 3 \times 125 = 375$) should be connecting the nodes; therefore, a threshold of 125 streamlines or more would require that at least ~33% (i.e. $125 / 375$) of all streamlines that potentially make up the edge to be present. Consequently the number of streamlines connecting any two

nodes, and not the edge weight value, will be used as a threshold for the edges of the brain network. As stated before thresholds are arbitrary, and this one is not the exception. In this dissertation the number of streamlines will serve as the criterion to compare results of network measures in binary and weighted networks constructed at different thresholds. Considering the high volume of seeds per voxel used in this work, three thresholds will be used to examine the effects of thresholding on calculated network parameters. First, binary and weighted network parameters will be calculated in networks without applying any threshold, i.e. any two nodes connected by at least one streamline will have an edge. Then edges with 25, 50 and 125 or more streamlines will be considered valid edges. In other words, 4 networks will be studied in this chapter; one with no applied threshold (this will be referred as 0 threshold), then a threshold of 25, 50 and 125 streamlines or more making up an edge (these last three will be 25, 50 and 125 threshold, respectively).

An automatic segmentation algorithm called Freesurfer was used to define sets of 68 anatomical nodes (Table 5-6 has a list of the nodes and their appropriate label numbers used in the figures of this chapter) in all of the human data sets (Fischl, 2012; Fischl et al., 2004). Freesurfer uses the T1 weighted images (i.e. structural images) to register each structural image to an atlas of predefined anatomical brain regions. First the algorithm removes the skull and creates an atlas of the white matter in the brain (based on intensity values of each pixel in the structural image) to set the points that determine the boundaries of the brain regions. This first step creates two brain structures: WM, and everything else. The non-WM structure is ultimately segmented into the predefined anatomical nodes in each brain. The structural image was then

registered to diffusion weighted images using FSL's FLIRT (Jenkinson et al., 2002) algorithm, using an affine transformation. The affine transformations include: rotations, translations, and dilations and/or shears. Employing FLIRT's transformation matrix output, Freesurfer's nodes were then registered from the T1 weighted image to DWI using FSL's ApplyXFM.

To avoid repetition the reader is referred to Section 4.2, which describes in detail the procedure used to define each edge of the human cortical networks used in this chapter. The edge weight as described by Colon-Perez, et.al.(Colon-Perez et al., 2012) and Chapter 4 is used to estimate the connectivity strength of the edges in the network.

5.2.2. Null Hypothesis Graphs

The results of network metrics are influenced by the decisions made in creating the network (e.g. number of nodes and edges, and the degree distribution). Therefore, to test the significance of the brain network results (i.e. clustering coefficients and path lengths) they are compared to results obtained for null hypothesis graphs. Null hypothesis graphs of binary networks are formed by selecting edges at random with two constraints: 1) the number of nodes and 2) the degree distribution remains identical to the original brain network obtained for example by tractography. Since these graphs are constrained by the number of nodes and the degree distribution, differences between null hypothesis graphs and graphs obtained from brain networks are not due to local differences in connectivity (i.e. node degree discrepancies) (Sporns, 2011).

Null hypothesis networks are employed in this study to determine the structural organization and the topological traits of brain networks. Weighted null hypothesis networks (like the ones to be described now) have not been described before. To create

weighted null hypothesis networks a third constraint is proposed to account for the additional degree of freedom resulting from weighting the edges of the network. The weighted null hypothesis networks will preserve the number of nodes, the degree distribution (similarly to the binary case) and in the weighted case the edge weight distributions of the original brain networks will also be preserved. The process of creating null hypothesis graphs starts by storing lists of the edge weight values and the node degree distribution (binary) for each brain network. Then, starting with the same number of nodes as the brain network, the edges are assigned at random to connect node pairs, with the restriction that the node degree distribution is preserved. As each edge is assigned, simultaneously an edge weight is randomly selected from the edge weight list and is applied to weigh the edges of the null hypothesis network. Ultimately, this creates a random network (i.e. a weighted null hypothesis graph) with the same node degree and edge weight distribution as the calculated brain network.

5.3. Network Metrics

The weighted edges require expanding the adjacency matrix to contain an extra parameter that accounts for the strength in connectivity on each edge. The binary adjacency matrix A , becomes the weighted connectivity matrix, A' (Newman, 2010) and the elements of the connectivity matrix are given by

$$a'_{ij} = a_{ij} \cdot w(e_{ij}) . \quad (5-1)$$

where $w(e_{ij})$ is the edge weight (Equation 4-6) defined in the section “Edge weight Derived from DWI” (Section 4.2.2). The weighted connectivity will allow calculating weighted network metrics analogous to the ones derived from the adjacency matrix

(Section 2.2.1). The weighted connectivity matrix will become the foundation that allows generalization of the framework that estimates the topological properties of weighted networks (Watts and Strogatz, 1998).

5.3.1. Node Connectivity

The degree (Section 2.2.1) can be generalized to study weighted networks by substituting the adjacency matrix with the weighted connectivity matrix, where the element ij represents the strength of connectivity between nodes i and j . With the ability to calculate the edge weight, the degree (Equation 2-6) can be generalized by substituting the degree with node strength (Newman, 2001). The node strength ($s(n_i)$) is expressed as

$$s(n_i) = \sum_{j=1}^N a'_{ij} = \sum_{j=1}^N a_{ij} \cdot w(e_{ij}) . \quad (5-2)$$

5.3.2. Average Weighted Path Length

Average path lengths reveal how effectively any node communicates with all of the others in the network. A generalization of path length (Section 2.2.1) can be made by the use of Dijkstra's algorithm to find a single path between nodes i and j , where the strongest path is used to connect any two nodes. Details of the algorithm can be found in *Introduction to Algorithms* (Cormen et al., 2009). Essentially in weighted networks, the algorithm searches for strong paths, i.e. the largest sum of edge weights connecting any two nodes along any path with the least number of edges (there may be several

paths with the least number of edges). Equation 5-3 defines the average weighted path length.

$$l'(n_i) = \frac{\sum_{j=1}^N pl_{ij}}{N-1} \quad (5-3)$$

where pl_{ij} represents the largest sum of edge weights traversed along the shortest path between node i and node j . Networks may contain several shortest path, in such cases the strongest path length is the path that yields the highest sum of the edge weights along a shortest path. It is important to note that the path length in this context is not a measure of Euclidean distance, i.e. the binary path length between any two nodes is not the distance between their center of masses, but the number of steps it takes to connect them (Equation 2-18). In the weighted framework, as stated before, the weighted path length is the largest sum of edge weights along the shortest path. For example, in Figure 5-1 the Euclidean distance from node a - c should be a path from a to c , since these are not connected as a network $pl_{ac} = w(e_{ab}) + w(e_{bc}) \neq w(e_{ac})$. In a binary network, the edge weight, $w(e_{ij}) = 1$, therefore $pl_{ac} = 2$ since information has to travel from a to b and then arrive at c .

The graph in Figure 5-2 will serve as a demonstration of Dijkstra's algorithm. The algorithm starts off with the weighted connectivity matrix as the estimation of the strongest path for nodes connected by one edge, and the zero elements are estimated with the strongest path connecting the nodes linked via two or more steps. To calculate the weighted path from node n_1 to n_6 in Figure 5-2, the algorithm will find the lowest cost by obtaining the highest sum of weights of the edges connecting n_1 - n_6 . The starting node, n_1 , has three neighbors, two of which connect to n_6 . The algorithm compares pl_{16}

experiencing the path, $w(e_{13})+ w(e_{36})$ and $w(e_{12})+ w(e_{26})$. From a visual inspection of each path on Figure 5-2, it can be determined that $w(e_{13})+ w(e_{36}) > w(e_{12})+ w(e_{26})$: therefore, $p_{16} = w(e_{13})+ w(e_{36})$. This process is repeated in all zero elements of the weighted connectivity matrix until all the $[(N \times (N-1)) / 2]$, paths are estimated with the value of the strongest path connecting the nodes.

5.3.3. Clustering Coefficient

The clustering coefficient relates how well connected the neighbors of a node are to the other neighbors of the same node. It provides some sense of the strength of the communities formed around the nodes of the network. Multiple generalizations of the clustering coefficient (Section 2.2.1) have been proposed in the literature, such as Onnela, $c_{i,0}$ (Onnela et al., 2005) and Zhang, $c_{i,z}$ (Zhang and Horvath, 2005). Saramaki summarizes the properties among all weighted clustering coefficients, c_i (Saramaki et al., 2007). Saramaki et.al. concludes that there is not an all-purpose weighted clustering coefficient. They argued that any network characterization should be made from two perspectives: binary and weighted. In this dissertation two weighted clustering coefficients will be used since there is no consensus on an appropriate weighted clustering coefficient to study brain networks. The weighted clustering coefficients used in this work are given by

$$c_{i,0} = \frac{1}{k_i(k_i - 1)} \sum_{j,k=1}^N (\hat{w}(e_{ij})\hat{w}(e_{jk})\hat{w}(e_{ki}))^{1/3}, \quad (5-4)$$

and

$$c_{i,Z} = \frac{\sum_{j,k=1}^N (\hat{w}(e_{ij})\hat{w}(e_{jk})\hat{w}(e_{ki}))^{1/3}}{\left(\sum_{j=1}^N \hat{w}(e_{ij})\right)^2 - \sum_{j=1}^N (\hat{w}(e_{ij})^2)}, \quad (5-5)$$

where

$$\hat{w}(e_{ij}) = \frac{w(e_{ij})}{\max(w(e))}. \quad (5-6)$$

These generalizations were chosen because they have the property that as $w(e_{i,j}) \rightarrow 1$, in all of the edges of a graph, the weighted clustering coefficient tends to $c_i \rightarrow 1$, for any triangle (i.e. three nodes fully connected between them). This ensures that the results in weighted networks will yield the expected binary results as $w(e_{i,j}) \rightarrow 1$

5.3.4. Small Worldness

The last metric to be used is called small worldness (Humphries and Gurney, 2008). This metric takes the calculation of clustering coefficients and path lengths into account and also considers the fact that small world networks deviate from random networks predictions. Small world networks are “more” clustered and display more “similar” mean path lengths than those predicted in Erdős’ and Rényi’s model (random graphs called ER graphs, Section 2.2.2). Instead of using ER graphs in this chapter, null hypothesis graphs are employed as control graphs to compare the brain networks. To employ the small worldness parameter, the null hypothesis graphs will be analogous to the ER graph, and the brain networks are analogous to the small world graphs

described by Watts et. al (Watts, 2003). This null hypothesis network provides a better comparison because the degree distribution and edge weight distribution are maintained in both brain and null hypothesis networks. To calculate small worldness, the ratio of the clustering coefficient (Equation 5-7) and average path length (Equation 5-8) for each network is compared with the null hypothesis graph.

$$\gamma = \frac{c_g}{c_N} \quad (5-7)$$

where c_g is the average clustering coefficient for a brain network and c_N is the average clustering coefficient for a null hypothesis network.

$$\lambda = \frac{l_g}{l_N} \quad (5-8)$$

where l_g is the average path length for the brain network and l_N is the average path length for the null hypothesis network. Finally, the parameter for small worldness, sw , takes the form of the ratio of Equations 5-7 and 5-8, and is expressed as

$$sw = \frac{\gamma}{\lambda} \quad (5-9)$$

Real binary networks usually display $\gamma > 1$ and $\lambda \sim 1$, in this dissertation these results are extended to weighted networks to estimate its organizational properties. Binary small world networks present a high degree of connections among the neighbors of any node when compared to a null hypothesis network, but the small average path lengths are preserved. In weighted networks, these notions will be extended so that any node will present a strong level of connectivity among its neighbors while the strong path lengths will be preserved.

5.4. Results

In this section, the results of brain networks and null hypothesis graphs (Binary and weighted) are summarized. The graph density, ρ , is defined as number of edges divided by the total numbers of possible edges in the graph (from this point on any reference to density will be specifically related to the aforementioned graph density parameter). The minimum optimal graph density to determine small world organization in brain networks derived from MRI has been studied before (Romero-Garcia et al., 2012). It was found that an optimal graph density is roughly 8% and the maximum calculated small worldness value was 2.38. As the number of nodes is increased, the small worldness values increase due to a decrease in the density of edges in the graph. This is due to the fact that at a larger number of nodes these become less likely to be statistically correlated due to the reduced scale of the nodes (i.e. size of nodes). The graph density will affect the binary metrics (described in the Networks Metrics section 2.2.1); such that as $\rho \rightarrow 1$, the path length and clustering coefficient will approach 1, since most of the graph will be populated. Figure 5-3 shows how the graph density changes for all 10 networks of a single subject (Section 3.1.1) as the thresholds increase. The thresholding reduced the edge density from ~51% (0 threshold) to ~30% (125 threshold) (Figure 5-3). This chart shows that the level of variation is consistent across all networks with coefficients of variation (standard deviation/mean) of 3.5%, 3.7%, 3.7%, and 3.8% for networks created with the thresholds of 0, 25, 50, and 125 respectively. From this point on, the order of all comparisons across thresholds will be shown from 0, 25, 50, to 125.

Average degree values are shown in Table 5-1 for all applied thresholds. Average degree variations for each node on all ten networks at each threshold are

12.3%, 14.5%, 13.8%, and 13.9%. Figure 5-4 shows the average degree values for each node, the bars represent the variation across the ten networks. Observing the y-axis on Figure 5-4 and Table 5-1, one can see the changes in average degree decreasing with the increasing threshold. This is expected since, as the threshold is increased, it reduces the number of edges from ~51% (0 threshold) to ~30% (125 threshold) (Figure 5-3). The overall shape of Figure 5-4 was maintained at all thresholds (i.e. the high degree nodes were the same at all thresholds). Since thresholds eliminate “weak” edges, these connections appear to be distributed evenly within the entire network. As was stated before, there are 68 nodes in the cortical network employed in this chapter; for the sake of clarity, the nodes names will not appear in the figures as it would make them too crowded and impossible to read. In this section the discussion of specific nodes will be reserved for the nodes with extreme values, since discussing each node result in detail would be too long and confusing to the reader. As the threshold is changed, the node degree shows reductions from 0% (paracentral lobule node, comparing node degree at 25 and 50 thresholds, this is the only node that did not change degree from one threshold to the next) to up to 62% (frontal pole node, comparing node degree at 0 and 125 thresholds). The nodes with the highest degree across all thresholds are the left (L) parietal lobe (Label 28), the right (R) superior frontal cortex (Label 62) and L superior frontal cortex (Label 27). The average node degree of L parietal lobe is: 56.8, 47.1, 45.1 and 41.6, across thresholds. The average degree of R superior frontal cortex is: 56.3, 43.6, 40.8 and 36.2, across thresholds. The average degree of L superior frontal cortex is: 53.5, 43.3, 39.7 and 35.9, across thresholds. The label numbers in parenthesis represent the nodes number in Figure 5-4. The removal of

“weak” edges reduces every node degree value (except for paracentral lobule comparing the degree at 25 to 50 thresholds) at each threshold.

As the threshold is increased, “weak” edges are removed which reduces the degree of the nodes connected by these weak edges. The biggest degree reductions, on average, were found when comparing the degree of non-thresholded networks with the thresholded networks: 28.4% (0 and 25), 34.0% (0 and 50), and 40.7% (0 and 125) while thresholded networks showed a decrease of 7.7% (25 and 50), 17.5% (25 and 125) and 10.6% (50 and 125). To observe whether these networks display the scale free characteristics of hubs, degree distributions on log-lin plots are shown on Figure 5-5. A scale free network would display a long tail as the node degree increases, implying the presence of high degree nodes, called hubs. This long tail is not observed; instead, a sharp decay is observed at the highest degree. In other words, hub nodes are not present in these networks. Consequently, the brain does not appear to display a preferential attachment organization (i.e. scale free organization, Section 2.2.4) agreeing with previous results employing tractography (Hagmann et al., 2007).

Average node strengths are shown in Table 5-2 for all applied thresholds. The average node strength is constant and the variation is 9.6% at all thresholds. The node strength’s uniformity across all thresholds is due to the edge weight value of weak edges; on average these edges exhibited smaller edge weight values than the majority of edge weights by more than 100 orders of magnitude. Therefore, eliminating these small edge weights from the node strength calculation resulted in the small variations observed in the node strength calculation as thresholds are increased. As the threshold is changed, the node strength showed differences from 0% to 0.24%. Average node

strengths and variations (Figure 5-6) did not significantly change as the threshold was varied. Although Figure 5-6 seems to display the same plot four times this not the case. The changes in node strengths are so small that distinguishing the node strengths at 0 and 125 thresholds becomes almost impossible. This is in stark contrast with the degree result (Figure 5-4) which displays clearly visible changes with changes in threshold. Node strength distributions are displayed in Figure 5-7 and, as in node distribution, a preferential attachment organization is not observed (i.e. power law decay). In Figure 5-7 as the threshold is changed the node strength distribution is minimally affected, unlike Figure 5-5. The node strength distributions indicate that thresholding does not have a significant effect on node strength calculation using the edge weight (Equation 4-6). The nodes with the highest node strength across all thresholds are the L insula (Label 34), the R caudal anterior cingulate (Label 36) and the L posterior cingulate (Label 22). The label numbers in parenthesis represent the nodes' numbers in Figure 5-6. The average node strengths of L parietal lobe, the R caudal anterior cingulate and the L posterior cingulate are: 0.127, 0.125 and 0.123 respectively, across thresholds (the anatomical location and shape of these nodes is shown in Figure 5-14). These nodes contain big coherent WM tracks associated to their connectivity with the rest of brain. Quantitatively these large tracks are represented with large edge weight values; hence the node strength of the aforementioned nodes is increased by the presence of these large pathways.

The changes in the binary and weighted adjacency matrices are shown in Figure 5-8. As the threshold is changed, the binary matrices display significant variation on the adjacency matrices, while no noticeable difference is observed in the weighted

matrices. The highest edge weight values are observed as red points in the top-left and bottom-right quadrant of the weighted connectivity matrices. These represent inter-hemispheric connections between the L and R caudal anterior cingulate cortex ($w(e) = 0.090$, shown in Figure 5-15), the L and R medial orbitofrontal cortex ($w(e) = 0.054$, shown in Figure 5-15) and the L and R rostral anterior cingulate cortex ($w(e) = 0.054$, shown in Figure 5-15). These connections facilitate information transfer from the right to the left side of the brain. The corpus callosum (large and coherent WM track) is the main WM pathway associated with these connections, and as it has been said before, large and coherent WM pathways are represented by large edge weight values.

Figure 5-9 displays the path length distribution for all thresholds and reveals that the brain networks are organized in favor of shorter path lengths. As the thresholds were increased the path lengths were also increased, this is seen in Figure 5-9 as shift towards longer paths lengths as thresholds were increased. When the graph density is high, weak edges serve as shortcuts in the network. At all thresholds, it was found that all nodes had an average path length shorter than 2.5 steps, even when the thresholding reduced the edge density by 20% from the 0 to 125 threshold (Figure 5-3). Average path length values of the entire brain graph are shown in Table 5-2, which ranges from 1.51 to 1.79, across thresholds. The node with the shortest path length was the L superior parietal lobe (Figure 5-14) across all thresholds; 1.16, 1.31, 1.34 and 1.39 (from 0 to 125 thresholds respectively). The R superior frontal cortex displayed the second shortest path length values with network of high density (0, 25 and 50 thresholds) with values of; 1.17, 1.36 and 1.41, while the L lateral occipital lobe displayed the second shortest path length at the lowest density (125 threshold) with a

value of 1.48. Also displayed on Table 5-3 are the results of average path length for the null hypothesis networks, which as expected display similar and slightly shorter path lengths ranging from 1.50 to 1.72, across thresholds. The short path length found in this work suggests an effective network organization for information traveling along the edges of the network. The path required to deliver information in brain networks has to only traverse a few nodes before reaching the recipient node, this ultimately reduces the probability of information being distorted as it travels through the network.

A broad range of weighted path lengths was obtained as shown on Figure 5-10, with values ranging from 8×10^{-4} to 3×10^{-3} . Unlike node strength, the weighted path length displays a higher vulnerability to thresholding and shifts the bulk of the distribution to higher values, i.e. to stronger paths, as the thresholds are increased. This effect can be observed as well in the strongest path lengths obtained at different thresholds (Table 5-4). Removing weak edges did not had a significant modification to the obtained node strengths (Table 5-2) and the weighted connectivity matrix (Figure 5-8) since they only made small contribution to these parameters. The weighted path length does not share the robustness as thresholds are change displayed by the node strength and the weighted connectivity matrix. This is due because as weak paths are removed these essentially get replaced by paths that lasted the thresholding process, which finally leads up to significantly stronger path lengths. The effect of thresholding becomes evident looking at the strongest paths at each threshold. The strongest path lengths were: The R caudal anterior cingulate cortex at high graph densities (0 and 25 threshold), while L caudal anterior cingulate cortex displayed the highest value in the 50-threshold network, finally the transverse temporal cortex displayed the highest value

at low graph density (125 threshold). Table 5-4 shows that the means of the brain network path lengths range from 1.08×10^{-3} to 1.57×10^{-3} , while mean weighted path lengths on the null hypothesis graphs range from 1.40×10^{-3} to 2.23×10^{-3} , yielding larger weighted path length values than the brain networks. The strong weighted path length proposes that the brain is arranged in a way that enhances the pathway strengths. This allows the use of strong pathways to transfer information within the edges of network in addition to the already discussed short paths, quite possibly to reduce the possibility of information distortion as it's transferred between nodes.

Clustering coefficient distributions, shown in Figure 5-11, indicate that the brain networks display a high level of clustering, ranging from 0.4 to about 1, across all thresholds. The nodes with the highest clustering coefficient across all thresholds were the L transverse temporal cortex and the L banks of the superior temporal sulcus, with mean values all above 0.95 at all thresholds. Average clustering coefficient values of the entire network are shown in Table 5-3, ranging from 0.74 to 0.63, while null hypothesis results show means varying from 0.66 to 0.39. As the threshold increases, the brain network displays a higher clustered organization than that observed in the null hypothesis. In other words, the brain is arranged to allow enhanced communication between communities of nodes (i.e. nodes sharing similar neighbors). The advantage of high clustering is to allow regions that work together processing information, to achieve faster results by being able to send and receive information directly to the regions involved in the processing to achieve a function.

The distribution of the weighted clustering coefficients shows an interesting result that is not present in the binary clustering coefficient distribution— it displays a slower

than exponential decay at all thresholds, similarly to the degree distribution of scale free networks. In the clustering coefficient distributions, a few nodes are observed with a very high level of clustering for both weighted clustering coefficients. Using the clustering coefficient of Equation 5-4 (c_o) the most clustered nodes were found to be the L transverse temporal cortex, banks of the superior temporal sulcus and R transverse temporal cortex respectively. At the highest graph density the banks of the superior temporal sulcus becomes the third more clustered node while R transverse temporal cortex becomes the second. On the other hand, using the clustering coefficient of Equation 5-5(c_z) the most clustered nodes are L and R banks of the superior temporal sulcus and the parahippocampal gyrus, across all thresholds. Average weighted clustering coefficients of the entire network can be seen in Table 5-4, ranging from 4.42×10^{-3} to 10.1×10^{-3} using $c_{g,o}$ and 5.25×10^{-3} using $c_{g,z}$ at all thresholds. Table 5-4 also shows the null hypothesis results, which display significantly smaller clustering coefficients than those in the brain network. The null hypothesis $c_{g,o}$ results range from 1.04×10^{-3} to 2.81×10^{-3} , and $c_{g,z}$ at all thresholds is 1.82×10^{-3} . As expected the brain displayed high clustering with weighted measures compared to null hypothesis networks. The high clustering suggests that the brain is not a random network and that it follows principles of advanced network structures (Watts and Strogatz, 1998). The clustering coefficient, $c_{g,z}$, displayed little variation in its distribution as thresholds were changed, similarly to node strength and the weighted connectivity matrix. From these results one can reason that thresholds are not critical to construct weighted networks, since differences from the null hypothesis are obtained in all graph densities.

Finally, the ratio, λ , of the brain network mean path length to null hypothesis mean path length, and the ratio, γ , of the brain network mean clustering coefficient to the null hypothesis mean clustering coefficient are shown in Table 5-5. As expected, the binary network displayed $\gamma > 1$ and $\lambda \sim 1$ yielding $sw > 1$. This demonstrates the small world property discussed in literature (Humphries and Gurney, 2008). The weighted approach also displayed $\gamma > 1$ and $\lambda \sim 1$ yielding $sw > 1$, which shows the small world property for the first time while employing a weighted network approach. The addition of weighting (an extra degree of freedom) did not affect the measured topological small world traits of brain networks, which further supports the idea that the brain is organized as a small world and not as a scale free network. The structural networks follow a physical topology, indicating that the connectivity of every node is limited by some physical parameter. In the case of structural brain networks described here, the limiting parameter is the surface area of the nodes. The scale free property implies an extremely large connectivity for some nodes, but this is unrealistic for nodes limited in the capacity to make connections. The binary networks did not display small world topology in dense networks, due to the high density of edges in the graph. However, weighted networks displayed small world topology at all thresholds, suggesting that the small world property is an inherent property of the brain (when weighted) and not just for sparse networks only. The weighing eliminates the restriction that networks should be sparse to determine the topological organization of brain networks; in doing so the thresholds are not necessary to determine the topological traits of brain networks.

5.5. Discussion

In order to increase the ability to have reproducible edges and edge weights, a high seed density is used (Cheng et al., 2012b). The large number of seeds per voxel (125) increases the possibilities of spurious connections and a high density of edges on the brain networks. In order to cope with this, the edge weight from Chapter 4 is used to ensure that the streamlines that connect the nodes meet the criteria for connectivity discussed in Chapter 4. The results presented here support the idea that sparse graphs in binary networks display a clearer small world organization than dense networks (Humphries and Gurney, 2008). However, a more rigorous study of fiber tracking results and their effect on the network density might answer the question of whether the real brain networks displays low-density of edges, or if the real topology of brain networks (those derived from tractography) includes a high-density of connections as reported here. As shown in Figure 5-4, the degree variability across the ten networks is less than 15% for most nodes, while the node strength of most nodes variation is less than 10% (see Figure 5-6). Utilizing a weighted approach reduces the variability in the average connectivity parameter for each node (i.e. degree vs node strength) as thresholds are changed (Figure 5-4 and 5-6). Another advantage of analyzing weighting networks can be seen in the node strength across thresholds (Table 5-2), where the same values of node strength is observed for graphs of high density (50% for 0 threshold) and low density (30% for 125 threshold). By removing the edges with a low number of streamlines, the analysis neglects the low edge weights, which only have values in the order of 10^{-6} , and are insignificant when compared to the bulk of the edges in the network, which are in the order of 10^{-3} . In other words, the thresholding in weighted networks eliminates edge weights that are 100 to 1000 orders of magnitude smaller

than the majority of edges of the network. In the binary approach, since all edges are given the same relevance, thresholding becomes a concern because the goal is to eliminate spurious and artifactual streamlines, and the threshold would be the only reasonable approach to eliminate the undesired connections that affect the network measures. In node strength calculations, edges with small edge weight values (compared with the mean edge weight values of the studied network) contribute minimally to the final result, so the elimination of these edges will not significantly affect the node strength calculations (Figure 5-6). Also, the visual representation of the adjacency matrix (Figure 5-8) favors employing the weighted approach since thresholding does not provide a significant contrast, in weighted matrices, with varying thresholds. The removed edges have edge weights on the order of 10^{-5} and the largest edge weight in the network is on the order of 10^{-2} . Removing weak edges corresponds to a reduction in the connectivity matrix on average, of less than 0.1%. In other words substituting a value 10^{-5} by zero in a network where the highest edge weight is the order of 10^{-2} does not affect substantially the visual appearance of the weighted connectivity matrix (Figure 5-8). The binary network shows how the thresholding changes the overall visual features of the adjacency matrix, while the weighted matrices did not display this apparent behavior. The removed edges and edge weights are shown in Figure 5-14. These plots show the differences as thresholds are increased; in the weighted matrix the differences are negligible while in the binary matrix they are not. The weighted differences are scaled by the largest edge weight removed; if the highest edge weight in the network would have been used to scale it, these plots would appear as white (i.e. no differences). Another advantage of weighting is that it easily distinguishes highly

weighted nodes and the important nodes connecting the hemispheres of the brain (the top right and bottom left quadrants). Only a handful of nodes show a significant edge weight value in Figure 5-8, while the binary matrices show a high density of edges. These nodes (red points in Figure 5-8) are main anatomical domains that allow the inter-hemispheric transfer of information. In the binary adjacency matrix this information is lost due to the equivalency of the edges of the network.

The binary and weighted approaches did not show the same nodes with the highest values of degree and node strength, which is easily explained by the emphasis of each approach. The superior parietal and frontal cortexes displayed the largest node degree values; these are fairly big nodes that have ample spatial occupancy within the brain to create connections to all other nodes in the network (largest bars in Figure 5-4). Also, these are association areas with multiple connections to and from primary cortexes of the parietal and frontal cortexes respectively. On the other hand, the node strength displayed high values for the insula, the caudal anterior and posterior cingulate (largest bars in Figure 5-6, anatomical locations in Figure 5-14); these are nodes with connections through the corpus callosum, which is the largest tract in the human brain. These nodes with large node strength also contain large projections to subcortical regions that in the weighted approach appear as strong edges connecting to other cortical regions.

The brain networks were also found to be highly clustered as expected (Hagmann et al., 2007), see Figure 5-11 and Table 5-3. However, as previously described for binary metrics, the binary clustering coefficient is also highly susceptible to thresholding. The weighted clustering coefficients displayed small variation across

thresholding (Figure 5-12, 5-13 and Table 5-4), similar to the node strengths. The clustering coefficient described by Zhang (Equation 5-5) displayed a higher resilience to thresholding than that described by Onnela (Equation 5-4). This might be a direct result of Onnela's normalization of the clustering coefficient by the node degree, k , which is binary measure, while Zhang's is entirely a weighted description of clustering. The weighted approach also shows a slow decay in the log-linear plots of Figures 5-12 and 5-13, suggesting power law decay in the weighted clustering coefficient, and a small collection of strongly clustered nodes. The banks of the superior temporal sulcus and the transverse temporal cortex displayed high clustering coefficients values.

Anatomically these two regions serve as intermediary nodes of connected regions: the superior temporal gyrus from the middle temporal gyrus and the primary auditory regions, respectively. The parahippocampal gyrus resulted in a highly clustered node employing Zhang's clustering coefficient (Equation 5-5). Anatomically, this is a region surrounding the hippocampus which also connects to perirhinal and entorhinal cortex. These highly clustered regions serve as intermediaries to the brain functions associated with the aforementioned areas. The weighted clustering coefficient displayed a larger robustness than the binary clustering coefficient as thresholds are changed. This is similar to the node strength argument that "weak" edges only minimally contribute to the overall measure. The elimination of these edges does not significantly affect the obtained results at high or low graph densities.

The binary path length was found to be "short" as predicted in references (Hagmann et al., 2007). Thresholding increased the average path length, by virtue of removing weak edges that serve as extra shortcuts in dense graphs. The weighted path

length was the weighted metric most susceptible to changes as the threshold was changed, as shown in Figure 5-10. With the binary approach, the brain network showed a higher average path length than the null hypothesis results. On the other hand, the weighted approach exhibits lower average weighted path lengths in the brain network than in the null hypothesis network. Higher values of the weighted path length should not be seen as an increase in path length. Instead, they should be interpreted as greater strength of the path. In binary networks, random organization leads to effective paths between nodes (i.e. short distances between nodes). In the weighted approach, random organization also shows effective paths between any two nodes by displaying strong path lengths (i.e. high weighted path length values). The thresholding eliminates weak paths, which have small weights throughout the pathway. These weak paths have not been given any attention in brain network studies. This in part is due to the thresholding used to remove them to be able to estimate topological properties of brain networks. Nonetheless to estimate these weak ties, high seed densities in tractography are necessary. Granovetter argued that weak ties are extremely important in social networks, since it allows for the shorter path lengths observed in social interactions (Granovetter, 1973). The same reasoning can be applied to brain networks, in that the brain is organized in a dense mesh of nodes with a high number of edges that show an intricate web of connections, weak and strong, providing a very stable network that is very robust to random errors or attacks. Although sparse graphs improve our ability to determine their topological traits, it could be possible that real networks might not be sparse yet strict organizational features (small world or scale free) are still true. A node with a large degree value implies that the nodes are connected through one edge to

many other nodes, yielding low path length values. Hence, binary networks with high graph density will display what would seemingly be small world property (i.e. high clustering and short path lengths) largely in part by virtue of high connectivity.

In weighted networks, nodes with the strongest weighted path length values were highly affected by thresholding (Figure 5-10). Thresholding removes direct “weak” connections between any two nodes; as the threshold is increased, weak and short path lengths are replaced with longer and stronger path lengths. For example, as the threshold is applied, if the resulting network is connected, then a “weak” direct (low edge weight value) connection between any two nodes will be replaced by at least two edges with “stronger” connections (larger edge weight values) than the original edge weight. Consequently the new weighted path length will be significantly larger than the original “weak” connection.

In the binary and weighted approaches the small world property in brain networks was determined, as seen in Table 5-5. The binary network’s small worldness parameter increased with a decrease in the density of edges, as expected, and the “small” small worldness parameter in the binary unthresholded network is due to the high density of edges in the network, ~50%. It comes as no surprise that the null hypothesis network displayed small path length, but a high clustering was not expected. As the edge density was high, the odds that the neighbors of any node were connected were high as well, so the high clustering observed in the non-thresholded null hypothesis network is a result of edge density and not of small world organization. Another advantage of weighted networks can be seen in the displayed ranges of small worldness parameter, sw , in Table 5-5. While binary networks only showed 1.53 for a thresholded network of

125, the weighted approach displays values of 5.13 and 4.10 for c_0 and c_z respectively. Therefore, a sharper small worldness organization is displayed in weighted networks.

5.6. Concluding Remarks

In multiple reports using a binary connectivity framework, the brain network structure has been described as a small world network, which is dependent on the edge density and the number of nodes (Bassett et al., 2011b; Hagmann et al., 2007; He et al., 2009). The weighted connectivity approach provides a more stable framework to study brain networks, since it adds a degree of freedom in the form of the edge strength. It also provides an improved way to visualize the hubs and the inter-hemispheric brain connectivity using just a simple display of the weighted adjacency matrix. Although all binary metrics (degree, path length and clustering coefficient) were stable when compared across acquisitions, when a comparison across thresholds (for all acquisitions) was made, they varied significantly with graph density. The use of a weighted network preserves the characteristic of small world organization and makes it easier to determine brain topology. Observe that the range of small worldness (high clustering and short path length) values in weighted networks was higher when compared to the binary networks and the node strength distribution did not display power law decay associated with scale free networks. Thresholds have significantly less effect on the small worldness values in weighted networks (8% for c_z and 7% for c_0 , Table 5-5) compared to the binary networks (28%, Table 5-5). The weighted network approach provides higher connectivity values (strengths) when big pathways (like the corpus callosum) connect the nodes, while the binary approach favors regions of large volumes that contain multiple projections to other nodes. In binary brain networks,

nodes with large volumes will have many connections, even weak ones (i.e. small edge weights); hence nodes will appear more connected (i.e. high degree), while in the weighted networks, nodes with big white matter tracts associated to them will appear more connected (i.e. high node strength). The major contributors to network variation in both binary and weighted networks will be; volume averaging (due to limited spatial resolution), subject variability, and node definition. Node definition is made carefully to reduce its effect on calculated network parameters. Subject variability is the main source to estimate differences in populations. Thresholding is commonly used to mitigate the effects of artifactual streamlines due to volume averaging. However, thresholding is an arbitrary procedure and the results of this chapter (Table 5) show that thresholding is unnecessary to study weighted networks. Therefore weighted networks reduce the number of possible sources of variation by one, by eliminating the need to threshold the brain networks derived from tractography, improving the ability to obtain a more realistic characterization of brain networks.

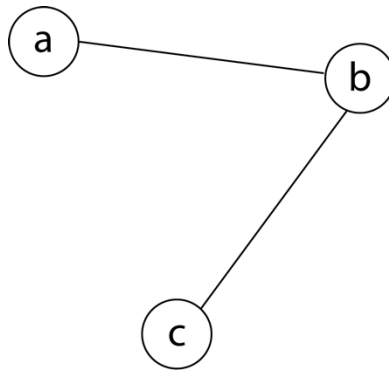


Figure 5-1. Three-node network connected by two edges. The distance from node *a* to node *c*, is the sum of the distance from node *a* to *b* in addition to the distance of node *b* to *c*.

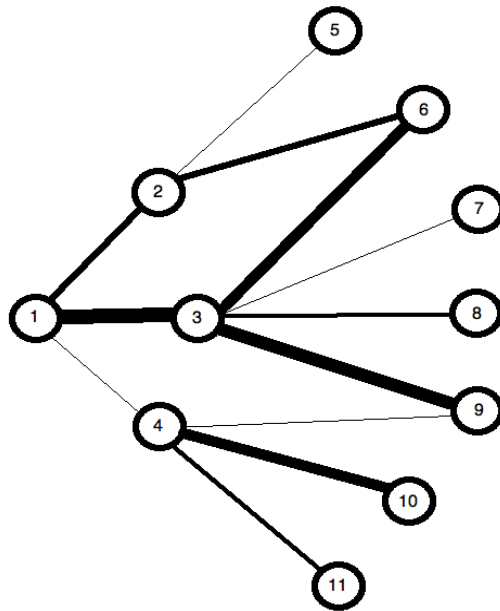


Figure 5-2. Eleven-node weighted network. Edge thickness represents the relative edge weight strength, e.g. $e_{13} > e_{14}$.

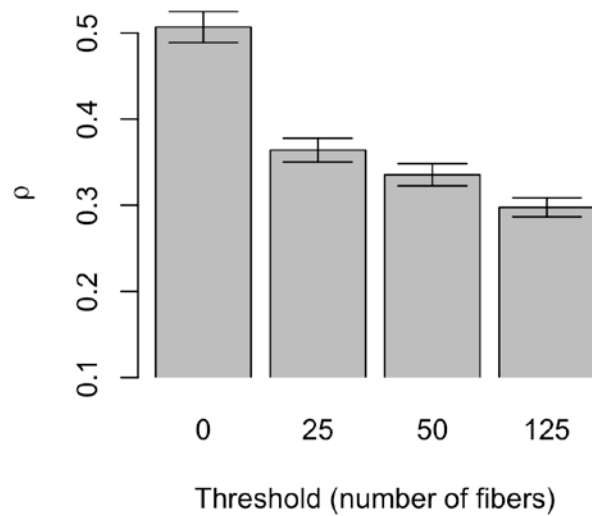


Figure 5-3. Graph density plot. Density is obtained by taking the ratio of the number of edges in a graph to the total possible number of edges in the graph. The threshold refers to the number of fibers required to remove an edge from the network. Zero refer to the unthresholded networks. Twenty five refers to networks constructed by eliminating edges made up by 25 or less fibers. Similarly for 50 and 125.

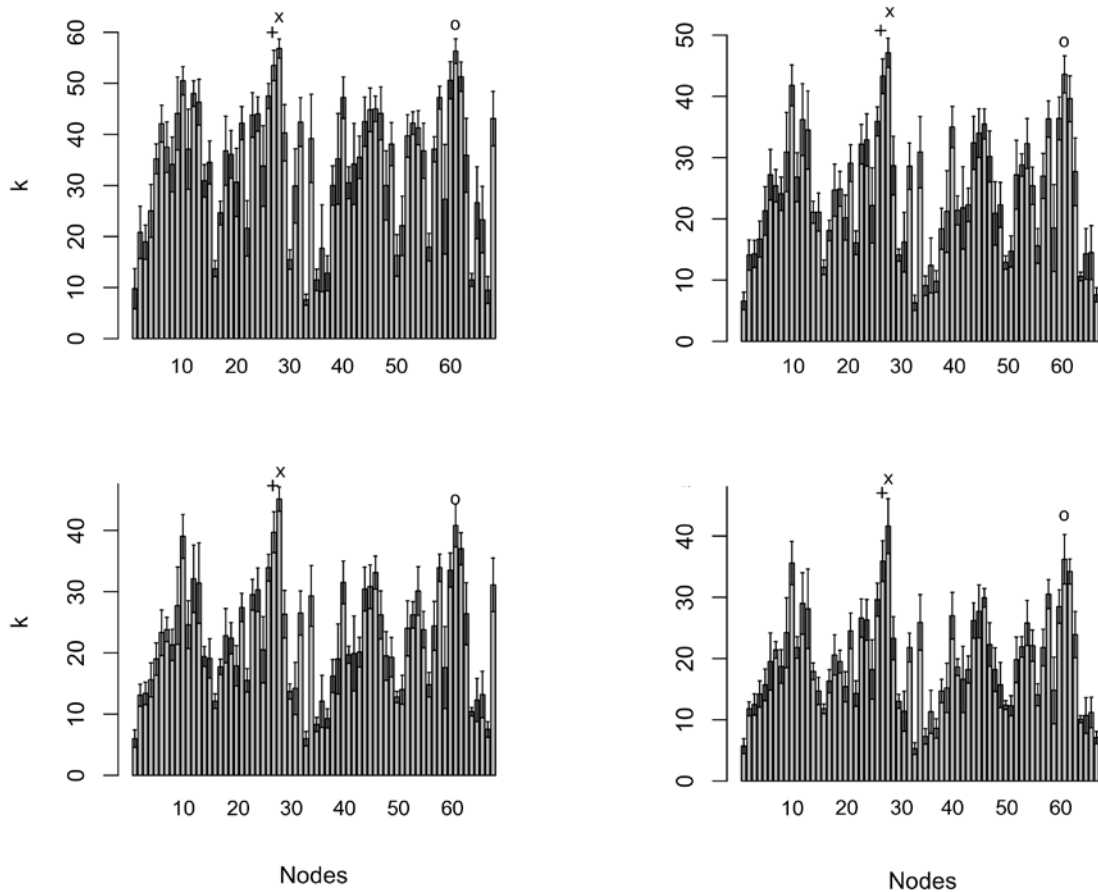


Figure 5-4. Node degree measurements. Plotted average values at different thresholds: threshold 0 (top left), 25 (top right), 50 (bottom left) and 125 (bottom right). The changes in bar heights show the reduction in degree values for each node as the threshold is changed. Note that the y-axis on the 0 threshold network ranges from 0-60 while all others range from 0-50; the axis is not kept the same to allow better visibility of the degree values at all thresholds. See Table 5-6 for the list of nodes. The marks in all plots corresponds to the three largest degree values: (x) L parietal lobe (Label 28), (o) R superior frontal cortex (Label 62), and (+) L superior frontal cortex (Label 27).

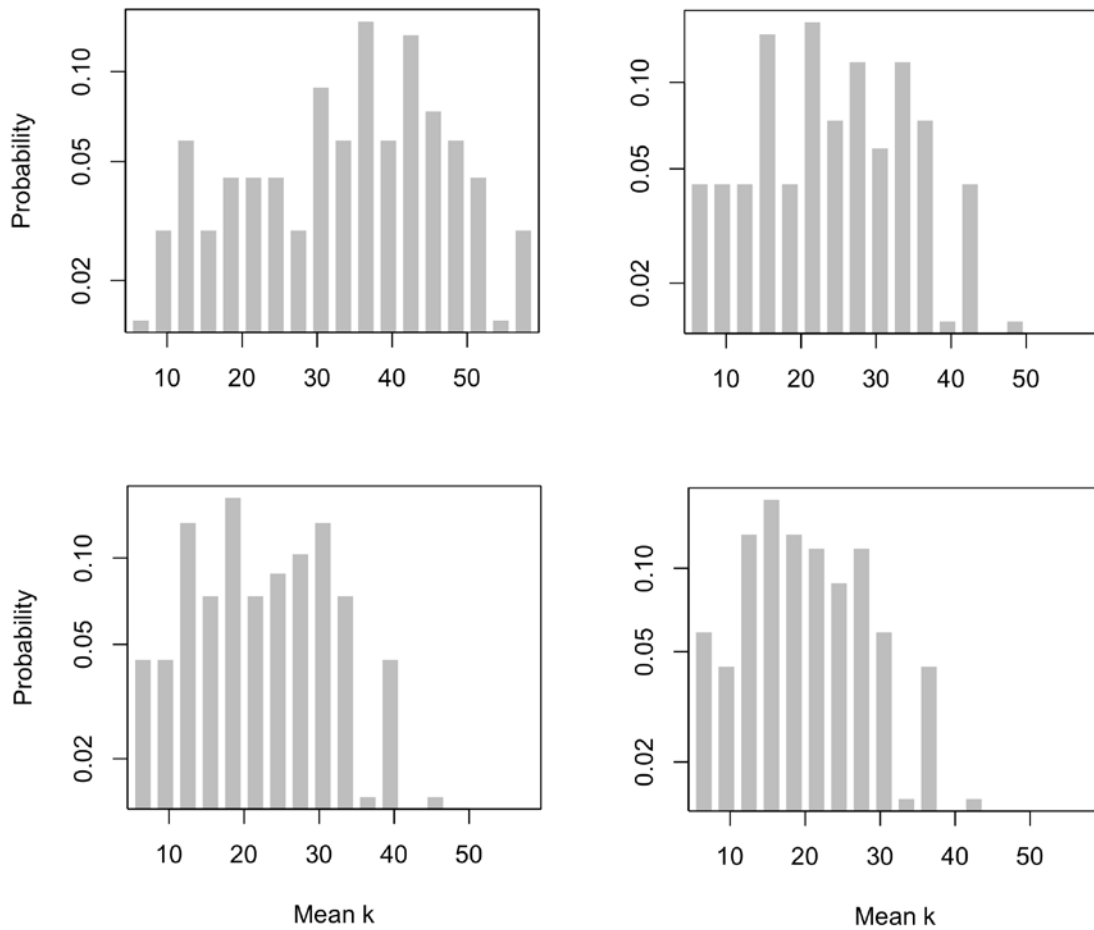


Figure 5-5. Node degree distribution in log-linear scale. Plot threshold 0 (top left), 25 (top right), 50 (bottom left) and 125 (bottom right). The degree distributions are shifted towards lower degree values as the thresholds are increased.

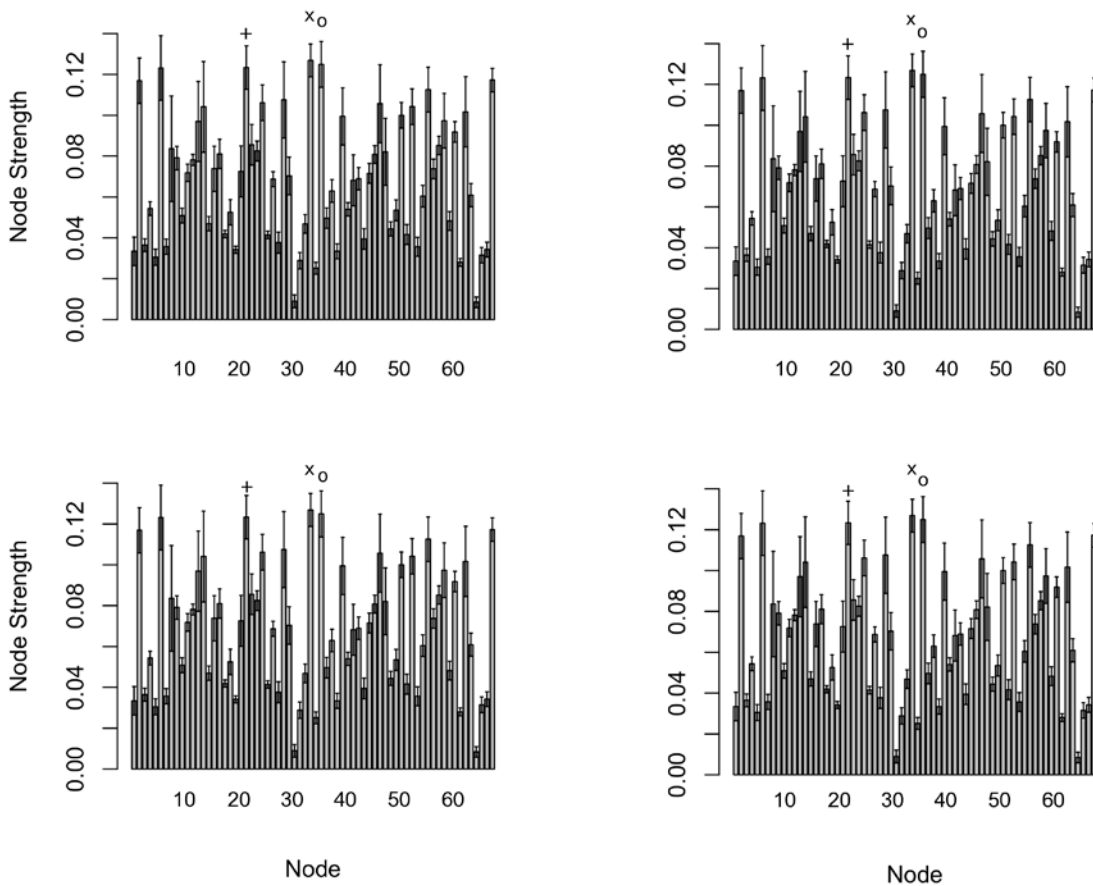


Figure 5-6. Node strength values. Plotted average values at different thresholds threshold 0 (top left), 25 (top right), 50 (bottom left) and 125 (bottom right). See Table 5-6 for the list of nodes. The brain networks displayed a reduction in the number of edges as the threshold was changed inducing a change in the degree values (Figure 5-4), conversely the node strength do not show this evident change in the average values for all nodes since it is in the order of less than 0.24%. The marks in all plots corresponds to the three largest node strengths: (x) L insula (Label 34), (o) L caudal anterior cingulate (Label 36), and (+) L posterior cingulate (Label 22).

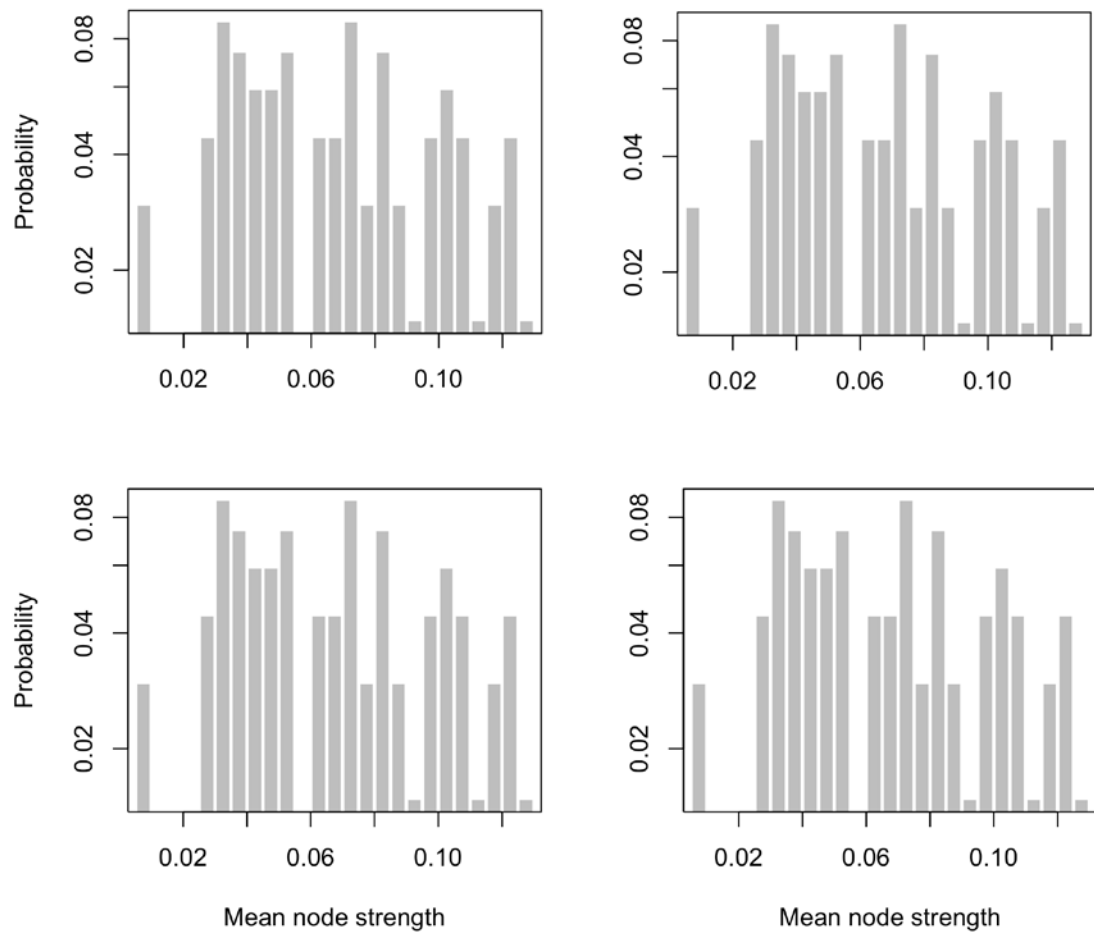


Figure 5-7. Node strength distribution in log-linear scale. Plot threshold 0 (top left), 25 (top right), 50 (bottom left) and 125 (bottom right). Similar distributions at all thresholds suggest that the removal of weak edges only modifies minimally the node strengths obtained from network constructed at different thresholds.

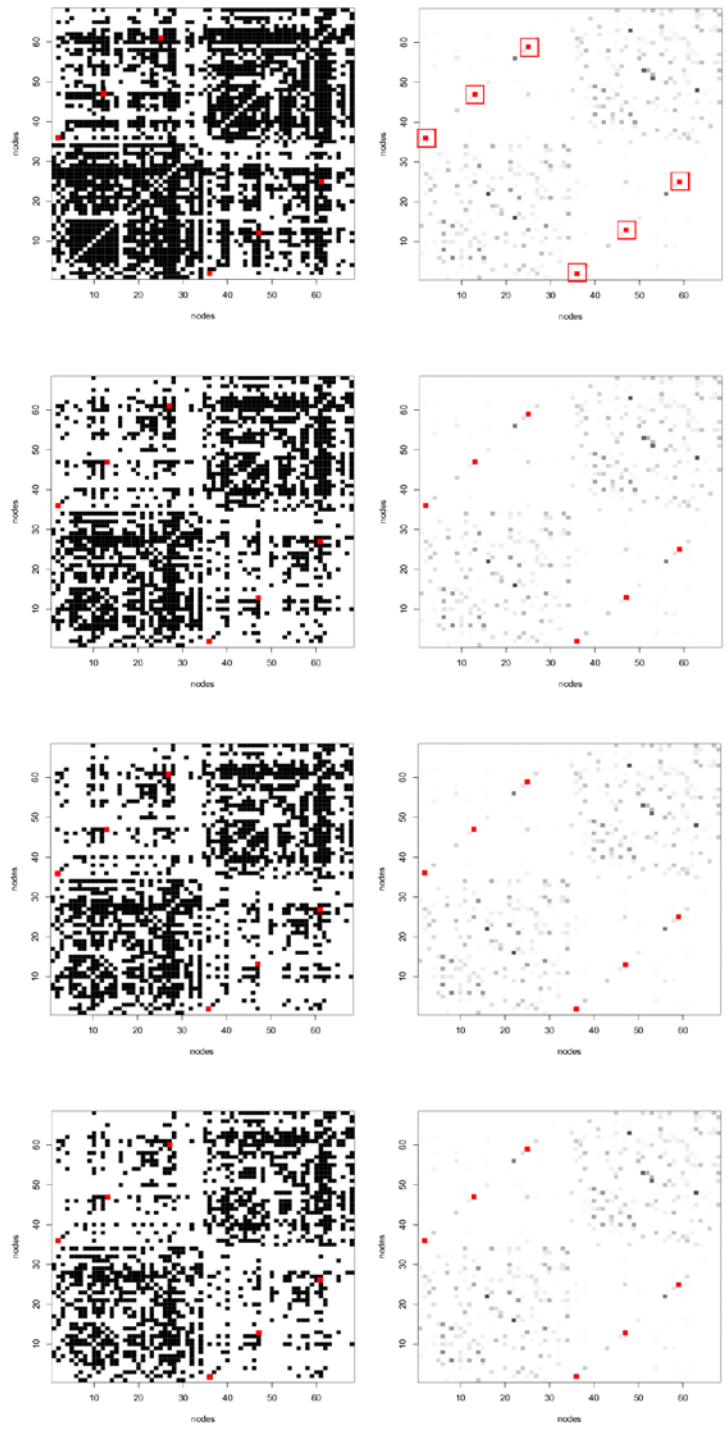


Figure 5-8. Representative binary and weighted adjacency matrices. Binary plots on the left and weighted plots right; thresholds at 0,25,50 and 125 from top to bottom. The binary matrices display stark differences as the threshold is increased, while weighted matrices seem exact replicas of each other. The red points corresponds to the larger edge weights in the entire network and anatomically these are inter-hemispheric connections traversing left-right in the brain.

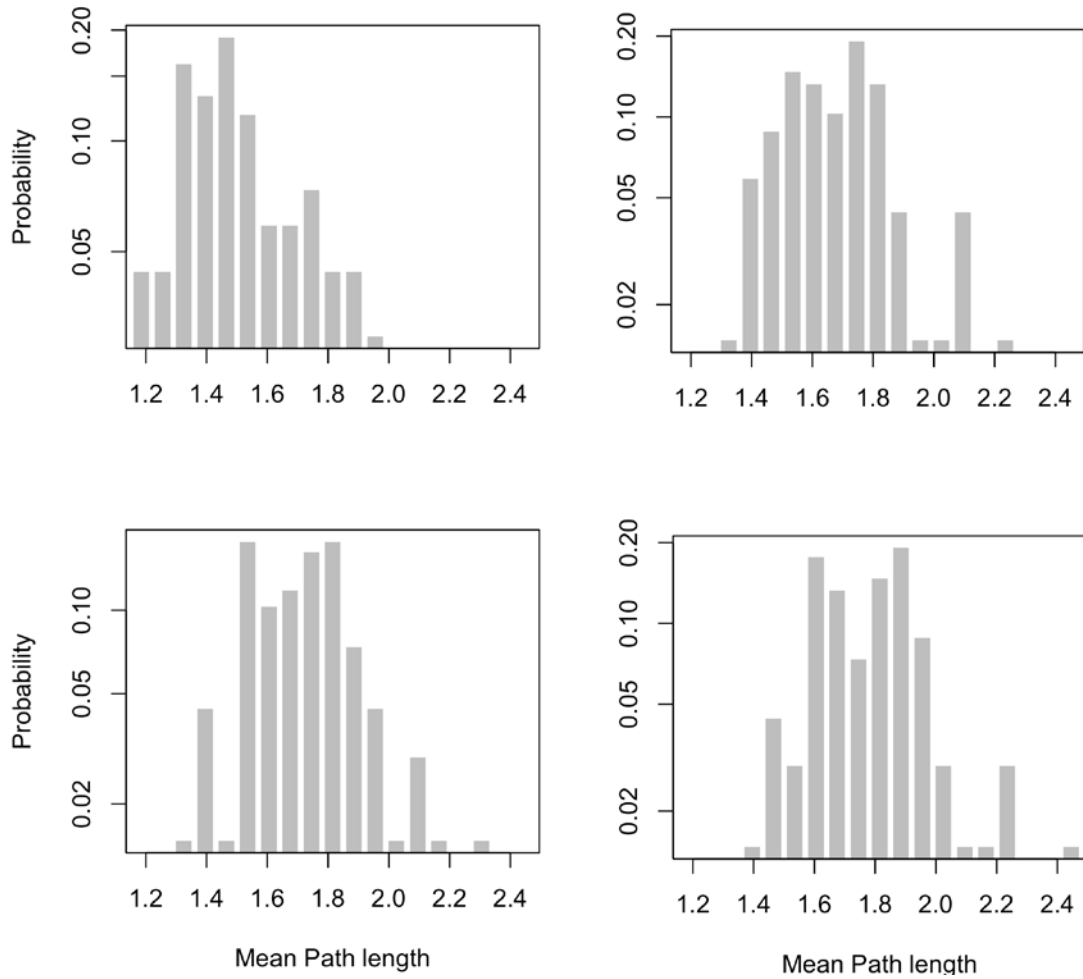


Figure 5-9. Average binary path length distribution in log-linear scale. Plot threshold 0 (top left), 25 (top right), 50 (bottom left) and 125 (bottom right). As thresholds are increased the greater part of the distribution shift to larger path lengths, since shortcuts (“weak” edges) are removed from the network.

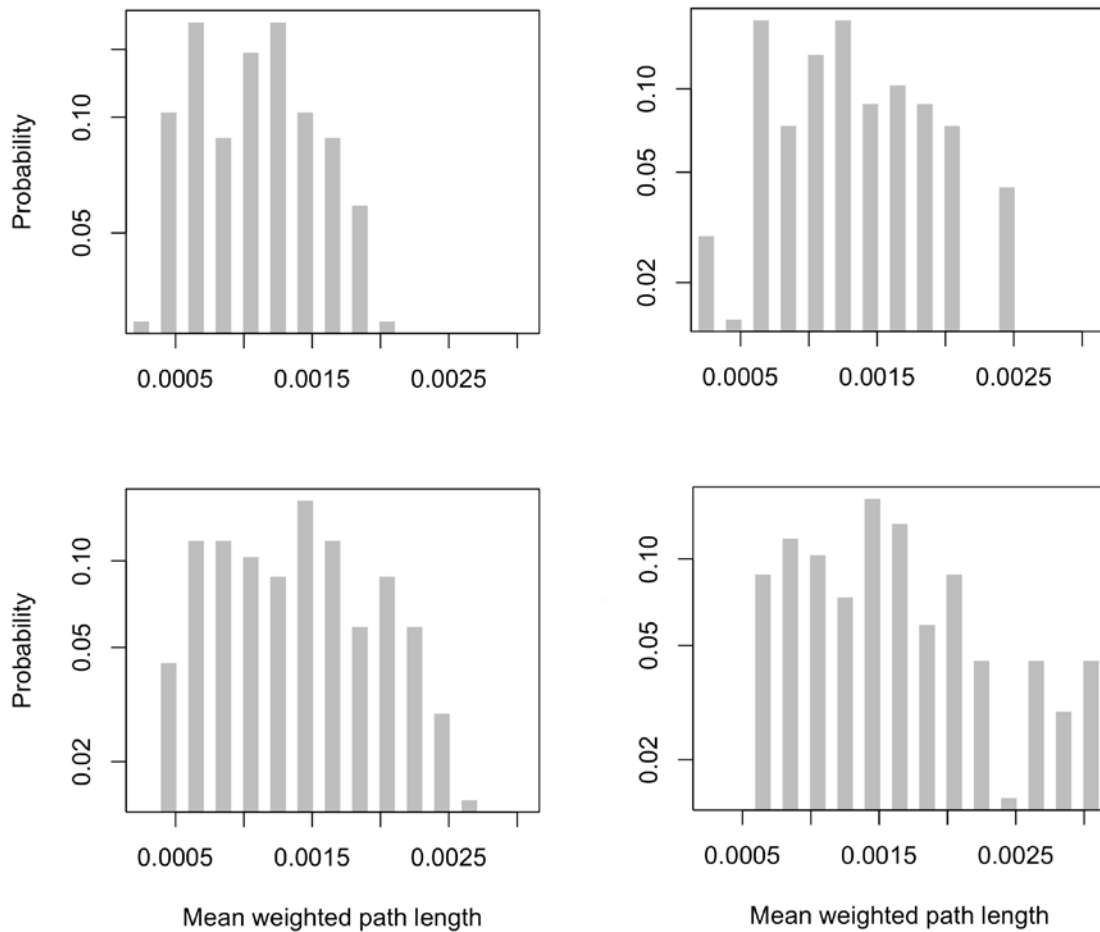


Figure 5-10. Average weighted path length distribution in log-linear scale. Plot threshold 0 (top left), 25 (top right), 50 (bottom left) and 125 (bottom right). As thresholds are increased the greater part of the distribution shift to stronger path lengths, since shortcuts (“weak” edges) are replaced with longer paths. The new paths will be two or more steps longer than the original “weak” path. Each edge that makes up the new path will have a larger edge weight than the original path, hence moving the distribution to stronger path lengths.

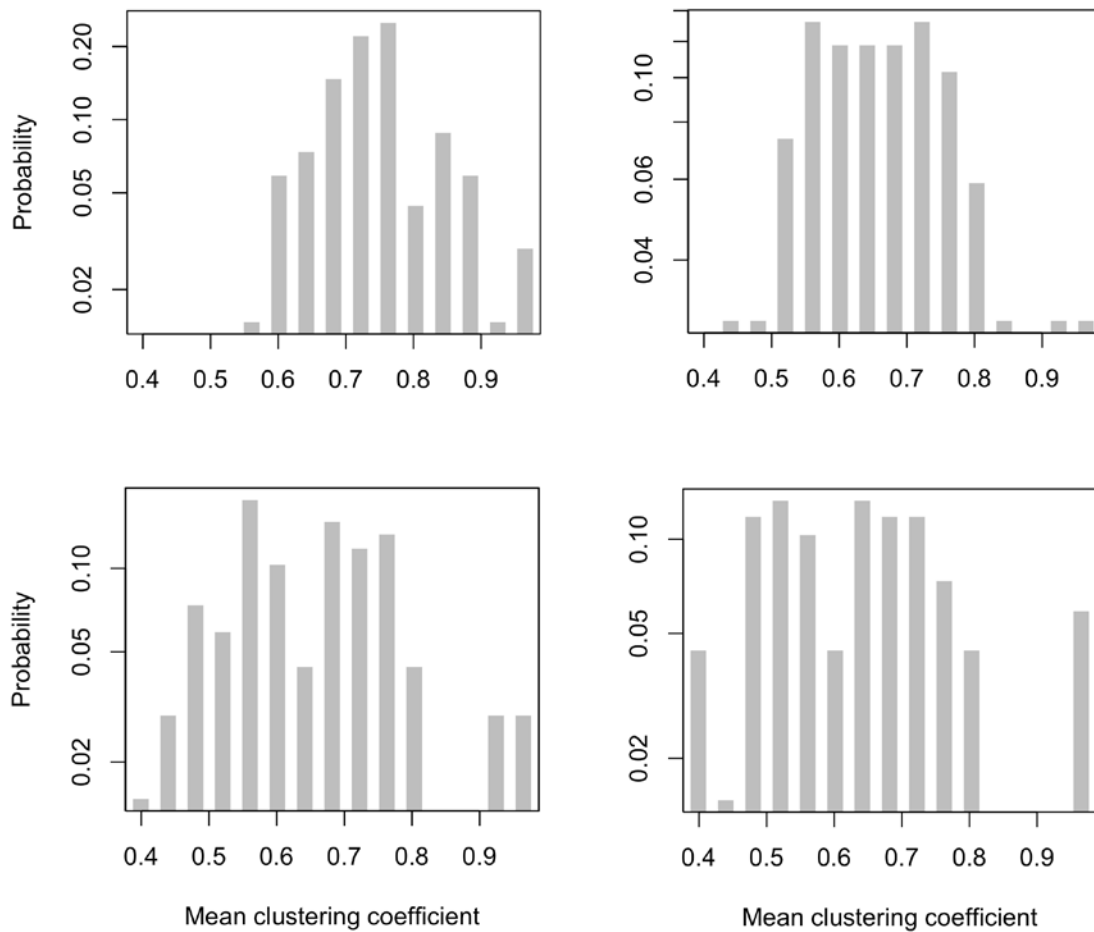


Figure 5-11. Binary clustering coefficient distribution in log-linear scale. Plot threshold 0 (top left), 25 (top right), 50 (bottom left) and 125 (bottom right). These plots show that as the threshold is increased the clustering coefficient distribution broadens. This implies that as “weak” edges are removed some nodes loses the strength of the communities around it but the overall the network still displays high values of clustering for most nodes (compared to null hypothesis networks, Table 5-3).

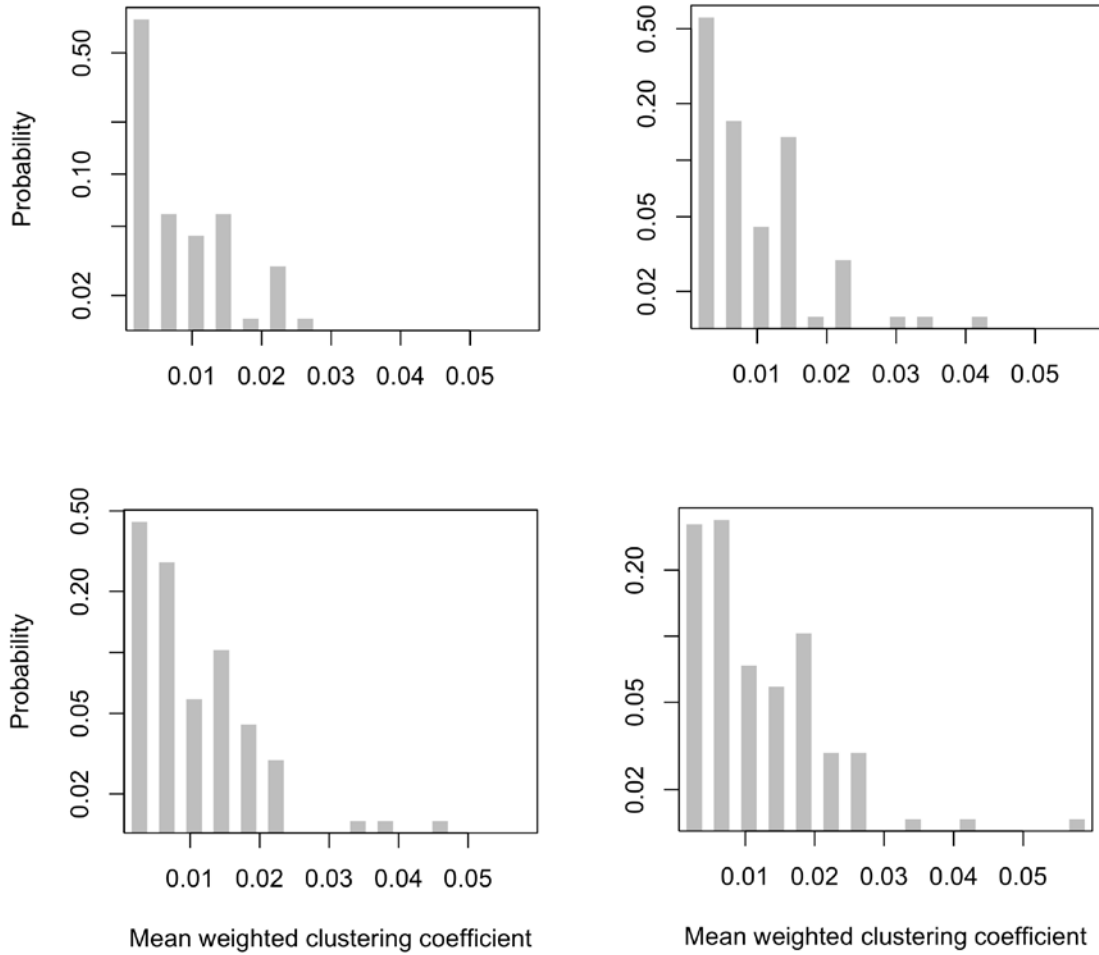


Figure 5-12. Weighted clustering coefficient (Equation 5-4) distribution in log-linear scale. Plot threshold 0 (top left), 25 (top right), 50 (bottom left) and 125 (bottom right). Slight variations in the distributions can be observed as the threshold is change however the overall trend is maintained. The variation could be attributed to using a binary metric (degree) in this weighted measure.

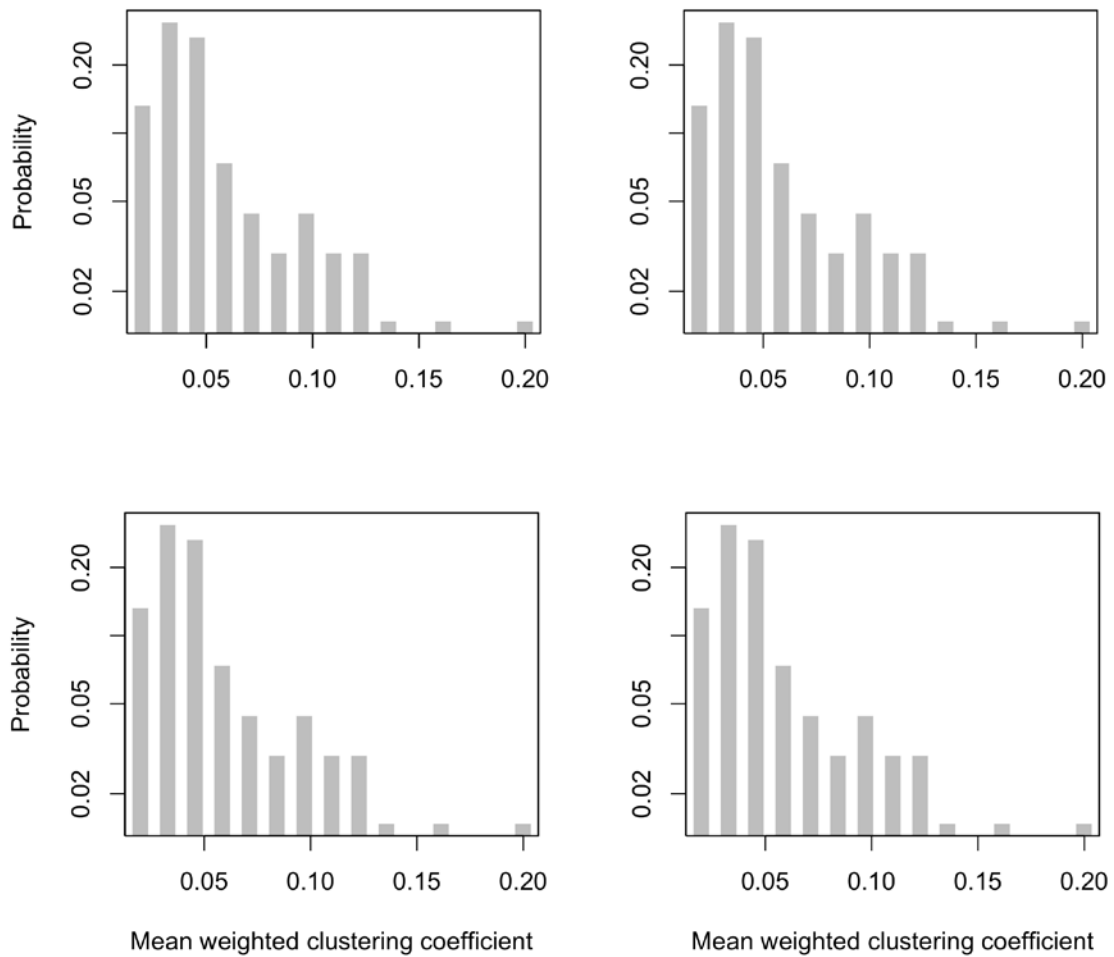


Figure 5-13. Weighted clustering coefficient (Equation 5-5) distribution in log-linear scale. Plot threshold 0 (top left), 25 (top right), 50 (bottom left) and 125 (bottom right). The clustering coefficient distributions seem to be replicas of each other as the threshold is changed, similar to the node strength and weighted connectivity matrices.

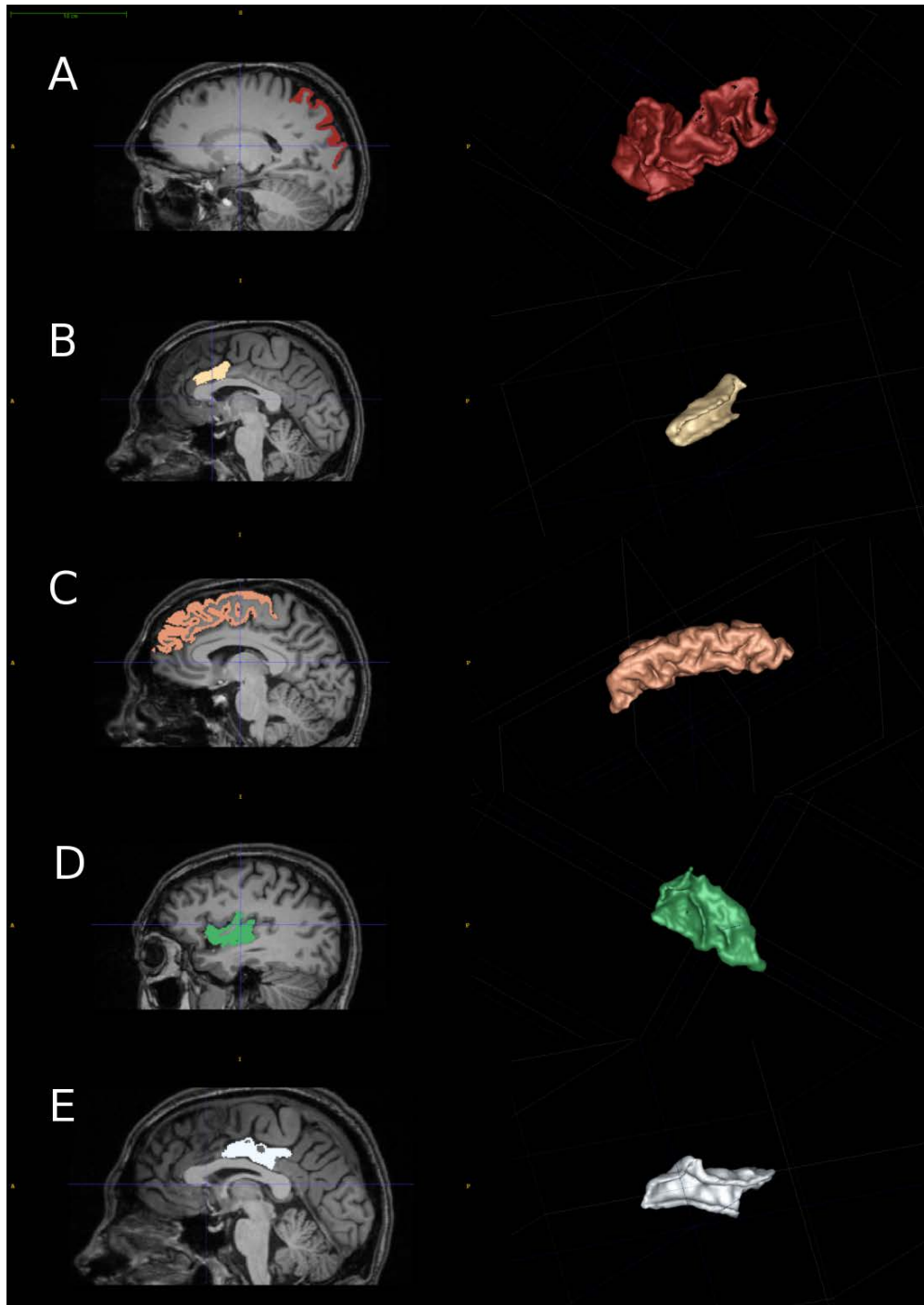


Figure 5-14. Anatomical location of human nodes. A) Superior parietal cortex, node with high degree value. B) Caudal anterior cingulate, node with high node strength value. C) Frontal cortex, node with high degree value. D) Insula, node with high node strength value. E) Posterior cingulate, node with high node strength value.

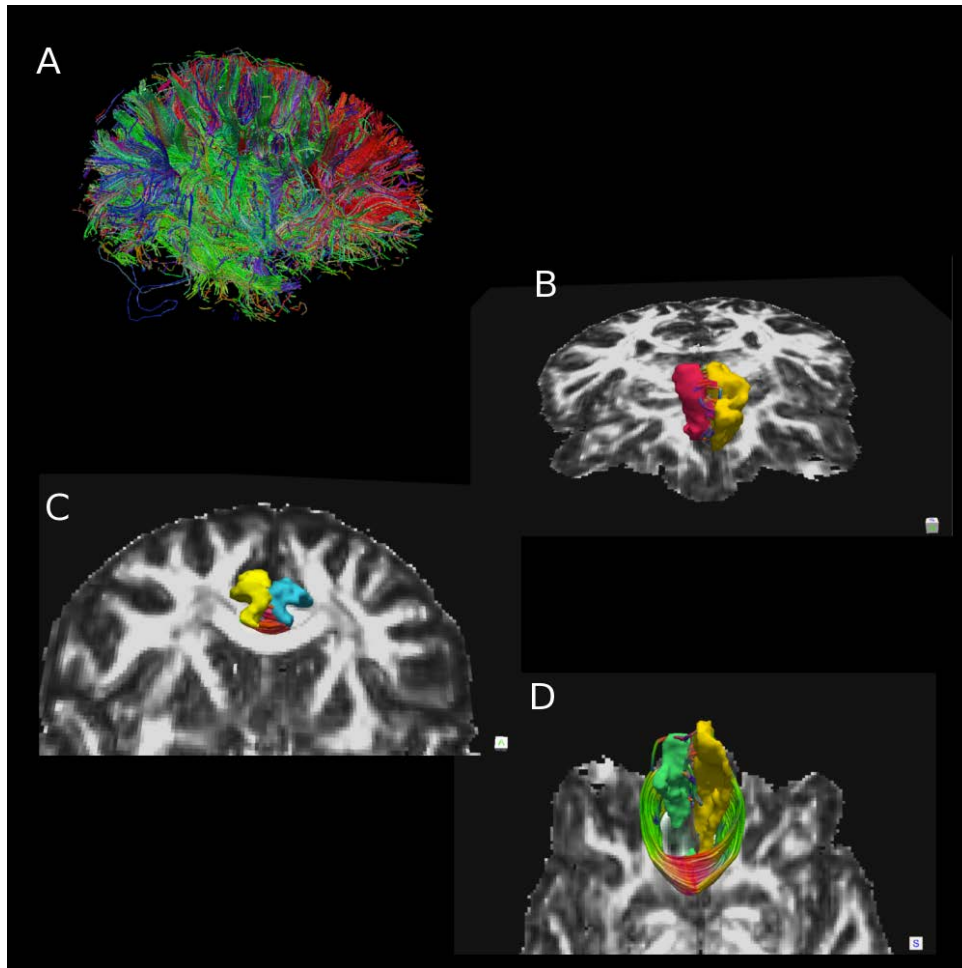


Figure 5-15. Streamlines connecting nodes. A) Whole brain tractography map.
 B) Streamlines connecting the left and right rostral anterior cingulate.
 C) Streamlines connecting the left and right caudal anterior cingulate.
 D) Streamlines connecting the left and right medial orbito-frontal cortex.

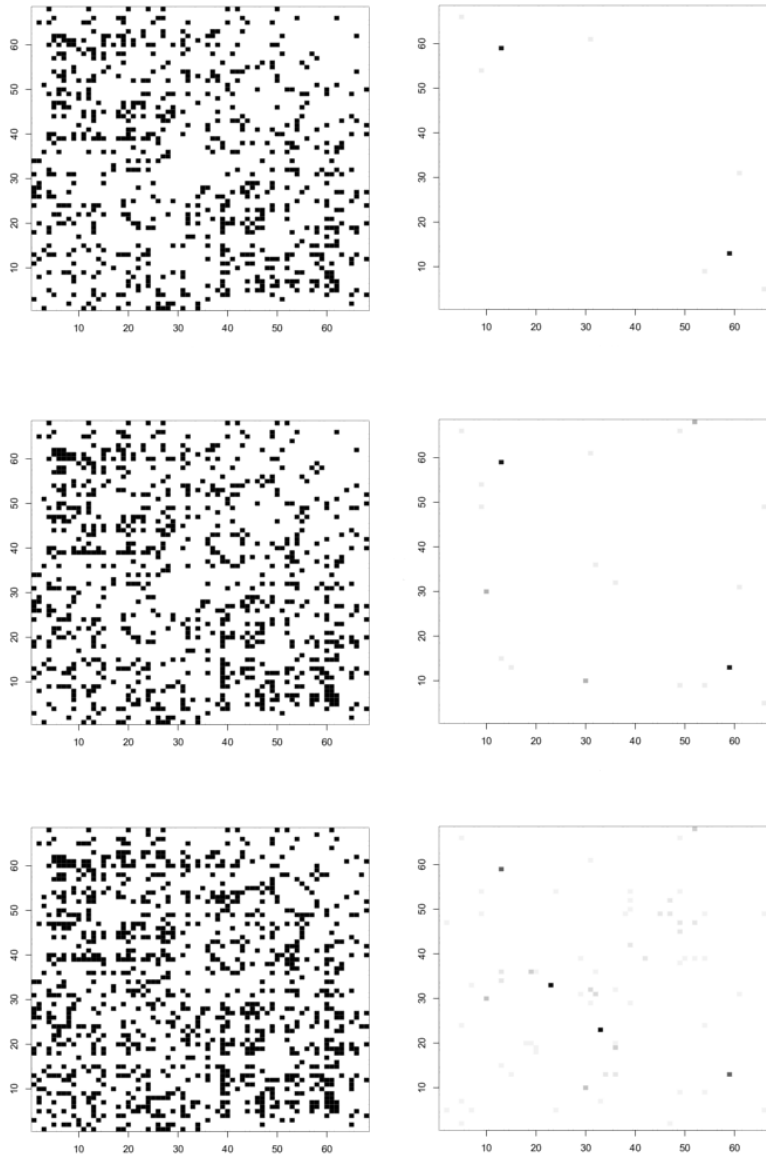


Figure 5-16. Differences in binary and weighted matrices. Left column shows the binary matrix changes as edges are removed with increasing threshold. Right column shows the weighted differences. Top row shows the difference between the unthresholded (0-threshold) and threshold of 25 streamlines or more (25-threshold). Middle row shows the difference between 0-threshold and 50-threshold. Bottom row shows difference between 0-threshold and 125-threshold.

Table 5-1. Average node degree (\hat{k}) values (Equation 2-17) and standard deviation (σ).
The values were averaged across the ten networks.

Threshold	\hat{k}	σ
0	36.0	4.49
25	24.4	3.49
50	21.9	3.14
125	19.1	2.81

Table 5-2. Average node strength (\hat{s}) values (Equation 5-2) and standard deviation (σ).
The values were averaged across the ten networks.

Threshold	\hat{s} (10^{-2})	σ (10^{-3})
0	6.88	7.40
25	6.88	7.40
50	6.88	7.40
125	6.88	7.40

Table 5-3. Binary path length and clustering coefficient metrics. The values were averaged across the ten networks.

Threshold	l_g	l_N	$C_{B,g}$	$C_{B,N}$
0	1.51	1.50	0.74	0.66
25	1.68	1.64	0.67	0.48
50	1.72	1.67	0.65	0.44
125	1.79	1.72	0.63	0.39

Table 5-4. Weighted path length (Equation 5-3) and clustering coefficient (Equation 5-4 and 5-5) metrics. The values were averaged across the ten networks.

Threshold	$l'_g(10^{-3})$	$l'_N(10^{-3})$	$c_{O,g}(10^{-3})$	$c_{O,N}(10^{-3})$	$c_{Z,g}(10^{-2})$	$c_{Z,N}(10^{-2})$
0	1.08	1.40	4.42	1.04	5.25	1.82
25	1.28	1.65	7.51	1.96	5.25	1.82
50	1.37	1.89	8.46	2.30	5.25	1.82
125	1.57	2.23	10.1	2.81	5.25	1.82

Table 5-5. Small worldness of weighted and binary networks (Equations 5-7 through 5-9). The γ and λ parameters were calculated from Tables 5-3 and 5-4.

Threshold	Binary			Weighted (c_O)			Weighted (c_Z)		
	γ	λ	sw	γ	λ	sw	γ	λ	sw
0	1.13	1.01	1.12	4.24	0.77	5.51	2.89	0.77	3.76
25	1.39	1.02	1.36	3.84	0.78	4.95	2.89	0.78	3.72
50	1.47	1.03	1.43	3.68	0.73	5.08	2.89	0.73	3.99
125	1.60	1.04	1.53	3.61	0.70	5.13	2.89	0.70	4.10

Table 5-6. Human brain network nodes. The number in both hemispheres column correspond to the node placement in Figures 5-4 and 5-6.

Hemisphere		Cortical region
Left	Right	
1	35	Banks of the superior temporal sulcus
2	36	Caudal anterior cingulate
3	37	Caudal middle frontal
4	38	Cuneus
5	39	Entorhinal
6	40	Fusiform
7	41	Inferior parietal
8	42	Inferior temporal
9	43	Isthmus cingulate
10	44	Lateral occipital
11	45	Lateral orbitofrontal
12	46	Lingual
13	47	Medial orbitofrontal
14	48	Middle temporal
15	49	Parahippocampal
16	50	Paracentral
17	51	Parsopercularis
18	52	Parsorbitalis
19	53	Parstriangularis
20	54	Pericalcarine
21	55	Postcentral
22	56	Posterior cingulate
23	57	Precentral
24	58	Precuneus
25	59	Rostral anterior cingulate
26	60	Rostral middle frontal
27	61	Superior frontal
28	62	Superior parietal
29	63	Superior temporal
30	64	Supramarginal
31	65	Frontal pole
32	66	Tempora lpole
33	67	Transverse temporal
34	68	Insula

CHAPTER 6 PATHOLOGICAL NETWORKS

6.1. Opening Remarks

The goal of this Chapter is to use the edge weight (Chapter 4) and weighted framework (Chapter 5) to study brain networks and show the favorability of weighted networks to provide additional information to differentiate control brains from thyroid disrupted (TD) networks. The thyroid hormone (TH) deficiency model is ideal since the structural changes in the brain are due to changes in WM volumes, which in turn lead to a decrease in the strength of connectivity measures.

With cocaine hypersensitivity (van der Marel et al., 2013), the rat brain has been shown to display changes in connectivity. Using DTI, van der Marel et al. were able to determine the small world organization in the rat brain using a weighted network. However, their approach employed diffusion tensor imaging (DTI), used only 10 seeds per voxel for the tractography, and weighted the network connections by FA values. A problem with this approach is that DTI fails to estimate fiber crossings and kissing, inducing errors in the connectivity map. The FA calculation is influenced by acquisition schemes (Alexander et al., 2001; Jones et al., 1999), and present a problem in WM regions where more than one fiber population crosses a voxel. In these regions, where each voxel contains multiple fibers, the obtained FA values resemble a GM region even though they are WM regions.

The results to be discussed in this chapter regarding rat brain organization support van der Marel's observation of small world organization in the rat brain. Also, this weighted framework can be used to study brain networks of rats with changes in

connectivity (Powell et al., 2012) and disconnection syndromes (Catani and Ffytche, 2005).

6.2. Methods

6.2.1. Animals Treatment

The rat treatments were performed at the University of South Florida (USF, St. Petersburg, FL) with the approval of the USF Institutional Animal Care and Use Committee (IACUC) permit #R3486. Offspring of rat dams were randomly selected and assigned for group treatments. For specific details of this procedure refer to Powell, et.al.(Powell et al., 2012). The groups in this publication are control rats (n = 5) and rats treated with 10 ppm 6-propyl-2thiouracil (n = 4) (PTU; Sigma Aldrich Corp, St. Louis, MO). Dosing began at gestation day 7 and continued until postnatal day 25. Rats were allowed to live until 90 days after birth, and were then sacrificed and perfused with phosphate-buffered saline (PBS), followed by 10% buffered formalin phosphate (Fisher Scientific Inc., Hampton, NH). Brains were removed from the skull and stored in formalin for *ex vivo* imaging. Throughout the rest of this text, rats treated with PTU will be referred to as PTU.

6.2.2. Networks

Using a digitized Paxinos atlas (Paxinos and Watson, 1998) a total of 40 rat cortical nodes (Table 6-6 for the nodes names and their appropriate label number used in the figures of this chapter) were defined. FSL's FLIRT was used to register the Paxinos atlas regions as nodes in diffusion space. Networks were constructed using the methods outlined in Chapters 4 and 5. In this Chapter for each rat brain, two networks will be created at different thresholds to estimate the organizational features of the rat

brain. The threshold will be employed to reduce the graph density and compare the topological properties of rat's brains in dense and sparse networks. Both networks will contain the same number of nodes, but the edges will be defined in the first network by having at least one fiber connecting any two nodes and the second will be with edges made up of 6000 fibers or more. These thresholds will allow the comparison of dense networks, i.e. high number of edges (~76% and ~70% of all possible edges in control and PTU networks respectively) and sparser networks (~24% and ~21% of possible edges in control and PTU networks respectively). Throughout the rest of this text, dense networks of control rats will be referred to as DeCo (**Dense Controls**), sparse networks of control rats will be referred to as SpaCo, (**Sparse Controls**), dense networks of PTU rats will be referred to as DePtu, and sparse networks of PTU rats will be referred to as SpaPtu.

6.3. Results

Null hypothesis networks allow determining whether any real-world network displays any organizational feature different from a random network. In this section the results of brain networks and null hypothesis graphs are summarized and a discussion of the results will be provided in section 6.4. As a reminder, the graph density is the number of edges present in the network divided by the total numbers of possible edges in the graph. The PTU treated rats displayed a significant reduction in average degree values in dense ($p = 5.5 \times 10^{-4}$) and sparse ($p = 1.6 \times 10^{-3}$) networks, as shown in Figure 6-1. Table 6-1 shows the average degree value of the entire network for control and PTU brains. DePtu networks displayed a reduction of high degree nodes, as shown in the degree distributions of Figure 6-2, which demonstrate a decreased connectivity on PTU brains. The TD connectivity reduction can also be observed in the large number of

small degree values (Figure 6-2) compared to the normal networks. SpaPtu networks displayed a faster decay of high degree nodes, as shown in the degree distributions of Figure 6-2, implying a reduction in the overall connectivity in the network similar to the dense network result. Similarly to Chapter 5, for the sake of clarity, the nodes' names will not appear in the figures as it would make them too crowded and impossible to read. In this section the discussion of specific nodes will be reserved for the nodes with extreme values, since discussing each node result in detail would be too long and confusing to the reader. The nodes with the highest degree in the dense networks were: DeCo—left (L) anterior cingulate (Label 21) (36.0), right (R) anterior cingulate (Label 1) (36.0) and the R somatosensory primary cortex (Label 16) (35.9), while in DePtu networks, they were: L retrosplenial cortex (Label 35) (36.5), L gustatory cortex (Label 26) (35.0) and R piriform cortex (Label 12) (34.8). However, in sparse networks the nodes with the highest degree were: SpaCo— L somatosensory primary cortex (Label 36) (17.1), R somatosensory primary cortex (Label 16) (15.7) and R anterior cingulate (Label 1) (15.1), while in SpaPtu, they were: L retrosplenial cortex (Label 35) (17.0), R piriform cortex (Label 12) (14.3), and R retrosplenial cortex (Label 15) (13.3).

Average node strength of PTU rats displayed a significant reduction compared to control brains in dense (9.8×10^{-10}) and sparse networks ($p = 1.6 \times 10^{-10}$), as shown in Figure 6-3. Table 6-2 shows average node strengths of PTU and control networks. Dense and sparse networks displayed similar node strength values with a reduction in the order of 10^{-3} . Like degree distributions, node strength distributions indicate a reduction in the number of strongly connected nodes (i.e. large node strength values). The degree and node strength distribution graphs of both dense and sparse PTU

networks failed to exhibit a long tail, suggesting that no hubs are present; therefore, a scale free organization is absent. The control network nodes with high node strength values were: L orbital cortex (Label 31) ($DeCo = 5.26 \times 10^{-2}$, $SpaCo = 4.66 \times 10^{-2}$), R orbital cortex (Label 11) ($DeCo = 4.81 \times 10^{-2}$, $SpaCo = 4.28 \times 10^{-2}$), and the third strongest node in the DeCo network was the L infralimbic cortex (4.10×10^{-2}), while in the SpaCo network the third strongest was the L piriform cortex (Label 32) (3.83×10^{-2}). Meanwhile, the PTU network nodes with high node strength values were: R orbital cortex (Label 11) ($DePtu = 4.89 \times 10^{-2}$, $SpaPtu = 4.12 \times 10^{-2}$) L orbital cortex (Label 31) ($DePtu = 4.35 \times 10^{-2}$, $SpaPtu = 3.79 \times 10^{-2}$) and the L gustatory cortex (Label 26) ($DePtu = 3.80 \times 10^{-2}$, $SpaPtu = 3.66 \times 10^{-2}$). In Figure 6-5 the anatomical location of some of the nodes is shown.

The binary clustering coefficient of PTU dense networks presented a significant reduction in clustering coefficients values, ($p = 2.96 \times 10^{-10}$); however, the sparse networks did not show a significant difference ($p = 0.242$). The clustering coefficient distribution (Figure 6-4) shows an overall reduction in clustering values, with the normal network displaying higher clustering than the PTU networks. Average clustering coefficient values for binary networks, over the entire network (Table 6-3), showed a high level of clustering (compared to null hypothesis networks) in dense and sparse networks, while null hypothesis networks only showed a high level of clustering in dense networks. The control networks displayed a high level of clustering for the following nodes: DeCo—R somatosensory secondary cortex (0.95), L somatosensory secondary cortex (0.92) and the R cortical amygdala (0.92), while in SpaCo, they were: R cortical amygdala (1.00), L cortical amygdala (0.85) and L somatosensory secondary cortex (0.78). Conversely, PTU networks displayed the following nodes with a high level of

clustering: DePtu— the R cortical amygdala (0.95), L temporal cortex (0.89) and the R insular cortex (0.89), while the SpaPtu displayed the following: the R cortical amygdala (1.00), L cortical amygdala (1.00), and L parietal cortex (0.83).

PTU networks display an increase on the average shortest path length in dense ($p = 6.77 \times 10^{-4}$) and sparse ($p = 1.71 \times 10^{-5}$) networks. The average shortest path length for PTU and controls was found to be similar to its value in comparable null hypothesis networks (Table 6-3). The shortest path lengths in control networks were associated to the following nodes: DeCo—R anterior cingulate (1.10), L anterior cingulate (1.10) and the R somatosensory primary cortex (1.10), while in SpaCo, they were: L somatosensory primary cortex (1.67), L piriform cortex (1.69) and the R piriform cortex (1.70). Shortest path lengths on PTU networks were found with the following nodes: DePtu—L retrosplenial cortex (1.09), the gustatory cortex (1.13), and the L piriform cortex (1.13), while in the SpaPtu, they were: L retrosplenial cortex (1.60), the piriform cortex (1.69), and L anterior cingulate (1.84).

The PTU networks displayed a significant reduction in weighted clustering coefficient values (using Equation 5-5) in dense ($p = 1.02 \times 10^{-8}$) and sparse ($p = 9.85 \times 10^{-8}$) networks, as shown in Figure 6-4 and Table 6-4. The PTU networks using clustering coefficient of Equation 5-4 also displayed a significant reduction in dense ($p = 9.09 \times 10^{-3}$) and sparse networks ($p = 2.32 \times 10^{-3}$) (see Table 6-4). With both measures, brain networks (PTU and controls) displayed a higher level of clustering than null hypothesis networks. Both dense and sparse weighted brain networks displayed higher clustering values than the null hypothesis networks, in contrast to the binary clustering coefficient, which only displayed higher clustering in sparse networks. This high

clustering indicates that the network organization in the rat brain maximizes local connectivity, which is not affected by TD. The highest clustering coefficient values (using Equation 5-5) in control networks were associated to the following nodes: DeCo—L tenia tecta cortex (0.27), R cortical amygdala (0.25) and L infralimbic cortex (0.24), while in SpaCo, they were: L tenia tecta cortex (0.40), R tenia tecta cortex (0.29), and the L infralimbic cortex (0.26). Conversely, the PTU networks displayed high levels of clustering using Equation 5-5, for: DePtu – R tenia tecta cortex, R cortical amygdala and L cortical amygdala, while in SpaPtu, they were: R tenia tecta cortex (0.37), L tenia tecta cortex (0.25), and the R cortical amygdala (0.25). In contrast Equation 5-4 yielded the highest values for the following nodes: DeCo—L orbital cortex (2.55×10^{-2}), R insular cortex (2.50×10^{-2}), and the R somatosensory secondary cortex (2.49×10^{-2}) while the SpaCo network displayed: R cortical amygdala (2.51×10^{-1}), L cortical amygdala (1.60×10^{-1}), and L orbital cortex (1.52×10^{-1}). Conversely, PTU brain networks displayed the highest clustering levels using Equation 5-4 for the following nodes: DePtu—L orbital cortex (2.28×10^{-2}), R orbital cortex (1.79×10^{-2}), and the L temporal cortex (1.57×10^{-2}), while in SpaPtu, they were: R cortical amygdala (3.02×10^{-1}), L cortical amygdala (2.10×10^{-1}), and L orbital cortex (1.46×10^{-1}).

PTU networks showed a reduction of weighted path lengths in dense and sparse networks; however, only dense networks display statistical significance ($p = 1.06 \times 10^{-9}$). Null hypothesis networks showed similar path length values as in both dense and sparse brain networks (Table 6-4). The strongest path lengths in control networks were associated to the following nodes: in DeCo they were: L orbital cortex (1.32×10^{-2}), R anterior cingulate (1.20×10^{-2}) and the L infralimbic cortex (1.07×10^{-2}), while in SpaCo

they were: R cortical amygdala (7.00×10^{-2}), L cortical amygdala (5.41×10^{-2}) and the L orbital cortex (5.20×10^{-2}). Strongest path lengths on PTU networks were found with the following nodes: in DePtU they were the following: R orbital cortex (1.22×10^{-2}), the L orbital cortex (1.09×10^{-2}), and the L gustatory cortex (0.95×10^{-2}), while the SpaPtU were: R cortical amygdala (7.34×10^{-2}), the L cortical amygdala (6.09×10^{-2}), and L orbital cortex (5.84×10^{-2}).

As seen in Figure 6-2, rat brain networks did not display a scale free organization. The clustering coefficient and path length results suggest non-random organizational features in the rat brain. Small worldness values, shown in Table 6-5, support the idea of small world organization in rat brains. Dense networks only show *sw* values of 1.03 and 1.04 for normal and PTU brains, respectively. On the other hand, sparse networks displayed values of 1.87 and 2.21 on normal and PTU networks. All weighted measures displayed *sw* values larger than 3.3 in all networks, PTU and normal, as well as dense and sparse, indicating more clearly organizational features of efficient networks using the weighted framework.

6.4. Discussion

In this study, cortical nodes were defined as network nodes, and streamlines calculated from tractography were defined as the network edges. Thyroid disruption has been shown to affect WM volumes and brain structure with volumetric analysis (Powell et al., 2012). This study shows that the changes with TD reduce brain connectivity; however it does not eliminate the organizational features of small world. Control and PTU networks displayed a linear decay in the degree distribution of sparse networks, suggesting that no scale free organization is present in rat brains. The degree

distribution suggests that TD reduces the overall connectivity in PTU brains. The most connected nodes (i.e. high degree) suggest TD prompts brain reorganization. Control networks display high degree values for anterior cingulate (Figure 6-5) and the somatosensory primary cortex (Figure 6-5), while PTU networks display high values in retrosplenial cortex and piriform cortex (Figure 6-5). The changes in the nodes with the highest degree suggest changes in organization upon TD, to maintain a high level of connectivity in the network. The values of high degree nodes were similar in control and PTU networks, with an overall reduction in the number of edges, hence a reduction of degree values, throughout the entire network. The nodes with highest degree values change on control and PTU networks; this can be interpreted as network reorganization in TD brains to maintain features of normal brains, like high connectivity.

Node strength values display a larger significant difference (controls vs PTU) than the degree values, which clearly supports previous findings of changes in brain structure due to WM loss. PTU brains display similar node strength distribution to control brains with an overall reduction in strength of connectivity throughout the entire network. Unlike degree, nodes with high strength values were the same in control and PTU networks; hence, the reduction in their value, agrees with the observation that WM volume is reduced in PTU brains (Powell et al., 2012). In this case, brains still maintain strong connection to the L and R orbital cortex (Figure 6-5 and 6-6), with reduction in the WM integrity (i.e., node strength) due to TD.

Organizational features of brain networks can be determined with the use of weighted network metrics. The clustering coefficient is related to specialized functions (e.g. visual, olfactory, and so forth). Control and PTU brains displayed a high level of

clustering in sparse networks (Table 6-3); however, dense networks displayed similar clustering results as the null hypothesis network. The high clustering in the dense null hypothesis network is due to the high number of edges, which artificially increases its overall clustering. Therefore, this is not due to organizational features in the null hypothesis or lack of it in the brain networks. The PTU dense networks displayed a significant difference in the binary (not weighted) measure of clustering from normal brains. The changes in clustering were not significant in sparse binary networks as weak edges were removed by thresholding. This can be attributed to changes in degree values; the average number of edges was reduced by 6% in dense networks, and 3% in sparse networks. The high clustering of brain networks that allow for specialized tasks is maintained with high graph densities (in weighted networks as shown Chapter 5 and 6) or TD (in sparse binary networks and weighted networks Section 6.3). The cortical amygdala displayed a high level of clustering in all networks, while the somatosensory secondary cortex displayed a high level of clustering in control networks. PTU networks, displayed a high level of clustering in the temporal and insular cortex (Figure 6-6) in dense networks and the parietal cortex in sparse networks. The graph density dependence of highly clustered nodes in the PTU networks is due to a high number of weak edges connecting the neighboring nodes of temporal and insular cortex, while stronger edges are associated to the parietal cortex neighborhood.

The path length displays similar values in brain and null hypothesis networks. This suggests an efficient brain organization that minimizes distances in the brain and this property is maintained even with TD. The somatosensory primary cortex and the anterior cingulate displayed small path lengths in DeCo networks while the

somatosensory and piriform cortex did so in SpaCo networks. Thresholding reduces the connections that allow anterior cingulate to display small path lengths. This implies that weak edges aid the anterior cingulate to achieve a high connectivity with the rest of the network, while the piriform cortex exhibits the smaller path lengths in SpaCo networks implying that stronger edges are connecting the piriform cortex to the rest of the network. The retrosplenial and piriform cortexes displayed small path lengths in both PTU networks (dense and sparse). The gustatory cortex displayed small path length in dense networks, while the anterior cingulate displayed small path length in sparse networks. The piriform cortex display showed small path lengths in all networks (DeCo, DePtU, SpaCo, and SpaPtU) suggesting that is an important node in rat brain. The piriform cortex is related to olfaction an important function for the rat. The rat does not have a good vision, but does have a great sense of smell. Therefore, it is logical to hypothesize that the rat brain is primed to protect the connectivity to and from its olfaction centers to enhance its survival.

The weighted approach also displayed non-random organization in rat brains. Unlike the binary clustering coefficient, the weighted clustering coefficient was able to demonstrate higher levels of clustering in dense brain networks compared to null hypothesis networks. It also displayed significant differences between PTU and normal brains at high and low densities. Control brain networks displayed a high level of clustering, using Equation 5-5 (Zhang), for the tenia tecta (Figure 6-5) and the infralimbic cortex (Figure 6-6), while in PTU networks, the high levels of clustering were displayed by the tenia tecta and the cortical amygdala. The cortical amygdala was also a highly clustered node in control brains, but only for dense networks. The tenia tecta

appeared to have strong connections between its neighbors, even with TD; however, the infralimbic cortex seems to have lost some of the strength associated with the connections of its neighbors with TD. Meanwhile, using Equation 5-4 (Onnela) the orbital cortex appears as the most clustered node in control networks, the somatosensory secondary and insular cortex display high levels of clustering on dense networks and the cortical amygdala does so in sparse networks. PTU networks display the orbital cortex as a clustered node as well, with the temporal cortex also displaying high levels of clustering at dense networks; finally the cortical amygdala does so at sparse networks. The case of sparse networks showed the same nodes with the highest clustering, with these displaying a reduction in their clustering coefficient values. The most clustered nodes, the tenia tecta, cortical amygdala and orbital cortex are associated with olfaction, memory and sensory integration, respectively. The high clustering of these nodes suggests an organization placing them as mediators to the aforementioned functions, which are of vital importance.

Lastly, the weighted path lengths displayed similar values in brain networks compared to null hypothesis, suggesting that the brain creates strong path lengths (pathways with large values of Equation 5-3) to maximize the presence of robust pathways in the brain. Weighted path length differences, from control to PTU brains gained statistical significance only on dense networks. The node with the strongest path lengths in dense networks was the orbital cortex, with the anterior cingulate and infralimbic cortex displaying strong values in controls, while the gustatory cortex (Figure 6-6) did so in the PTU brains. This suggests a reorganization reducing the strength of connectivity of the anterior cingulate and infralimbic structures upon TD.

Brain network and null hypothesis differences suggest an efficient, small world organization in the rat brain. Small worldness values are presented in Table 6-5, displaying larger *sw* values in all of the weighted networks than in the binary networks. Also, in binary networks only the sparse ones displayed *sw* values indicative of small world organization. Graph density affects the determination of topological features of networks at high values. So, arguably, the similar topological features of brain networks and null hypothesis networks at high density in binary networks are artifacts of the high density and the fact that all edges are equivalent in the binary approach. With binary networks, it is not possible to determine the small world property of brain networks at high graph densities. However using weighted networks described in this dissertation (Chapters 4 and 5) the small world property is obtained for even high graph densities. The ability to determine structural organization at high graph densities is due to the heterogeneity in the edge weights, which are efficiently organized to allow strong clusters and strong path lengths. This efficient organization is evident by calculating weighted clustering coefficients and path lengths at high graph densities.

6.5. Concluding Remarks

In this Chapter the small world organization in the rat brain was successfully determined. As expected, TD brains displayed reductions in connectivity and strength of connectivity. However, small world organization of rat brains was still present even after TD. Previous studies have shown deformities in WM and GM in rats' brains with thyroid hormone deficiencies (Powell et al., 2012). These deformities cause changes in brain structure in the form of reduced WM volumes and heterotopias (presence of GM in abnormal WM locations) in the corpus callosum. Rat brains with TD displayed reduced

global connectivity and strength of connectivity, implying that thyroid disruption reduces the brain connectivity by means of inhibited connectivity (reduced degree) and reductions of WM volumes, as shown by Powell (Powell et al., 2012) (reduced node strength). The strongest and most connected nodes in normal and PTU brains were not the same, suggesting that the WM reduction observed by Powell et al. (Powell et al., 2012) is not a global reduction but probably is accompanied by reorganization to make up the reduced WM tracks in the brain. A small sample was used in this study, possibly more brain samples than the ones described in this chapter and additional analysis (e.g. histology) should be made to fully support this claim. Since plasticity is a property of the brain, it should be expected that the brain would attempt to make up lost WM volumes to optimize its structure and display optimal network properties (the proof of this statement should be treated in future work). The high clustering coefficient and short path lengths obtained for PTU networks suggest that the reorganization is guided to maintain high connectivity in the network, which allows the brain to properly function. Basically, the brain reorganized to still allow an efficient communication in the entire network (small and strong path lengths) with high local connectivity to allow the complex functioning of brain regions (high clustering coefficients).

Even though it was found that there are structural changes associated with TD, the entire picture is not complete if one does not understand the functional changes associated with structural changes in the brain. In Chapter 7, a roadmap to merge the structural results of this dissertation (Chapter 4-6) will be shown with models to study the function in the brain.

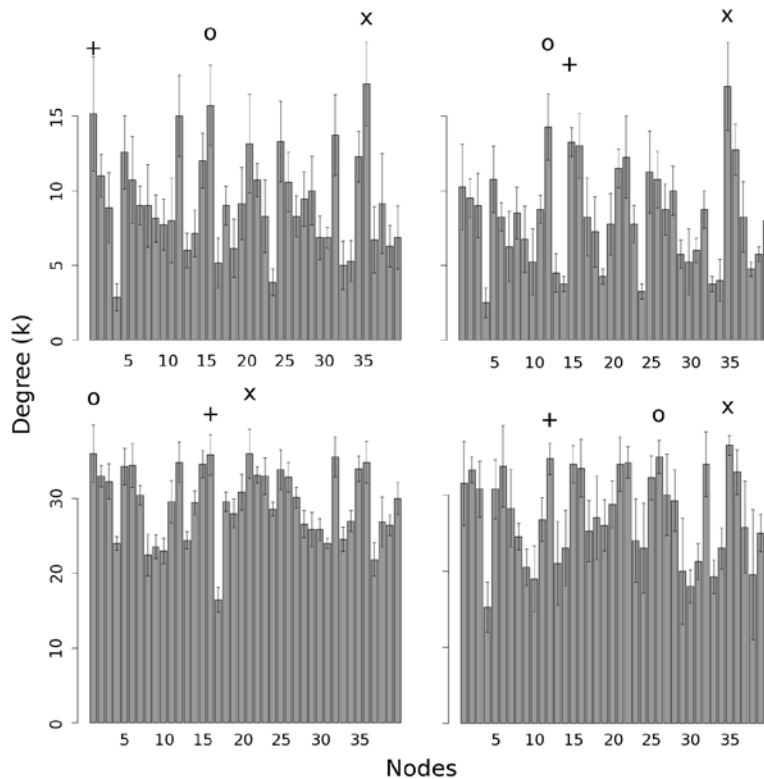


Figure 6-1. Degree values, results of rat networks. Top-left plot, normal and sparse networks. The marks correspond to the largest degree values: (x) L somatosensory cortex-node 36, (o) R somatosensory cortex-node 16, and (+) R anterior cingulate-node 1. Top-right plot, PTU and sparse brains. (x) L retrosplenial cortex-node 35, (o) R piriform cortex-node 12, and (+) R retrosplenial cortex-node 15. Bottom-left, normal and dense networks. (x) L anterior cingulate-node 21, (o) R anterior cingulate-node 1, and (+) R somatosensory cortex-node 16. Bottom-right, PTU and dense networks. (x) L retrosplenial cortex-node 35, (o) L gustatory cortex-node 26, and (+) R piriform cortex-node 12. The first twenty nodes represent the right side of the brain and the latter twenty represent the left side of the brain.

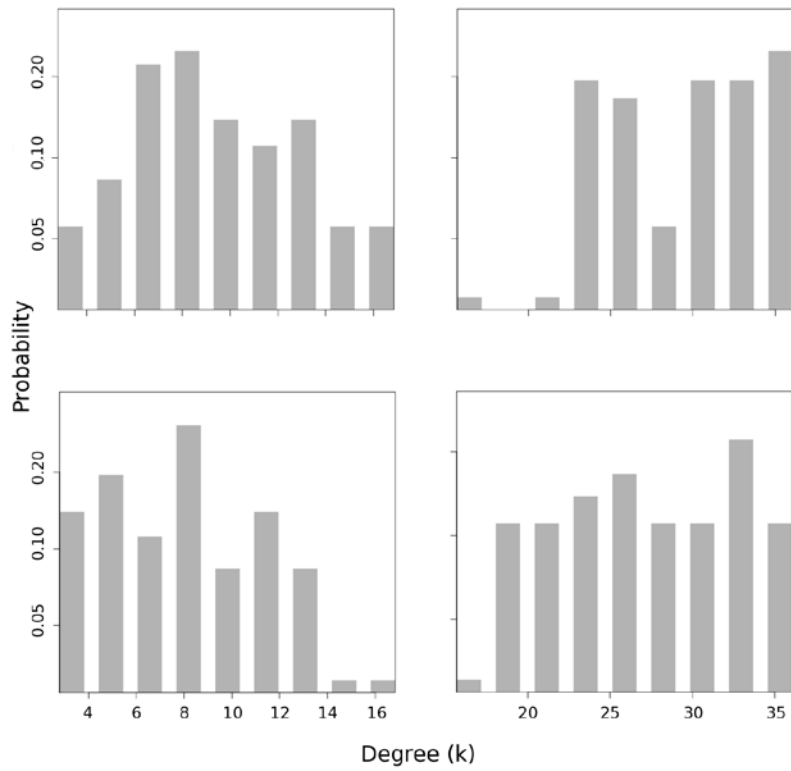


Figure 6-2. Degree distribution (log-lin) of rat brain networks. Top-left plot, normal and sparse networks. Top-right plot, normal and dense networks. Bottom-left, PTU and sparse brains. Bottom-right, PTU and dense networks.

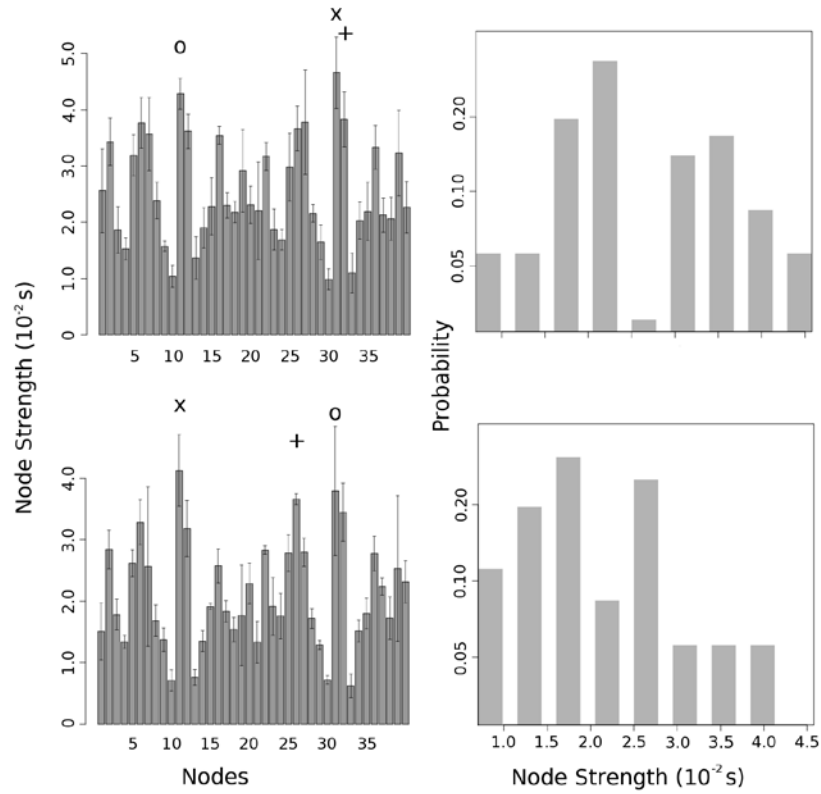


Figure 6-3. Node strength results of sparse networks. Top- left, node strength values of normal networks. The marks corresponds: (x) node 31, (o) node 11, and (+) node 32. Bottom-left, node strength values of PTU networks. The marks corresponds: (x) node 11, (o) node 31, and (+) node 26. The first twenty nodes represent the right side of the brain and the latter twenty represent the left side of the brain. Top-right, node strength distribution (log-lin) of sparse and normal networks. Bottom-right, node strength distribution of PTU brains.

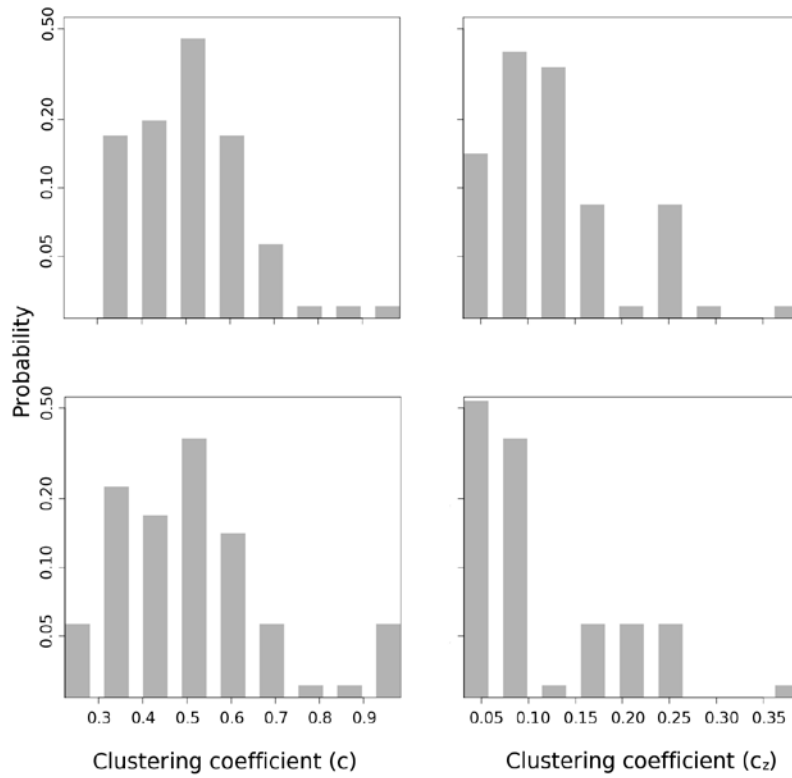


Figure 6-4. Clustering coefficients distribution (log-lin) of sparse networks. Top-left, distribution of binary clustering coefficient of normal sparse networks and bottom-left, of PTU brains. Top-right, weighted clustering coefficient (c_z) distribution (log-lin) of normal sparse networks and bottom-right, PTU networks.

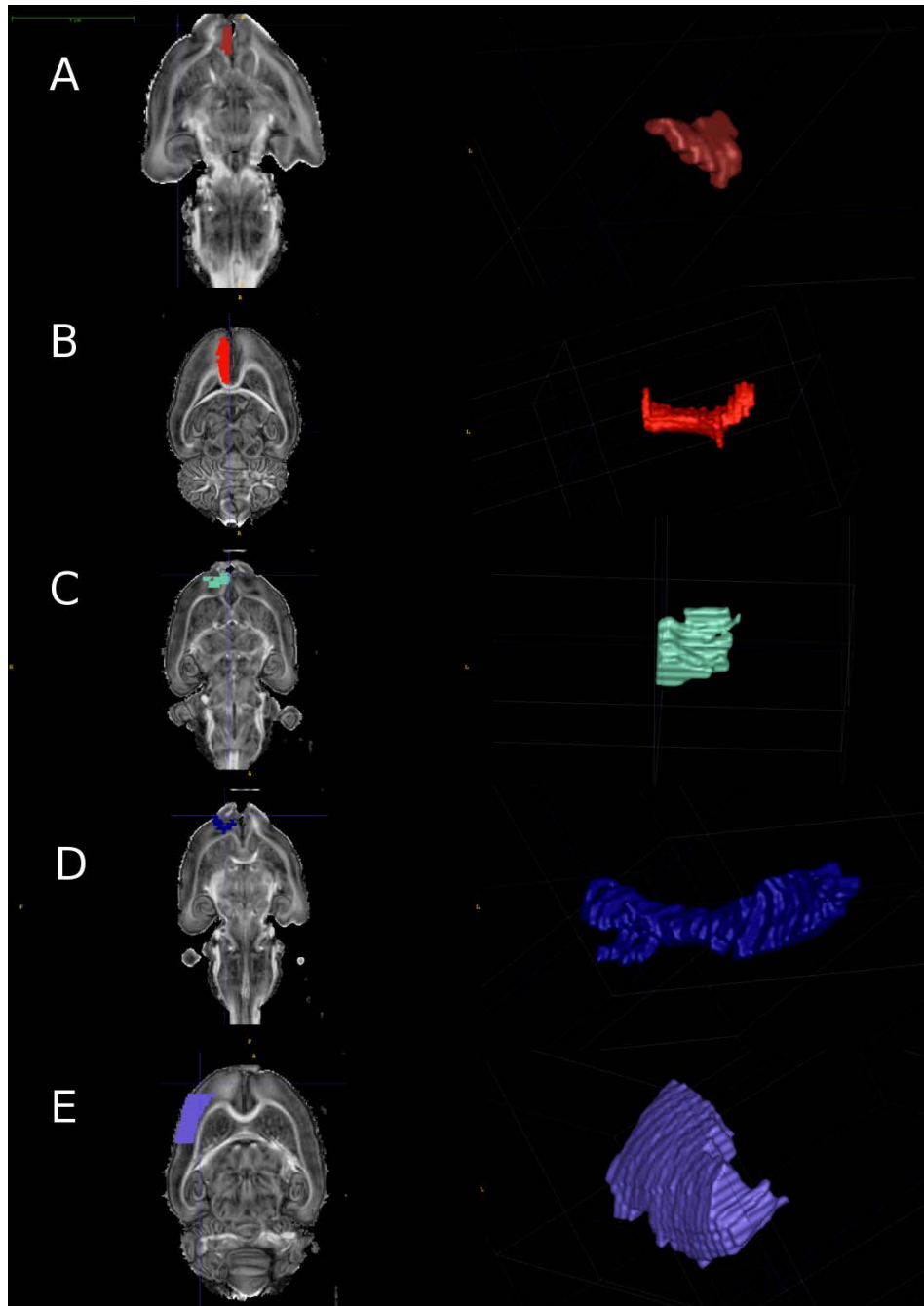


Figure 6-5. Anatomical location of rat nodes. A) Tenia tecta, node with high clustering coefficient values. B) Anterior cingulate, node high degree values in control brains. C) Orbital cortex, node with high node strength values in control brains. D) Piriform cortex, node with high degree values in PTU brains. E) Somatosensory cortex, node with high degree values in controls.

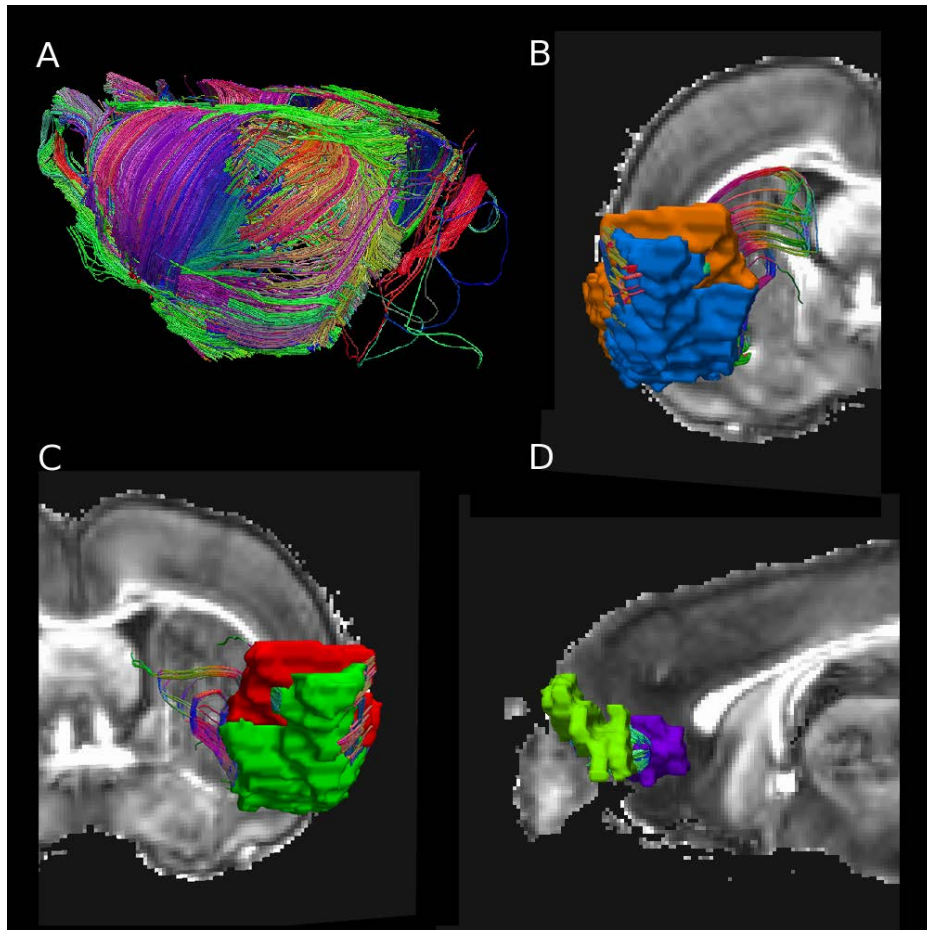


Figure 6-6. Streamlines connecting nodes in the rat brain. A) Whole brain tractography map. B) R gustatory cortex connected the R insular cortex. C) L gustatory cortex connected the L insular cortex. D) L infralimbic cortex connected to the L orbito-frontal cortex

Table 6-1. Average degree (\hat{k}) values and standard deviation (σ). PTU networks display reduction in mean values while maintaining similar high and low degree values. Standard deviation

	\hat{k}	σ
DeCo	29.4	4.80
DePtU	27.3	3.82
SpaCo	9.3	2.01
SpaPtU	8.2	1.62

Table 6-2. Average node strength (\hat{s}) values and standard deviation (σ). PTU networks display reduction in mean strength values, as a result of reduce WM volumes

	$\hat{s} (10^{-2})$	$\sigma (10^{-3})$
DeCo	2.75	3.63
DePtU	2.39	2.96
SpaCo	2.56	4.04
SpaPtU	2.11	3.35

Table 6-3. Binary network metrics. PTU brains display a reduced clustering and increased path lengths, as a result of reduced presence of connections.

	l_g	l_N	$C_{B,g}$	$C_{B,N}$
DeCo	1.26	1.26	0.85	0.82
DePtU	1.32	1.32	0.80	0.77
SpaCo	1.99	1.87	0.53	0.27
SpaPtU	2.09	1.93	0.51	0.21

Table 6-4. Weighted network metrics. PTU brains display a reduced clustering and increased path lengths, as a result of reduced WM integrity.

	$l'_g (10^{-3})$	$l'_N (10^{-3})$	$c_{O,g} (10^{-3})$	$c_{O,N} (10^{-3})$	$c_{Z,g} (10^{-2})$	$c_{Z,N} (10^{-2})$
DeCo	0.69	0.85	11.2	4.11	12.7	4.26
DePtU	0.60	0.77	9.50	3.64	9.90	3.40
SpaCo	2.90	3.47	72.9	17.7	13.0	4.16
SpaPtU	2.84	3.79	62.4	13.5	9.18	3.05

Table 6-5. Small worldness. All brains display small world organization, except dense networks as a result of high density of edges in the network

	Binary			Weighted (c_o)			Weighted (c_z)		
	γ	λ	sw	γ	λ	sw	γ	λ	sw
DeCo	1.03	1.00	1.03	2.73	0.81	3.36	2.99	0.81	3.68
DePtU	1.04	1.00	1.04	2.61	0.78	3.36	2.91	0.78	3.74
SpaCo	1.99	1.06	1.87	4.11	0.84	4.92	3.12	0.84	3.74
SpaPtU	2.39	1.08	2.21	4.64	0.75	6.19	3.01	0.75	4.01

Table 6-6. Rat brain network nodes. The number in both hemispheres column correspond to the node placement in Figures 6-1 and 6-3.

Hemisphere		Cortical region
Right	Left	
1	21	Anterior cingulate
2	22	Agranular insular
3	23	Auditory
4	24	Cortical amygdala
5	25	Entorhinal
6	26	Gustatory
7	27	Infralimbic
8	28	Insular
9	29	Primary motor
10	30	Secondary motor
11	31	Orbital
12	32	Piriform
13	33	Prelimbic
14	34	Parietal
15	35	Retrosplenial
16	36	Primary somatosensory
17	37	Secondary somatosensory
18	38	Temporal
19	39	Tenia tecta
20	40	Visual

CHAPTER 7 FUNCTIONAL NETWORKS

7.1. Opening Remarks

The brain is a dynamic system of interconnected regions that give rise to our everyday functions and behavior. Even when no task is occurring, multiple regions of the brain are actively firing and communicating, which causes a latent baseline activity known as the default mode network or DMN (Raichle et al., 2001). This is a robust behavior of the brain, even across species, such as monkeys (Vincent et al., 2007), chimpanzees (Rilling et al., 2007) and rats (Lu et al., 2012). The driving anatomical regions of this network are yet still to be determined. Employing models to study the function of brain networks, the sources of the DMN can finally be understood and more intrinsic activities of the brain can possibly be elucidated.

Models of interacting brain regions (i.e. ensembles of neurons) have been used to study the emergent dynamics of brain using fMRI. These models attempt to create a realistic model of interacting cortical regions as a network (Friston et al., 2003; Wilson and Cowan, 1972). The general idea of these models is to recreate the dynamical interactions of large structures. This approach simplifies the dynamics obtained from single neuron-neuron interactions (Hodgkin and Huxley, 1952), by modelling ensembles of neurons without the need to solve dynamics of single neurons. The dynamic causal model (DCM), which is explained in the next section, obtains dynamical process information with a series of a priori inputs that resemble the nervous system inputs into the brain (e.g. visual, olfactory and so forth). One of the assumptions in DCM is that the responses are caused by changes in the inputs. These changes lead to effective

connectivity changes which are parameterized in terms of coupling among brain regions. Friston defines effective connectivity as the influence that one neuronal region exerts over another by inducing a response of the form $\partial \dot{z} / \partial z$ (Friston et al., 2003). DCM is used to test the specific hypothesis that motivates a particular observed function in the brain (Brazdil et al., 2007; Stefan and Lopes da Silva, 2013). In DCM, inputs can produce responses in one of two ways: changing state variables (i.e., neuronal activity) or effective connectivity. Direct changes in the state variables can be perceived as sensory input that triggers direct responses in associated brain areas.

DCMs are not restricted to linear or instantaneous systems; hence, they are complicated and potentially need a large number of free parameters (if the numbers of nodes get large). The DCM model estimates the interactions between regions with bilinear approximations. The bilinear approximation reduces the parameters in the model to three: 1) the direct or external effect of inputs on brain regions, 2) the intrinsic or latent connections that couple responses of one region to others, and 3) changes in the intrinsic coupling induced by inputs. DCM is primarily used to answer questions about the modulation of effective connectivity through deductions about the inherent connections and couplings. The external effects will become a prominent parameter when correlating structure and function.

7.2. Theory

In this section DCM as explained by Friston (Friston et al., 2003) is summarized. For a more in depth discussion the reader is referred to (Friston et al., 2003). Friston first constructs the network by defining a number of interacting brain regions. The model is composed of m inputs to the brain regions and l outputs (one per region). The m

inputs correspond to the stimulus on each region. The idea of the model is for each of the I regions to produce a measured output that corresponds to an observed BOLD response.

Friston defines the neuronal state $z = [z_1, \dots, z_I]^T$ to take any arbitrary model to determine the effective connectivity, as shown in Equation 7-1.

$$\dot{z} = F(z, u, \theta) \quad (7-1)$$

where F is some nonlinear function describing the neurophysiological influences of the activity z and u exert upon changes in the other regions. The $\theta = \{A, B^j, C\}$ are the parameters of the model to be determined from the data. Equation 7-1 can be modified in terms of effective connectivity, as shown in Equation 7-2.

$$\dot{z} = \left(A + \sum_{j=1}^J u_t(j) B^j \right) z_t + C u_t \quad (7-2)$$

where t is time, z_t is the neuronal activity, $u_t(j)$ is the j^{th} input at t , and A , B^j , and C are the connectivity matrices. The connectivity matrix A represents the connectivity among the regions in the absence of input or structural connectivity. A represents the strength of connections between the regions, context-independent or free of functional correlation. Effective connectivity is the expression in brackets in Equation 7-2, which is obtained by inducing a response of the form $\partial \dot{z} / \partial z$. In DCM, a response is defined in terms of a change in activity with time (Equation 7-1). The effective connectivity can be understood as the intrinsic coupling in the absence of experimental perturbations. Perturbed states depend on the experimental design; therefore, the intrinsic coupling is specific to each experiment. The matrices B^j are effectively the change in coupling induced by the j^{th} input. They encode the input-sensitive changes in $\partial \dot{z} / \partial z$ or the modulation of effective

connectivity by experimental manipulations. The matrices B^j represent the modulation of the connections of A (e.g. due to learning, attention, etc.) induced by the j^{th} input $u_t(j)$. Because B^j are second-order derivatives these terms are referred to as bilinear. Finally, the matrix C embodies the extrinsic influences of inputs on neuronal activity. The C matrix represents the influence of direct (exogenous) inputs to the system (e.g. sensory stimuli). The parameters $\theta = \{A, B^j, C\}$ are the connectivity or coupling matrices that DCM attempts to identify, which define the functional organization and interactions among brain regions at a neuronal level. In order to merge structural and functional results, correlations between structure and function have to be introduced since all parameters in DCM are rate constants and are in units of s^{-1} .

7.3. Global Functional and Structural Networks

Interactions between regions are modeled by DCM at the neuronal level. Neuronal modeling is more biologically accurate and appropriate than hemodynamic modeling, because neuronal interactions do not necessarily lead to detectable hemodynamic responses. DCMs are able to work at the neuronal level because they employ a 'forward model' (with hemodynamic parameters) relating neuronal activity to fMRI activity (Penny et al., 2004). Also, in DCM, one can postulate arbitrarily complex connectivity patterns between regions leading to better fitting models and biologically more realistic.

Recently, there has been growing interest in the modeling of larger networks or graphs, as the ones described in Chapters 5 and 6. However, increasing the number of regions or nodes in a DCM presents some problems. Clearly, the number of connections or edges increases with the square of the number of nodes (number of

edges = $N*(N-1) \sim N^2$). This can lead to models with enormous numbers of free parameters and complicated dependencies among the parameters (Seghier and Friston, 2013). This in turn calls for the need to reduce the number of free parameters in the DCM.

It is generally accepted that anatomical connectivity provides important constraints on effective connectivity (Stephan et al., 2009). It is important to note that anatomical connectivity constrains but does not determine effective connectivity. There are several reasons for this. First, the function of a synapse depends on its recent history. For example, in the absence of any structural changes of the synapse, marked facilitation or depression of synaptic transmission can occur at a timescale of milliseconds (Zucker and Regehr, 2002). A second, and probably more important, reason why there is no one-to-one mapping between anatomical and effective connectivity is that the structural presence of a synaptic connection does not determine whether it will be engaged during a particular process or not.

7.4. Structural constraints to large DCMs

Tractography based constraints were introduced as a method to determine the parameters of DCMs (Stephan et al., 2009). With the use of tractography, one can estimate the probability that a given fiber pathway exists to constrain the range of the effective connection strength in DCM. In other words, the structural connection strength is used to estimate the prior variance of the corresponding coupling parameter (A, B) (See Equation 7-2) in the DCM. The most intuitive notion is that the higher the probability that a given connection exists, the larger one should set the prior variance of the corresponding effective connectivity. This increases the probability that the effective

connectivity for a given stimulus deviates from inactive to represent a strong functional connection.

In Chapters 4 and 5 an edge weight and a framework to study weighted networks was presented to estimate the structural connectivity derived from DWI. The edge weight measures the relative strength of connection within the network. It has been shown that functional neural networks composed of weak and strong connections optimize spike-based communication (Teramae et al., 2012). This network of heterogeneous connections leads to background noise generation in the network, which improves communication of strong synapses. Also, this background noise might be crucial to the DMN. The structural networks obtained can be used to set the DCM parameters. First, A can be stipulated from the weighted structural networks described in this dissertation (Chapters 4-6) where the values of a_{ij} serve as modulators to the strength of communication. The rates characterizing the DCM (θ^c) can be determined from structural edges weights (Chapter 4) by the relation described by Stephan (Stephan et al., 2009). DCM for large networks like the one described in Chapter 5 requires a large number of free parameters, which makes it difficult to estimate. In the brain, there is a large level of redundancy in the neurons of anatomical regions (Wilson and Cowan, 1972), which means that the neurons within some cortical region will present nearly identical responses for the same stimuli. The notion of redundancy can be extended to interactions between regions such that there is level of redundancy in the coupling response of nearly equal connection strengths (i.e. edge weights) to identical stimuli to reduce the number of free parameters in large DCMs. This assumption allows a first level estimation of the couplings, B^j , for influences of

stimulations at different level of connectivity: strong (high edge weight), moderate and weak (small edge weight). This first level estimation should be tested and extended to add more levels of connectivity strength until the desired output is obtained. Therefore the structural weighted networks described in this dissertation can be combined with DCM to determine the anatomical sources of the DMN and any other functional network in the brain.

CHAPTER 8 CONCLUSION AND FUTURE DIRECTIONS

8.1. Conclusions

The work in this dissertation was focused on the development of novel techniques to study networks. Brain networks are used to set a formulation to study weighted networks and determine their weighted topological features. First, an edge weight, derived from tractography and diffusion MRI, is presented to quantify the connectivity strength between regions in the brain. In doing so, a foundation is made to weigh brain networks.

The edge weight described in Chapter 4 is a novel approach to defining connectivity within the brain. The edge weight is derived from MRI and tractography. The edge weight takes into consideration that only streamlines originating from the pathway should be used to quantify the connectivity. Also the normalization (V_{voxel} / P_{voxel}) ensures that edge weight reduces its dependence on seed point and fiber scales. The edge weight introduces a mechanism to filter extraneous streamlines. The filtering removes streamlines, from the set of all streamlines connecting any two nodes that originate outside the portion of the streamline that connects the nodes. The mechanism of filtering ensures that the edge weight displays fiber paths and the strength of connectivity within the brain as objectively as MRI allows, instead of just using arbitrary notions of connectivity (streamline count, FA along a path, non-normalized edge weights) derived from tractography. The edge weight provides a useful tool to look at local networks within the brain. It also serves as a reasonable measurement to model global networks, relying on differences in the connectivity strengths within the brain.

Weighted networks seem like a natural fit to study real world networks, in part because many of the connections between components of a network cannot be determined with exactitude. Exact measurements of the strength of connectivity would be an ideal situation, where these measurements can be used to determine weighted networks, for example “friendship” between any two individuals or the strength of WM bundles connecting nodes. However, to my knowledge, an unambiguous and objective “friendship” metric does not exist to allow quantifiable differentiation of a wife from a coworker. In the brain, the proposed edge weight performs this role, as weak connections are differentiated from strong ones, creating a dense network (i.e. with more than 50% of all possible edges existent in the network) while maintaining the organizational features of brain networks obtained from tractography and simple networks. As expected, the new measurement agrees with currently accepted knowledge of brain structure and introduces a new outlook about network organization. The generalized framework relaxes restrictions on the graph density of networks and allows for the estimation of topological features of networks, even at high graph densities. When the density of edges in binary networks is high, almost any node is connected to any other node, which implies an expensive and ineffective network. With the weighted networks, a new picture arises. Networks become an entangled mesh that contains many connections, weak and strong, yielding an efficient network organization. The new organization emphasizes increased connectivity strength of a few edges, while weak connections can be seen as auxiliary connections to improve the resilience and robustness of the network.

The idea of studying networks must be accompanied by an application to study perturbation to the real networks. A perturbation in the brain is expressed as pathology. By learning how pathologies change brain structure and network organization, new universal principles of real world networks can possibly be developed that aid in understanding the general principles of network structure and organization. The small world organization of brain networks is maintained even with a perturbation of WM reduction. The preservation of brain structure is achieved by strengthening the weak connections of the normal network, and inducing a network rearrangement to allow complex tasks and functions to be performed. This behavior of rearrangement can be difficult to explain with the idea of sparse networks; hence, dense networks with heterogeneous connectivity distribution can serve as model to describe the widespread changes in connectivity in the brain. An analogy to this behavior can be seen in a situation where some catastrophic event occurs between two best friends (strong connection), causing their friendship to be diminished or destroyed. The individuals without a best friend will most likely compensate for that lack of friendship by getting close to another good friend, as opposed to become best friends with a recently met acquaintance. Hence, another advantage to using weighted networks comes from the possibility to identify potential ways of restructuring networks after an attack or a perturbation.

8.2. Future Directions

A problem with defining nodes in MR images is being able to accurately determine a relevant anatomical or functional region given the coarse size of voxels in relation to neuron size. For example, if a grid like structure (bottom map in Figure 8-1) is

placed on top of the map of Puerto Rico (PR), the pixels in the PR map are too large to be segregated as all administrative autonomous municipalities (Top map in Figure 8-1). Therefore if a different criterion is chosen to define nodes like electoral districts (Middle map Figure 8-1), then it is possible to obtain a more accurate description of the topological diversity in PR from the grid like structure. Similarly, all brains vary in size and shape. Guidelines that allow segmentation of the brain into a set of functionally relevant network nodes need to be established (see Figure 2-7). fMRI can be a useful tool to reach this goal, as it allows the network in the brain to segregate areas in terms of their functional behavior. Using the process described in this dissertation will make it possible to examine the structural connectivity in the brain with functionally connected nodes (defined by fMRI), which enables us to relate the functional connectivity with the structural organization of the brain. In addition to these concerns about resolution, the validation of small pathways is also necessary to understand the limitations and capabilities of tractography as a method to estimate brain connectivity. Addressing the issue of MRI resolution would yield a more appropriate answer as to what is sufficient resolution to estimate small pathways. In this dissertation it was emphasized the importance of weak edges. A caveat with these weak edges is that their anatomical validity has not been established relative to the obtained MR resolution. From the point of view of networks it is feasible that the weak edges are real since the brain displayed small organization with its presence; however a more extensive analysis of them is necessary. In Figure 8-2, a preliminary analysis is shown to establish the connection between tractography and small pathways. In this figure, a high resolution scan of a human hippocampus was obtained and subsequent histological analysis is underway.

This work will allow us to find the correlation between the streamlines observed from MRI and the real anatomical structures observed from histology. Finally it will provide insights to determine better tactics to perform the tractography process.

The brain has been found to have properties of small world networks as validated in this work. Also, scale free organization has been reported, but in fewer studies. The scale free organization has been associated with the use of fMRI and functional networks. Looking for the link between scale free and small world can consolidate these findings and possibly set a mathematical foundation for the brain network formation. A first lead to defining this problem can possibly be found in the topology of both networks: functional and structural. The structural networks are restricted by a physical topology, which limits the connectivity by some physical constraints like size or active sites. Functional networks, on the other hand, are restricted by a logical topology, in which the connectivity arises from communication or sensing of remote areas.

Finally, the consolidation of functional and structural networks can give insight towards a theory of network formation. The current models (random, scale free and small world) lack the physical constraints (like node size, spatial constraints to make connections, and so forth) and only seek to replicate observed properties of real networks. Current knowledge regarding brain organization cannot allow the creation of such theory. The development of a theory describing network formation may be possible after the dynamics of network formation and topological manifestations are understood, along with basic concepts, such as energy and entropy. The brain is organized to minimize distances and maximize local connectivity; therefore, the small world model certainly seems like a logical place to start such a theory. However, the

brain is a very energy expensive system within our bodies, consuming about 20% of all our energy. Therefore, low cost models like the small world certainly cannot be the entire answer. The brain seems like a good starting point since the study of both of its topologies (physical and logical) already garner a great deal of attention and effort. The consolidation of discoveries regarding the dynamics and structure of brain networks will provide necessary insights toward the determination of basic principles that describe real-life networks. Ultimately, concepts like energy consumption, network formation, and network recuperation could potentially be the building blocks of a complete description of brain networks and their dynamics.

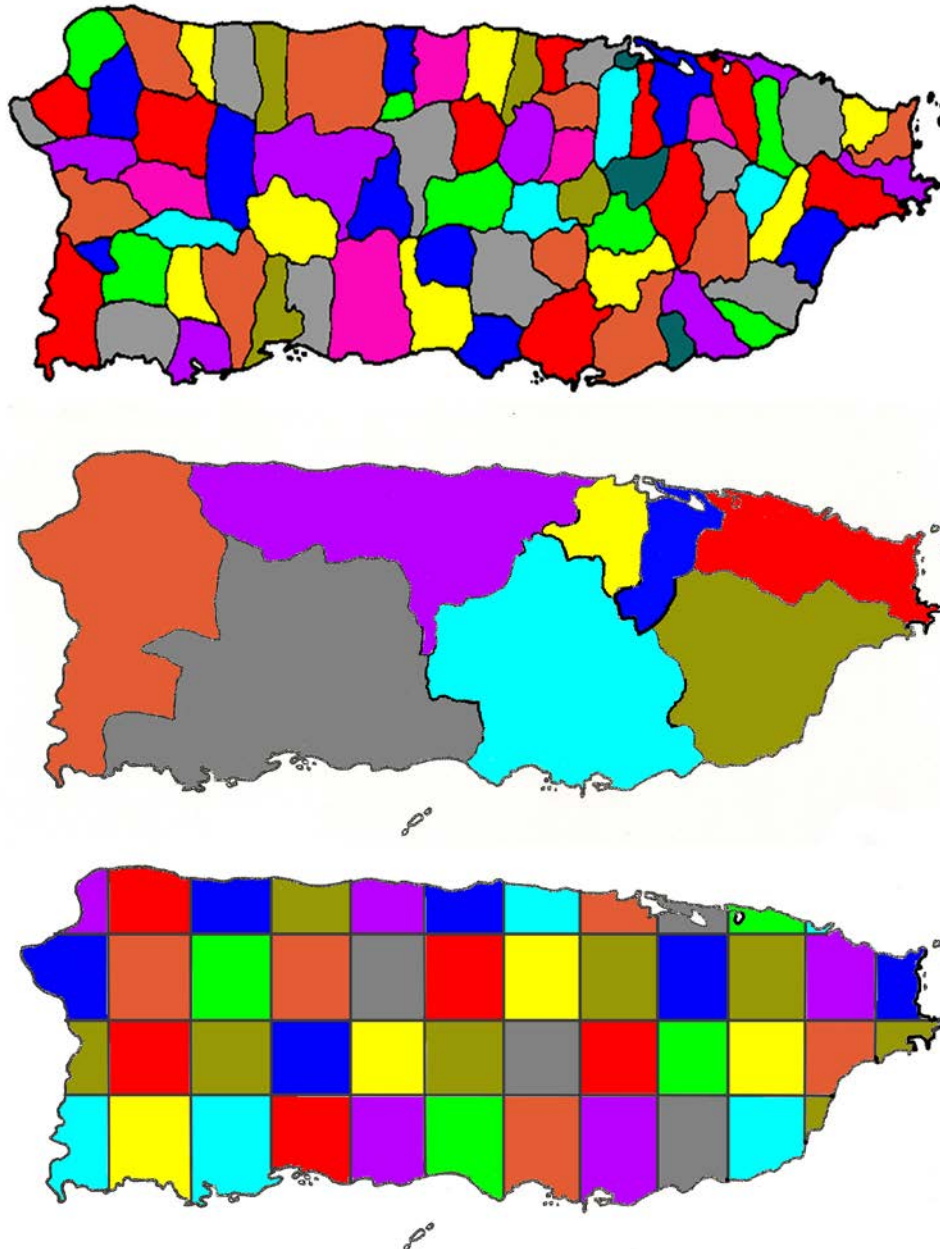


Figure 8-1. Resolution effects on town borders in Puerto Rico. Top map shows the actual town borders. Middle map, shows the senatorial boundaries. Bottom map, shows if only squares can be made to discern between land portions. The original shape and actual town borders cannot be discerned; however a reasonable arrangement of boxes can be made for the senatorial district.

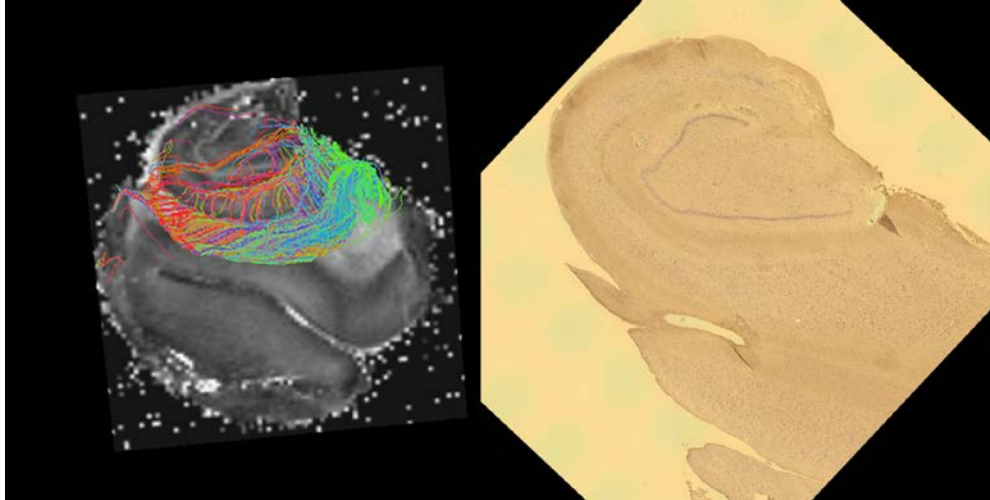


Figure 8-2. Validation of streamlines obtained with tractography with histology. Image on the left corresponds to streamlines connecting to the hippocampus calculated with tractography. Image on the right, corresponds to a representative histological slide approximately is the same location to the image on the right. A reconstruction of the fiber that connects the hippocampus can aid to determine the validity of tractography for small pathways and help optimize tractography schemes.

APPENDIX A OPTOGENETICS AND FMRI

An adult male rat was injected with 2 μ L of AAV9-ChR2-mCherry. AAV9 is a virus used to infect the neurons with light-gated properties. ChR2 is a protein that functions as the light-gated ion channel. mCherry is a fluorescent protein that serves to verify the gene transduction into the tissue. The rats were infused in the right M1 (motor cortex) with the virus and also a cannula was implanted to deliver light into the M1. Three weeks after the injection, the rat was anesthetized and imaged. Functional activity was measured using fMRI and 4.7 T horizontal bore magnet (Agilent). A receive only passively decoupled quadrature surface coil was constructed to be used to perform the fMRI acquisition. A transmit only, actively decoupled quadrature birdcage coil was used for excitation. An EPI sequence was used to acquire a time series of images with the following set of parameters: TR/TE = 750/20 ms with resolution of 0.500 x 0.500 x 0.750 μ m. Fourteen slices around the cannula site were acquired to verify localized activation. The time series was repeated 7 times to average the fMRI images. Structural scans were acquired using a spin echo sequence with: TR/TE= 2500/45 ms, with a resolution of 0.273 x 0.273 x 0.750 mm. A 40 mW 473 nm laser was pulsed at 20 Hz in 30 seconds on - 30 seconds off light cycle for 6 minutes. The data was analyzed by calculating the individual voxel coherence, defined as the magnitude of the frequency component divided by the sum-of-squares of all frequency components.

Analysis shows successful activation of the M1 region. Figure A-1 shows BOLD activation around the cannula site, the time series of the MR signal at the cannula location and the frequency spectrum of the activated site. The time series of the signal

agrees with the light on and off cycles, suggesting that the response is due to the light. Histology studies were performed and the gene was found in the area of activation. Additional activation was observed in voxels 7.5 mm away from the cannula site. This appears to display a functional coherence between remote areas, which suggests that connectivity can be measured with fMRI.

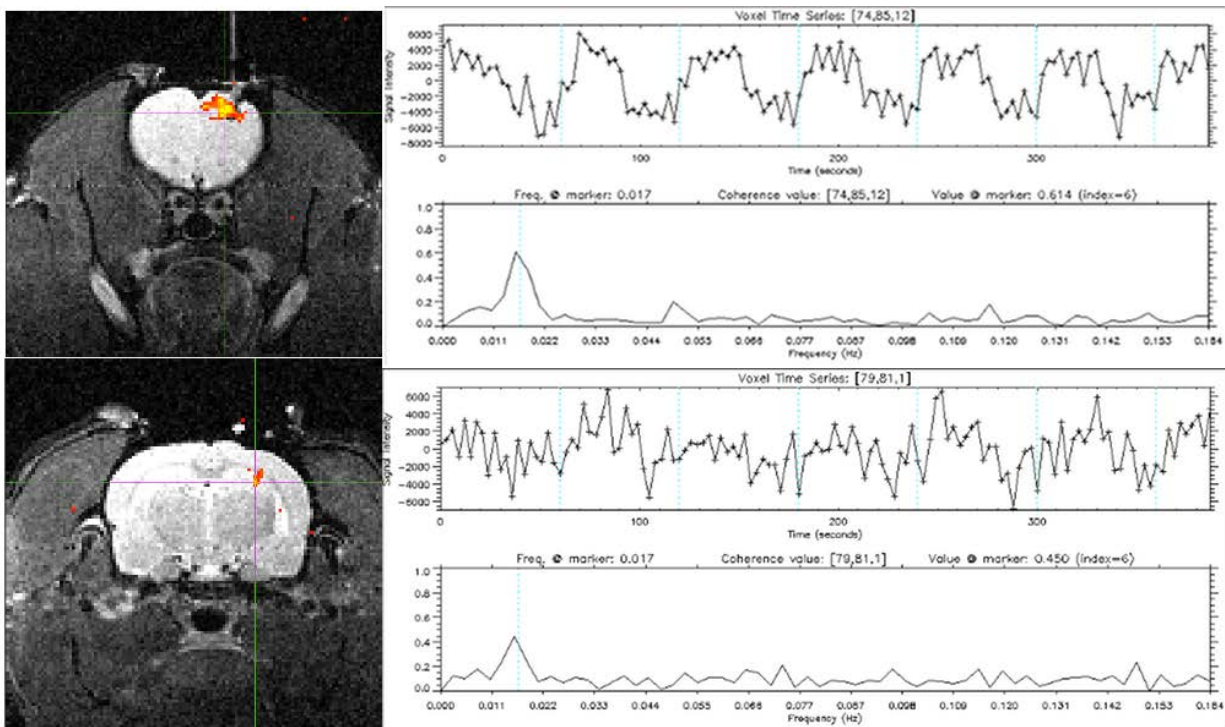


Figure A-1. Optogenetic stimulation and activation captured with fMRI. Top is the activation site in the motor cortex. Activated voxels 7.5mm away from activation site in the hippocampus.

APPENDIX B
CONTINUOUS EDGE WEIGHT REPRESENTATION

In this dissertation an edge weight is derived from streamline tractography to measure the strength of an edge relative to the total nodes' surface area. In this appendix the edge weight is described on a continuous space. The edge weight of Equation 4-1 takes form given by the following expression,

$$w(e_{ij}) = \frac{1}{\langle A \rangle} \frac{1}{\bar{l}(f_R)} \int_R dV, \quad (B-1)$$

where the integral over R defines the volume occupied by the fiber. In Equation B-1, A is the mean surface area of the nodes, which is given by

$$\langle A \rangle = \frac{\iint_T \left(\sqrt{\left(\frac{\partial g_1}{\partial x} \right)^2 + \left(\frac{\partial g_1}{\partial y} \right)^2 + 1} \right) dx dy + \iint_T \left(\sqrt{\left(\frac{\partial g_2}{\partial x} \right)^2 + \left(\frac{\partial g_2}{\partial y} \right)^2 + 1} \right) dx dy}{2}, \quad (B-4)$$

where g_i is the function describing the surface along the z axis of node i and T is the region of the node occupied in the xy plane. In Equation B-1, $\bar{l}(f_R)$ is the mean length of the edge for all fibers located within region R and making a connection between the nodes and it is specified by

$$\bar{l}(f_R) = \frac{1}{s_2 - s_1} \int_{s_1}^{s_2} s dl = \frac{1}{s_2 - s_1} \int_{s_1}^{s_2} \left(\int_0^l \sqrt{1 + f'(x')^2} dx' \right) dl, \quad (B-2)$$

where

$$s = \int_0^l \sqrt{1 + f'(x')^2} dx' \quad (B-3)$$

In Equation B-2, $f(x)$ is a function describing the trajectory of the fiber, its slope is given by f' and the length of individual fibers is given by s (Equation B-3).

In the denominator of Equation B-1 there is a volume measure (A^*), this value is analogous to the total volume of a cylinder where the volume is the area of the cross section of the cylinder times its length. Also in the numerator there is the total volume of the space occupied by the fiber connecting the nodes. Therefore the edge weight represents the ratio of the total volume occupied by the fiber that connects nodes by the total physical spatial volume that is available to make connections.

Calculation of the slant on plane

The continuous edge weight (Equation B-1) is used to calculate the strength of connectivity between two nodes as the ones shown in Figure 4-4b. The surface area of a cubic node of sides d is given by

$$\langle A \rangle = 6d^2. \quad (\text{B-5})$$

The average fiber length, with any number of voxels separating the nodes is given by

$$\begin{aligned} \bar{l} &= \frac{1}{M+1-M} \int_{Md}^{(M+1)d} \int_0^l \sqrt{1+1} dx' dl = \sqrt{2} \int_{Md}^{(M+1)d} x' \Big|_0^l dl = \sqrt{2} d \frac{l^2}{2} \Big|_M^{M+1} \\ &= \sqrt{2} d \frac{(M+1)^2 - M^2}{2} = \sqrt{2} d \frac{2M+1}{2}. \end{aligned} \quad (\text{B-6})$$

Alternatively, the average length is the average of the shortest and longest fiber. In this case all fibers are distributed evenly in the xy plane, forming a square cross section where the fibers connects the node; therefore, the mean fiber length obtained by

$$\bar{l} = \frac{\sqrt{2}Md + \sqrt{2}(M+1)d}{2} = \sqrt{2}d \frac{2M+1}{2}, \quad (\text{B-7})$$

which is the same result of Equation B-6. The volume occupied by the fiber in R , is calculated by volume integral in Equation B-1 and is obtained by

$$\int_R dV = \begin{cases} R_1 & 0 < z < d, 0 < x < d, 0 < y < d(x+1) \\ R_2 & 0 < z < d, d < x < d(M+1), dx < y < d(x+1) \\ R_3 = R_1 + R_2. \end{cases} \quad (\text{B-8})$$

First, the integral over R_1 is given by

$$\int_{R_1} dV = \int_0^d \left(\int_d^{(x+1)d} \left(\int_0^d dz \right) dy \right) dx = d \int_0^d y \Big|_d^{(x+1)d} dx = d^2 \int_0^d x dx = d^3 \frac{x^2}{2} \Big|_0^1 = \frac{d^3}{2}. \quad (\text{B-9})$$

Then the integral over R_2 is obtained by

$$\int_{R_2} dV = \int_d^{(M+1)d} \left(\int_{xd}^{(x+1)d} \left(\int_0^d dz \right) dy \right) dx = d^2 \int_d^{(M+1)d} 1 dx = d^2 \int_d^{(M+1)d} dx = d^3 x \Big|_1^{M+1} = d^3 M. \quad (\text{B-10})$$

Finally employing the expression for the entire volume R (Equation B-8) and the solutions of Equations B-9 and B-10 yields the volume for the entire region R by the following expression,

$$\int_R dV = 2 \left[\int_{R_1} dV + \int_{R_2} dV \right] = 2d^3 \left[M + \frac{1}{2} \right] = d^3 (2M + 1). \quad (\text{B-11})$$

In conclusion the edge for the slant on a plane with the nodes' surface area specified by Equation B-5, a mean edge length equal to Equation B-6 and the volume occupied by the fiber obtained by Equation B-9, yields an edge weight given by

$$w(e) = \frac{1}{6d^2} \frac{1}{\sqrt{2d} \frac{(2M+1)}{2}} (2M+1)d^3 = \frac{1}{3\sqrt{2}} \approx 0.235, \quad (\text{B-12})$$

regardless of the physical length of the edge.

Calculation of the slanted 3d fiber

The continuous edge weight is now used to calculate the connectivity strength for a fiber shown in Figure 4-5. The surface area of the nodes is given by Equation B-5. The volume occupied by the fiber (Figure B-1) yields two long fibers for every short one (Figure B-2), forming a triangular cross section instead of square cross section as the slant on plane example. As the separation of the nodes, M , is increased one obtains the following number of fibers,

$$\begin{aligned}
 M_1 &= 1 & \sqrt{3} + 2(2\sqrt{3}) \\
 M_2 &= 2 & \sqrt{3} + 2(3\sqrt{3}) \\
 M_3 &= 3 & \sqrt{3} + 2(4\sqrt{3}) \\
 &\vdots & \vdots \\
 M_M &= M & \sqrt{3} + 2((M+1)\sqrt{3}) .
 \end{aligned} \tag{B-13}$$

The mean length at any separation, M , of the voxels is given by

$$\bar{l} = \frac{\sqrt{3}Md + 2\sqrt{3}(M+1)d}{3} = \sqrt{3}d \frac{3M+2}{3} . \tag{B-14}$$

The occupied volume by the fiber occupies on each voxel (Figure B-3 and B-4) is obtained by calculating the following,

$$\int_R dV \approx R_1, \quad 0 < z < dy, \quad 0 < x < d, \quad 0 < y < dx . \tag{B-15}$$

The solution of Equation B-15, yields half of the contribution of each voxel to the edge and is obtained by,

$$\int_{R_1} dV = \int_0^d \left(\int_0^{xd} \left(\int_0^{dy} dz \right) dy \right) dx = d \int_0^d \int_0^{yd} z \, dy dx = d^2 \int_0^d \frac{y^2}{2} \Big|_0^d dx = d^3 \frac{x^3}{6} \Big|_0^d = \frac{d^3}{6} . \tag{B-16}$$

The total volume is twice of Equation B-16, yielding a result given by

$$\int_{R_1} dV = \frac{d^3}{3} \quad . \quad (B-17)$$

At any separation, M , the number of voxels and the volume each voxel contributes to the edge weight is given by

<i>separation</i>	<i>(number of $d^3/3$ voxels), number of d^3 voxels</i>	
$M_1 = 1$	$(3,3,6), 1$	
$M_2 = 2$	$(3,3,6,6), 2$	
$M_3 = 3$	$(3,3,6,6,6), 3$	
\vdots	\vdots	
$M_M = M$	$(3,3,6M), M$. (B-18)

Therefore the total volume of region R becomes,

$$\int_R dV = \frac{d^3}{3}(6M + 6) + Md^3 = (3M + 2)d^3 \quad . \quad (B-19)$$

Finally the edge for the slant on a plane with a surface area of the nodes specified by Equation B-5, a mean edge length equal to Equation B-14 and the volume occupied by the fiber obtained by Equation B-19, yields an edge weight given by

$$w(e) = \frac{1}{6d^2} \frac{1}{\sqrt{3}d \frac{(3M+2)}{3}} (3M+2)d^3 = \frac{1}{2\sqrt{3}} \approx 0.289 \quad , \quad (B-20)$$

regardless of the physical length of the edge.

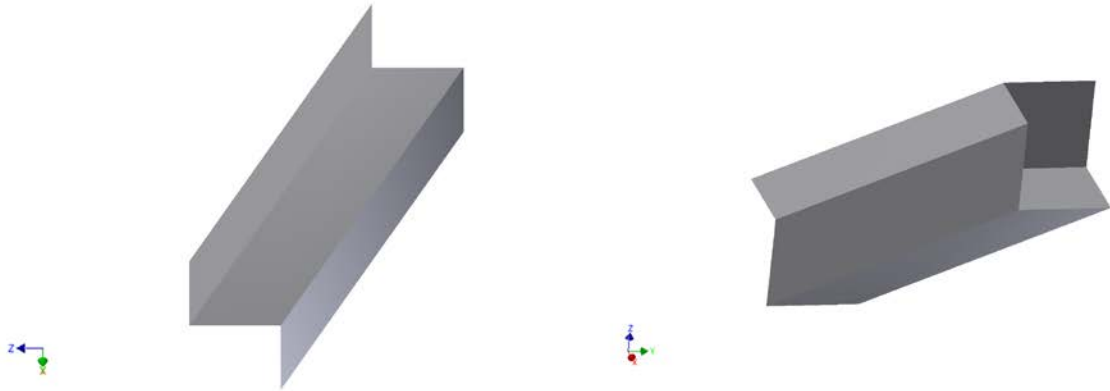


Figure B-1. 3D fiber sideways. Nodes are not shown to simplify the visualization.

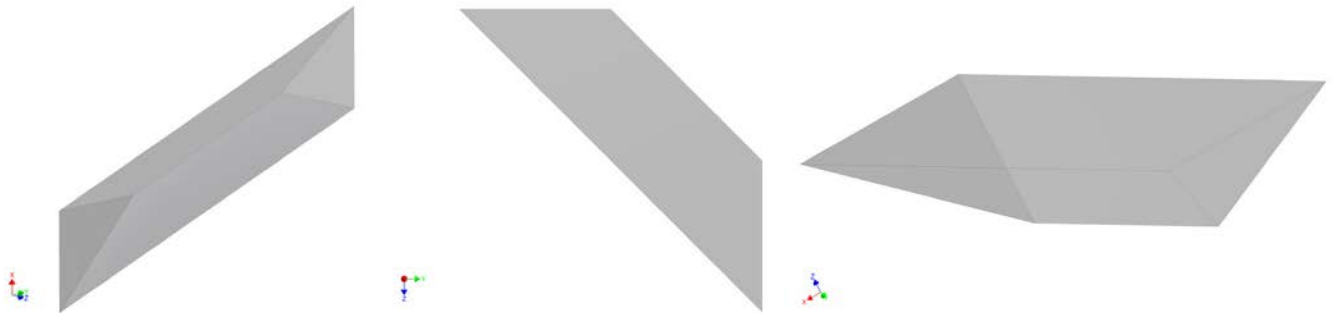


Figure B-2. Sketch of one of the portions that make up the fiber. In the left most sketch it can be seen that for every short fiber there are two of the long ones. The middle sketch shows a short side, which has a length of $\sqrt{3}$ and the longer one is $2\sqrt{3}$. In the right most sketch it can be seen the triangular cross section of the fiber, yielding a higher number of longer fibers compared to the short ones.

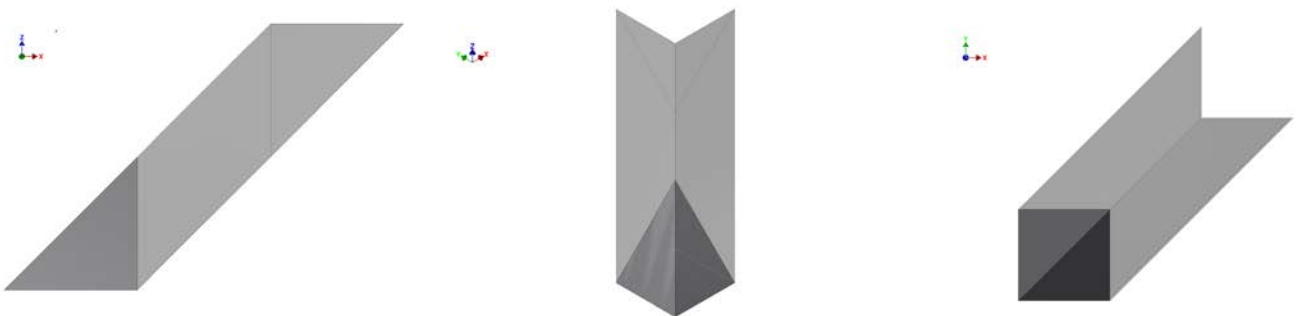


Figure B-3. Sketch of the piece of the voxel volume (dark gray) adjacent (on top) to the node that contributes to the edge. The left most sketch shows the dark gray corresponds to the voxel above the node voxel on a sideways view. The middle sketch shows the voxel above the node voxel on a view along the z axis. The rightmost sketch corresponds to the voxel above the node voxel on a top view.

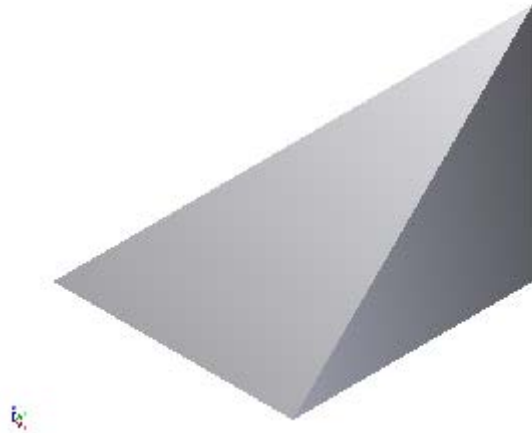


Figure B-4. Sketch of the isolated piece of the voxel contributing to the edge. This volume is repeated along the fiber length except in middle nodes where the entirety of voxel contributes to the edge weight.

APPENDIX C COMPUTER CODES

The codes in this appendix can be copy and pasted to be used in R as they appear.

Dikstras algorithm (Section 5.3.2)

```
pathLen_w <- function (g, pm){
  # g, is the binary network as a network object as defined by R
  using the network library
  # pm, is the weighted adjacency matrix.

  source_node=1
  nodes= network.size(g)
  neigh=get.neighborhood(g,source_node)
  remlist=list(source_node)
  for(i in 1:(nodes*nodes)){
    if(pm[i]==0){pm[i]=NA}}

  for(i in 1:nodes){
    ind= which.min(pm[i,])
    pm[i,i]=2*pm[i,ind]}

  while(length(pm)-length(which(!pm=="NA")) !=0){
    while(length(pm[source_node,])-length(which(!pm[source_node,
]= "NA")) !=0){
      nei_num=length(neigh)
      remlist=list(unlist(remlist),neigh)
      neighTwo=array(0,nei_num)

      for(i in 1:nei_num){
        neighTwo[i]=list(get.neighborhood(g,neigh[i]))

        neighTwo[i]=list(setdiff(unlist(neighTwo[i]),unlist(remlist)))
      }
      if(nei_num > 1){
        for(i in 1:(nei_num-1)){
          for(j in (i+1):nei_num){
            if(length(unlist(neighTwo[i]))!=0 &&
length(unlist(neighTwo[j]))!=0){
              rem_n
=intersect(unlist(neighTwo[i]),unlist(neighTwo[j]))
              rem_check=length(rem_n)
              if(rem_check !=0){
                for(k in 1:rem_check){
                  rem_vert=which(rem_n[k]==unlist(neighTwo[i]),
arr.ind= TRUE)
                  ew1=
pm[source_node,neigh[i]]+pm[neigh[i],unlist(neighTwo[i])[which(unlist(
neighTwo[i])==rem_n[k])]]
                  ew2=
```

```

pm[source_node,neigh[j]]+pm[neigh[j],unlist(neighTwo[j])[which(unlist(
neighTwo[j])==rem_n[k])]]
      if(ew1<ew2){
        neighTwo[j]=list(setdiff(unlist(neighTwo[j]),rem_n[k]))
      }else
neighTwo[i]=list(setdiff(unlist(neighTwo[i]),rem_n[k]))}
    }
  }
}
remlist=list(c(unlist(neighTwo),unlist(remlist)))
for(i in 1:length(neigh)){
  if(length(unlist(neighTwo[i]))>0){
    for(j in 1:length(unlist(neighTwo[i]))){
      pm[source_node,unlist(neighTwo[i])[j]]=pm[source_node,neigh[i]]+pm
[neigh[i],unlist(neighTwo[i])[j]]
      pm[unlist(neighTwo[i])[j],source_node]=pm[source_node,unlist(neigh
Two[i])[j]]
    }
  }
}
neigh=unlist(neighTwo[1:length(neighTwo)])
}
source_node=source_node+1
neigh=get.neighborhood(g,source_node)
remlist=list(source_node)
}
pm
}

```

Null hypothesis graphs

```

createNullHypMat_weighted_beta <- function(ew, deg){
  # ew, is the list of edge weights desired to replicate.These
  should be ordered, it does not matter if its an increasing or
  decreasing sequence.
  # deg, is the degree sequence desired to replicate
  ew=sample(ew)
  nodes = length(deg)
  Adj = array(0, c(nodes,nodes))
  Adj_w = array(0, c(nodes,nodes))

```

```

deg=as.numeric(sort(deg, decreasing=TRUE))
degNull=colSums(Adj)
ind_ew=1

while(sum(deg)/2 != sum(degNull)/2){
Adj = array(0, c(nodes,nodes))
Adj_w = array(0, c(nodes,nodes))
degNull=colSums(Adj)
ind_ew=1
for(i in 1:(nodes-1)){
  #print(i)
edges = sample(c((i+1):nodes))
x=1
while((deg[i]-degNull[i]) != 0){
  if(((deg[edges[x]]-degNull[edges[x]]) != 0)){
    Adj_w[i, edges[x]]=ew[ind_ew]
    Adj_w[edges[x], i]=ew[ind_ew]
    Adj[i, edges[x]]=1
    Adj[edges[x], i]=1
    degNull= colSums(Adj)
    x=x+1
    if(x > length(edges) && (deg[i]-degNull[i]) != 0){
      i=1
      ind_ew=1
      break
    }
    ind_ew = ind_ew + 1
  }else{
    x=x+1
    if(x > length(edges)){
      i=1
      ind_ew=1
      break
    }
  }
}
}
print('done')
Adj_w
}

```

APPENDIX D
AUTHOR'S PUBLICATIONS

PUBLISHED

- Ford, A., **Colon-Perez, L.**, Triplett, W., Gullett, J., Mareci, T., FitzGerald, D., 2013. Imaging White Matter in Human Brainstem. *Frontiers in Human Neuroscience* In Press.
- Ingo, C., Magin, R.L., **Colon-Perez, L.**, Triplett, W., Mareci, T.H., 2013. On random walks and entropy in diffusion-weighted magnetic resonance imaging studies of neural tissue. *Magn Reson Med* In Press
- Magin, R.L., Ingo, C., **Colon-Perez, L.**, Triplett, W., Mareci, T.H., 2013. Characterization of anomalous diffusion in porous biological tissues using fractional order derivatives and entropy. *Microporous and Mesoporous Materials* 178, 39-43.
- Powell, M.H., Nguyen, H.V., Gilbert, M., Parekh, M., **Colon-Perez, L.M.**, Mareci, T.H., Montie, E., 2012. Magnetic resonance imaging and volumetric analysis: Novel tools to study the effects of thyroid hormone disruption on white matter development. *Neurotoxicology* 33, 1322-1329.

CONFERENCES

- Colon-Perez, L.**, Couret, M., Triplett, W., and Mareci, T.H., 2013. Generalized framework to study brain weighted networks. *Biophysical Society 57th Annual Meeting*, Philadelphia, PA, USA.
- Colon-Perez, L.**, Horesh, R., Triplett, W., Parekh, M. and Mareci, T. H., 2011. Low Resolution network connectivity of the limbic system using Diffusion Weighted Imaging. *International Society for Magnetic Resonance in Medicine Conference*, Montreal, Quebec, Canada.
- Colon-Perez, L.**, Spindler, C., Goicochea, S., Triplett, W., and Mareci, T.H., 2011. Edge weight measurements using Diffusion Weighted Imaging; effects of resolution on brain network parameters. *Southeastern Magnetic Resonance Conference*, Atlanta, GA, USA
- Colon-Perez, L.**, Spindler, C., Goicochea, S., Triplett, W., Parekh, M., Montie, E.W., Carney, P.R., Mareci, T.H., 2012. Brain network metric derived from DWI: application to the limbic system. *Meeting of the International Society for Magnetic Resonance in Medicine International Society for Magnetic Resonance in Medicine*, Melbourne, Australia.

IN PREPARATION

- Colon-Perez, L.**, Spindler, C., Goicochea, S., Triplett, W., Parekh, M., Paul Carney, P., and Mareci, T.H. Local Brain Connectivity Measure for Weighted Networks.
- Colon-Perez, L.**, Couret, M., Triplett, W., and Mareci, T.H. Topology of weighted human cortical networks.
- Colon-Perez, L.**, Montie, E., Couret, M., and Mareci, T.H. Connectivity changes in cortical rat networks with thyroid hormone disruption.

APPENDIX E GLOSSARY INDEX

- Adjacency matrix, a square matrix describing the connectivity of a graph. The elements of the adjacency matrix represent the presence or lack of connections between nodes
- Binary networks, when edges of a graph are equivalent. The adjacency matrix is described by ones (presence of connection) and zeros (lack of connection)
- Clustering, the property of graphs to form triangles among nodes
- Degree, the degree of a node refers to the number of edges connecting it
- Edge, connection between pairs of nodes (e.g. axons connecting neurons, WM bundles connecting brain regions, friendship between individuals and so on)
- Functional networks, brain networks derived from functional data (e.g. fMRI, EEG)
- Graph, a mathematical description of a real world network. A mathematical construct composed by a set of nodes and a set of edges
- Hub, a node with a high number of edges connecting to it compared to others in the network
- Neighbors, the neighbors of a node is the set of all nodes connected it
- Node, the basic object in a network (e.g. neuron, brain regions, people, and so on)
- Null hypothesis graphs, graphs with a connectivity described by a random network (maintaining the degree distribution and number of nodes of a real network) used to test the statistical significance of measured network properties from real world networks
- Path length, the minimal number of edges that connect two nodes
- Random network, a type of network also known as Erdős and Rényi network. In these networks edges connecting nodes are assigned at random
- Scale free network, a type of network first described by Albert and Barabási. In these networks the degree distribution is characterized by a power law due to the presence of hubs.
- Small world network, a type of network first introduced by Milgram and mathematically explained by Watts and Strogatz. These networks display a high level of clustering among the neighbors of a node and short path lengths from any node to any other node
- Structural networks, brain networks derived from structural correlation among nodes (e.g. from tractography, cortical thickness and so on)
- Weighted networks, when edges of the graph are characterized by a parameter associated with the strength of connection between node pairs

LIST OF REFERENCES

- Albert, R., Barabási, A.-L., 2002. Statistical mechanics of complex networks. *Reviews of Modern Physics* 74, 47.
- Alexander, A.L., Hasan, K.M., Lazar, M., Tsuruda, J.S., Parker, D.L., 2001. Analysis of partial volume effects in diffusion-tensor MRI. *Magn Reson Med* 45, 770-780.
- Assaf, Y., Basser, P.J., 2005. Composite hindered and restricted model of diffusion (CHARMED) MR imaging of the human brain. *Neuroimage* 27, 48-58.
- Assaf, Y., Blumenfeld-Katzir, T., Yovel, Y., Basser, P.J., 2008. AxCaliber: a method for measuring axon diameter distribution from diffusion MRI. *Magn Reson Med* 59, 1347-1354.
- Assaf, Y., Freidlin, R.Z., Rohde, G.K., Basser, P.J., 2004. New modeling and experimental framework to characterize hindered and restricted water diffusion in brain white matter. *Magn Reson Med* 52, 965-978.
- Barabási, A.-L., 2003. *Linked: How Everything Is Connected to Everything Else and What It Means for Business, Science, and Everyday Life*. Plume, USA.
- Barabási, A.-L., 2009. Scale-free networks: a decade and beyond. *Science* 325, 412-413.
- Barabási, A.-L., 2011. The network takeover. *Nature Physics* 8, 14-16.
- Barabási, A.-L., Albert, R., 1999. Emergence of scaling in random networks. *Science* 286, 509-512.
- Barrat, A., Barthélemy, M., Pastor-Satorras, R., Vespignani, A., 2004. The architecture of complex weighted networks. *Proceedings of the National Academy of Sciences of the United States of America* 101, 3747-3752.
- Basser, P.J., 2002. Relationships between diffusion tensor and q-space MRI. *Magn Reson Med* 47, 392-397.
- Basser, P.J., Jones, D.K., 2002. Diffusion-tensor MRI: theory, experimental design and data analysis - a technical review. *NMR Biomed* 15, 456-467.
- Basser, P.J., Mattiello, J., LeBihan, D., 1994. MR diffusion tensor spectroscopy and imaging. *Biophys.J.* 66, 259-267.
- Bassett, D.S., Brown, J.A., Deshpande, V., Carlson, J.M., Grafton, S.T., 2011a. Conserved and variable architecture of human white matter connectivity. *Neuroimage* 54, 1262-1279.

- Bassett, D.S., Brown, J.A., Deshpande, V., Carlson, J.M., Grafton, S.T., 2011b. Conserved and variable architecture of human white matter connectivity. *Neuroimage* 54, 1262-1279.
- Bassett, D.S., Bullmore, E., 2006. Small-world brain networks. *Neuroscientist*. 12, 512-523.
- Bastin, M.E., Armitage, P.A., Marshall, I., 1998. A theoretical study of the effect of experimental noise on the measurement of anisotropy in diffusion imaging. *Magnetic Resonance Imaging* 16, 773-785.
- Bernstein, M.A., King, K.E., Zhou, X.J., 2004. *Handbook of MRI Pulse Sequences*. Academic Press.
- Bertram, E.H., 2009. Temporal lobe epilepsy: where do the seizures really begin? *Epilepsy Behav* 14 Suppl 1, 32-37.
- Boccaletti, S., Latora, V., Moreno, Y., Chavez, M., Hwang, D.U., 2006. Complex networks: Structure and dynamics. *Physics Reports* 424, 175-308.
- Brazdil, M., Mikl, M., Marecek, R., Krupa, P., Rektor, I., 2007. Effective connectivity in target stimulus processing: a dynamic causal modeling study of visual oddball task. *Neuroimage* 35, 827-835.
- Brown, R., 1828. A brief account microscopical observations made in the months of June, July, and August 1827, on the particles contained in pollen plants; and on the general existence of active molecules in organic and inorganic bodies. *Philosophical Magazine* 4, 161-173.
- Bullmore, E., Sporns, O., 2009. Complex brain networks: graph theoretical analysis of structural and functional systems. *Nat Rev Neurosci* 10, 186-198.
- Butts, C.T., 2009. Revisiting the foundations of network analysis. *Science* 325, 414-416.
- Callaghan, P., 1991. *Principles of Nuclear Magnetic Resonance Microscopy*. Oxford University Press, Oxford, England.
- Cammoun, L., Gigandet, X., Meskaldji, D., Thiran, J.P., Sporns, O., Do, K.Q., Maeder, P., Meuli, R., Hagmann, P., 2011. Mapping the human connectome at multiple scales with diffusion spectrum MRI. *J Neurosci Methods* 203, 386-397.
- Carr, H.Y., Purcell, E.M., 1954. Effects of Diffusion on Free Precession in Nuclear Magnetic Resonance Experiments. *Physical Review* 94, 630-638.
- Catani, M., Ffytche, D.H., 2005. The rises and falls of disconnection syndromes. *Brain* 128, 2224-2239.

- Catani, M., Howard, R.J., Pajevic, S., Jones, D.K., 2002. Virtual in vivo interactive dissection of white matter fasciculi in the human brain. *Neuroimage* 17, 77-94.
- Chavez, M., Hwang, D.U., Amann, A., Hentschel, H.G., Boccaletti, S., 2005. Synchronization is enhanced in weighted complex networks. *Phys Rev Lett* 94, 218701.
- Cheng, H., Wang, Y., Sheng, J., Kronenberger, W.G., Mathews, V.P., Hummer, T.A., Saykin, A.J., 2012a. Characteristics and variability of structural networks derived from diffusion tensor imaging. *Neuroimage*.
- Cheng, H., Wang, Y., Sheng, J., Sporns, O., Kronenberger, W.G., Mathews, V.P., Hummer, T.A., Saykin, A.J., 2012b. Optimization of seed density in DTI tractography for structural networks. *J Neurosci Methods* 203, 264-272.
- Colon-Perez, L., Spindler, C., Goicochea, S., Triplett, W., Parekh, M., Montie, E.W., Carney, P.R., Mareci, T.H., 2012. Brain network metric derived from DWI: application to the limbic system. Meeting of the International Society for Magnetic Resonance in Medicine International Society for Magnetic Resonance in Medicine, Melbourne, Australia, p. 686.
- Concha, L., Gross, D.W., Beaulieu, C., 2005. Diffusion tensor tractography of the limbic system. *AJNR Am J Neuroradiol* 26, 2267-2274.
- Conturo, T.E., Lori, N.F., Cull, T.S., Akbudak, E., Snyder, A.Z., Shimony, J.S., McKinstry, R.C., Burton, H., Raichle, M.E., 1999. Tracking neuronal fiber pathways in the living human brain. *Proc Natl Acad Sci U S A* 96, 10422-10427.
- Cormen, T.H., Leiserson, C.E., Rivest, R.L., Stein, C., 2009. Introduction to algorithms 3rd ed. MIT Press, Cambridge, Mass.
- Costa Lda, F., Kaiser, M., Hilgetag, C.C., 2007. Predicting the connectivity of primate cortical networks from topological and spatial node properties. *BMC Syst Biol.* 1, 16.
- Craddock, R.C., Jbabdi, S., Yan, C.G., Vogelstein, J.T., Castellanos, F.X., Di Martino, A., Kelly, C., Heberlein, K., Colcombe, S., Milham, M.P., 2013. Imaging human connectomes at the macroscale. *Nat Methods* 10, 524-539.
- Crank, J., 1980. *The Mathematics of Diffusion*, 2nd ed. Oxford University Press Inc., New York, USA.
- Crick, F., Jones, E., 1993. Backwardness of human neuroanatomy. *Nature* 361, 109-110.
- Eguiluz, V.M., Chialvo, D.R., Cecchi, G.A., Baliki, M., Apkarian, A.V., 2005. Scale-free brain functional networks. *Phys Rev Lett* 94, 018102.

- Einstein, A., 1905. Investigations on the Theory of Brownian Movement. *Annalen der Physik* 17, 549-560.
- Erdős, P., Rényi, A., 1959. On random graphs, I. *Publicationes Mathematicae (Debrecen)* 6, 290-297.
- Erdős, P., Rényi, A., 1960. On the evolution of random graphs. *Publication of the Mathematical Institute of the Hungarian Academy of Sciences* 5, 17-60.
- Fischl, B., 2012. FreeSurfer. *Neuroimage* 62, 774-781.
- Fischl, B., van der Kouwe, A., Destrieux, C., Halgren, E., Segonne, F., Salat, D.H., Busa, E., Seidman, L.J., Goldstein, J., Kennedy, D., Caviness, V., Makris, N., Rosen, B., Dale, A.M., 2004. Automatically parcellating the human cerebral cortex. *Cereb Cortex* 14, 11-22.
- Friston, K.J., Harrison, L., Penny, W., 2003. Dynamic causal modelling. *Neuroimage* 19, 1273-1302.
- Glickstein, M., 2006. Golgi and Cajal: The neuron doctrine and the 100th anniversary of the 1906 Nobel Prize. *Current Biology* 16, R147-151.
- Gong, G., He, Y., Concha, L., Lebel, C., Gross, D.W., Evans, A.C., Beaulieu, C., 2009. Mapping anatomical connectivity patterns of human cerebral cortex using in vivo diffusion tensor imaging tractography. *Cereb Cortex* 19, 524-536.
- Granovetter, M.S., 1973. The Strength of Weak Ties. *American Journal of Sociology* 78, 1360-1380.
- Guye, M., Bettus, G., Bartolomei, F., Cozzone, P.J., 2010. Graph theoretical analysis of structural and functional connectivity MRI in normal and pathological brain networks. *MAGMA* 23, 409-421.
- Haacke, E.M., Brown, R.W., Thompson, M.R., Venkatesan, R., 1999. *Magnetic Resonance Imaging Physical Principles and Sequence Design*. John Wiley & Sons, New York.
- Hagmann, P., Cammoun, L., Gigandet, X., Gerhard, S., Ellen Grant, P., Wedeen, V., Meuli, R., Thiran, J.-P., Honey, C.J., Sporns, O., 2010a. MR connectomics: Principles and challenges. *Journal of Neuroscience Methods* 194, 34-45.
- Hagmann, P., Cammoun, L., Gigandet, X., Meuli, R., Honey, C.J., Wedeen, V.J., Sporns, O., 2008. Mapping the structural core of human cerebral cortex. *PLoS Biol* 6, e159.
- Hagmann, P., Kurant, M., Gigandet, X., Thiran, P., Wedeen, V.J., Meuli, R., Thiran, J.P., 2007. Mapping human whole-brain structural networks with diffusion MRI. *PLoS ONE* 2, e597.

- Hagmann, P., Sporns, O., Madan, N., Cammoun, L., Pienaar, R., Wedeen, V.J., Meuli, R., Thiran, J.P., Grant, P.E., 2010b. White matter maturation reshapes structural connectivity in the late developing human brain. *Proc Natl Acad Sci U S A* 107, 19067-19072.
- He, Y., Dagher, A., Chen, Z., Charil, A., Zijdenbos, A., Worsley, K., Evans, A., 2009. Impaired small-world efficiency in structural cortical networks in multiple sclerosis associated with white matter lesion load. *Brain*. 132, 3366-3379. Epub .
- Hodgkin, A.L., Huxley, A.F., 1952. A quantitative description of membrane current and its application to conduction and excitation in nerve. *J Physiol* 117, 500-544.
- Honey, C.J., Thivierge, J.-P., Sporns, O., 2010. Can structure predict function in the human brain? *Neuroimage* 52, 766-776.
- Humphries, M.D., Gurney, K., 2008. Network 'small-world-ness': a quantitative method for determining canonical network equivalence. *PLoS ONE* 3, e0002051.
- Iturria-Medina, Y., Canales-Rodriguez, E.J., Melie-Garcia, L., Valdes-Hernandez, P.A., Martinez-Montes, E., Aleman-Gomez, Y., Sanchez-Bornot, J.M., 2007. Characterizing brain anatomical connections using diffusion weighted MRI and graph theory. *Neuroimage* 36, 645-660.
- Jellison, B.J., Field, A.S., Medow, J., Lazar, M., Salamat, M.S., Alexander, A.L., 2004. Diffusion tensor imaging of cerebral white matter: a pictorial review of physics, fiber tract anatomy, and tumor imaging patterns. *AJNR Am J Neuroradiol* 25, 356-369.
- Jenkinson, M., Bannister, P., Brady, M., Smith, S., 2002. Improved optimization for the robust and accurate linear registration and motion correction of brain images. *Neuroimage* 17, 825-841.
- Jenkinson, M., Beckmann, C.F., Behrens, T.E., Woolrich, M.W., Smith, S.M., 2012. Fsl. *Neuroimage* 62, 782-790.
- Jian, B., Vemuri, B.C., Ozarslan, E., Carney, P., Mareci, T., 2007a. A Continuous Mixture of Tensors Model for Diffusion-Weighted Mr Signal Reconstruction. *Proc IEEE Int Symp Biomed Imaging* 4, 772-775.
- Jian, B., Vemuri, B.C., Ozarslan, E., Carney, P.R., Mareci, T.H., 2007b. A novel tensor distribution model for the diffusion-weighted MR signal. *Neuroimage* 37, 164-176.
- Jones, D.K., Horsfield, M.A., Simmons, A., 1999. Optimal strategies for measuring diffusion in anisotropic systems by magnetic resonance imaging. *Magn Reson Med* 42, 515-525.
- Jones, D.K., Leemans, A., 2011. Diffusion Tensor Imaging. *Methods in Molecular Biology*. Springer, pp. 127-144.

- Langer, N., Pedroni, A., Jancke, L., 2013. The problem of thresholding in small-world network analysis. *PLoS ONE* 8, e53199.
- Lee, J.H., Durand, R., Gradinaru, V., Zhang, F., Goshen, I., Kim, D.S., Fenno, L.E., Ramakrishnan, C., Deisseroth, K., 2010. Global and local fMRI signals driven by neurons defined optogenetically by type and wiring. *Nature* 465, 788-792.
- Lo, C.Y., He, Y., Lin, C.P., 2011. Graph theoretical analysis of human brain structural networks. *Rev Neurosci* 22, 551-563.
- Lo, C.Y., Wang, P.N., Chou, K.H., Wang, J., He, Y., Lin, C.P., 2010. Diffusion tensor tractography reveals abnormal topological organization in structural cortical networks in Alzheimer's disease. *J Neurosci* 30, 16876-16885.
- Lu, H., Zou, Q., Gu, H., Raichle, M.E., Stein, E.A., Yang, Y., 2012. Rat brains also have a default mode network. *Proc Natl Acad Sci U S A* 109, 3979-3984.
- Magistretti, P.J., Pellerin, L., 1999. Cellular mechanisms of brain energy metabolism and their relevance to functional brain imaging. *Philos Trans R Soc Lond B Biol Sci* 354, 1155-1163.
- Magistretti, P.J., Pellerin, L., Rothman, D.L., Shulman, R.G., 1999. Energy on demand. *Science* 283, 496-497.
- Miles, J., Laidlaw, D.H., 2012. Predicting DTI Tractography Uncertainty from Diffusion-Weighted-Image Noise. ISMRM 20th Annual Meeting & Exhibition, Melbourne, Australia, p. 1906.
- Milgram, S., 1967. The small world problem. *Psychology Today* 1, 61-67.
- Mori, S., Crain, B.J., Chacko, V.P., van Zijl, P.C., 1999. Three-dimensional tracking of axonal projections in the brain by magnetic resonance imaging. *Ann Neurol* 45, 265-269.
- Nadler, J.V., 2003. The recurrent mossy fiber pathway of the epileptic brain. *Neurochem Res* 28, 1649-1658.
- Newman, M., 2010. *Networks: An Introduction*. Oxford University Press, New York, USA, USA.
- Newman, M.E.J., 2001. Scientific collaboration networks. II. Shortest paths, weighted networks, and centrality. *Physical Review E* 64.
- Ogawa, S., Lee, T.M., Kay, A.R., Tank, D.W., 1990. Brain magnetic resonance imaging with contrast dependent on blood oxygenation. *Proceedings of the Royal Society of London A* 87, 9868-9872.

- Onnela, J.P., Saramaki, J., Kertesz, J., Kaski, K., 2005. Intensity and coherence of motifs in weighted complex networks. *Physical review. E, Statistical, nonlinear, and soft matter physics* 71, 065103.
- Ozarslan, E., Shepherd, T.M., Vemuri, B.C., Blackband, S.J., Mareci, T.H., 2006. Resolution of complex tissue microarchitecture using the diffusion orientation transform (DOT). *Neuroimage* 31, 1086-1103.
- Paxinos, G., Watson, C., 1998. *The Rat Brain in Stereotaxic Coordinates*, 4th ed. Academic Press, San Diego.
- Penny, W.D., Stephan, K.E., Mechelli, A., Friston, K.J., 2004. Modelling functional integration: a comparison of structural equation and dynamic causal models. *Neuroimage* 23 Suppl 1, S264-274.
- Phillips, R., Kondev, J., Theriot, J., 2008. *Physical Biology of the Cell*, 1st ed. Garland Science.
- Ponten, S.C., Douw, L., Bartolomei, F., Reijneveld, J.C., Stam, C.J., 2009. Indications for network regularization during absence seizures: weighted and unweighted graph theoretical analyses. *Exp Neurol.* 217, 197-204. Epub 2009 Feb 2013.
- Poustchi-Amin, M., Mirowitz, S.A., Brown, J.J., McKinstry, R.C., Li, T., 2001. Principles and applications of echo-planar imaging: a review for the general radiologist. *Radiographics* 21, 767-779.
- Powell, M.H., Nguyen, H.V., Gilbert, M., Parekh, M., Colon-Perez, L.M., Mareci, T.H., Montie, E., 2012. Magnetic resonance imaging and volumetric analysis: Novel tools to study the effects of thyroid hormone disruption on white matter development. *Neurotoxicology* 33, 1322-1329.
- Raichle, M.E., MacLeod, A.M., Snyder, A.Z., Powers, W.J., Gusnard, D.A., Shulman, G.L., 2001. A default mode of brain function. *Proc Natl Acad Sci U S A* 98, 676-682.
- Rilling, J.K., Barks, S.K., Parr, L.A., Preuss, T.M., Faber, T.L., Pagnoni, G., Bremner, J.D., Votaw, J.R., 2007. A comparison of resting-state brain activity in humans and chimpanzees. *Proc Natl Acad Sci U S A* 104, 17146-17151.
- Romero-Garcia, R., Atienza, M., Clemmensen, L.H., Cantero, J.L., 2012. Effects of network resolution on topological properties of human neocortex. *Neuroimage* 59, 3522-3532.
- Rosen, K., 2003. *Discrete Mathematics & its Applications*, 5th ed. Mc-Graw Hill.
- Rubinov, M., Sporns, O., 2010. Complex network measures of brain connectivity: uses and interpretations. *Neuroimage* 52, 1059-1069.

- Saramaki, J., Kivel, M., Onnela, J.-P., Kaski, K., Kertesz, J., 2007. Generalizations of the clustering coefficient to weighted complex networks. *Physical Review E* 75, 027105.
- Seghier, M.L., Friston, K.J., 2013. Network discovery with large DCMs. *Neuroimage* 68, 181-191.
- Sotelo, C., 2011. Camillo Golgi and Santiago Ramon y Cajal: the anatomical organization of the cortex of the cerebellum. Can the neuron doctrine still support our actual knowledge on the cerebellar structural arrangement? *Brain Res Rev* 66, 16-34.
- Sporns, O., 2011. *Networks of the brain*. MIT Press, Cambridge, Mass.
- Sporns, O., Honey, C.J., Kotter, R., 2007. Identification and classification of hubs in brain networks. *PLoS One*. 2, e1049.
- Sporns, O., Tononi, G., Kotter, R., 2005. The human connectome: A structural description of the human brain. *PLoS Comput Biol* 1, e42.
- Stefan, H., Lopes da Silva, F.H., 2013. Epileptic neuronal networks: methods of identification and clinical relevance. *Front Neurol* 4, 8.
- Stejskal, E.O., Tanner, J.E., 1965. Spin Diffusion Measurements: Spin Echoes in the Presence of a Time-Dependent Field Gradient. *Journal of Chemical Physics* 42, 288-292.
- Stephan, K.E., Tittgemeyer, M., Knosche, T.R., Moran, R.J., Friston, K.J., 2009. Tractography-based priors for dynamic causal models. *Neuroimage* 47, 1628-1638.
- Teramae, J.N., Tsubo, Y., Fukai, T., 2012. Optimal spike-based communication in excitable networks with strong-sparse and weak-dense links. *Sci Rep* 2, 485.
- Tomasi, D., Volkow, N.D., 2011. Functional connectivity hubs in the human brain. *Neuroimage* 57, 908-917.
- Torrey, H.C., 1953. Nuclear Spin Relaxation by Translational Diffusion. *Physical Review* 92, 8.
- Torrey, H.C., 1956. Bloch Equations with Diffusion Terms. *Physical Review* 104, 563-565.
- Tournier, J.D., Calamante, F., Gadian, D.G., Connelly, A., 2004. Direct estimation of the fiber orientation density function from diffusion-weighted MRI data using spherical deconvolution. *Neuroimage* 23, 1176-1185.
- Tuch, D.S., 2004. Q-ball imaging. *Magn Reson Med* 52, 1358-1372.

- Tuch, D.S., Reese, T.G., Wiegell, M.R., Makris, N., Belliveau, J.W., Wedeen, V.J., 2002. High angular resolution diffusion imaging reveals intravoxel white matter fiber heterogeneity. *Magn Reson Med* 48, 577-582.
- Tuch, D.S., Weisskoff, R.M., Belliveau, J.W., Wedeen, V.J., 1999. High angular resolution diffusion imaging of the human brain. 7th annual meeting of the Society for Magnetic Resonance in Medicine, Philadelphia.
- van den Heuvel, M.P., Mandl, R.C., Stam, C.J., Kahn, R.S., Hulshoff Pol, H.E., 2010. Aberrant frontal and temporal complex network structure in schizophrenia: a graph theoretical analysis. *J Neurosci* 30, 15915-15926.
- van den Heuvel, M.P., Sporns, O., 2011. Rich-club organization of the human connectome. *J Neurosci* 31, 15775-15786.
- van den Heuvel, M.P., Stam, C.J., Boersma, M., Hulshoff Pol, H.E., 2008. Small-world and scale-free organization of voxel-based resting-state functional connectivity in the human brain. *Neuroimage* 43, 528-539.
- van der Marel, K., Homberg, J.R., Otte, W.M., Dijkhuizen, R.M., 2013. Functional and structural neural network characterization of serotonin transporter knockout rats. *PLoS ONE* 8, e57780.
- Vincent, J.L., Patel, G.H., Fox, M.D., Snyder, A.Z., Baker, J.T., Van Essen, D.C., Zempel, J.M., Snyder, L.H., Corbetta, M., Raichle, M.E., 2007. Intrinsic functional architecture in the anaesthetized monkey brain. *Nature* 447, 83-86.
- Watts, D.J., 2003. *Small Worlds: The Dynamics of Networks between Order and Randomness*, 1st ed. Princeton University Press.
- Watts, D.J., Strogatz, S.H., 1998. Collective dynamics of 'small-world' networks. *Nature* 393, 440-442.
- Wedeen, V.J., Hagmann, P., Tseng, W.Y.I., Reese, T.G., Weisskoff, R.M., 2005. Mapping complex tissue architecture with diffusion spectrum magnetic resonance imaging. *Magnetic Resonance in Medicine* 54, 1377-1386.
- Wilson, H.R., Cowan, J.D., 1972. Excitatory and inhibitory interactions in localized populations of model neurons. *Biophys J* 12, 1-24.
- Yushkevich, P.A., Piven, J., Hazlett, H.C., Smith, R.G., Ho, S., Gee, J.C., Gerig, G., 2006. User-guided 3D active contour segmentation of anatomical structures: significantly improved efficiency and reliability. *Neuroimage*. 31, 1116-1128. Epub 2006 Mar 1120.
- Zhang, B., Horvath, S., 2005. A general framework for weighted gene co-expression network analysis. *Stat Appl Genet Mol Biol* 4, Article17.

Zucker, R.S., Regehr, W.G., 2002. Short-term synaptic plasticity. *Annu Rev Physiol* 64, 355-405.

BIOGRAPHICAL SKETCH

Luis M. Colon-Perez was born in Arecibo, Puerto Rico (PR). Luis was raised in Utuado, PR, where he completed his primary and secondary school studies. After graduating from high school with the highest honors, he moved to San Juan, PR to pursue a bachelor's degree in physics from the University of Puerto Rico. During his undergraduate studies, Luis pursued many research opportunities at the University of Puerto Rico (Dr. P. Feng 2005-'06 and Dr. J. Ponce de Leon 2006-'07), also through Research Experience for Undergraduates program within the US, (Cornel, 2005 and UF, 2006) as well as internationally (Hannover Germany, Albert Einstein Institute, 2007). After completing his undergraduate studies at the University of Puerto Rico and graduating with Magna Cum Laude honors, he enrolled at the University of Florida to pursue his doctoral degree in physics. At UF, he studied brain networks using MRI under the mentorship of Dr. Thomas Mareci. The focus of these studies has been to develop novel methods to study the topological organization of brain networks.